Electromagnetic Energy Transport Through Complex Media

by

Kaelan B. Hansson

A dissertation submitted in partial fulfillment
of the requirements for the degree of
Doctor of Philosophy
(Aerospace Engineering)
in the University of Michigan
2021

Doctoral Committee:

Professor Venkat Raman, Chair
Adjunct Professor Iain D. Boyd
Professor Emeritus Edward Larsen
Professor Leung Tsang

Kaelan B. Hansson
khansson@umich.edu
ORCID iD: 0000-0002-8830-1304

For whoever, by these pages, a burden is found lifted

TABLE OF CONTENTS

DEDICATION . . . . **ii**

LIST OF FIGURES . . . . **vi**

LIST OF TABLES . . . . **xi**

ABSTRACT . . . . **xii**

CHAPTER

1 Introduction **1**

- 1.1 Multiphase Flows 4
- 1.2 Reacting Flows 6
- 1.3 Dissertation Outline 8

2 Electromagnetic Waves and Particulates **9**

- 2.1 Background 9
- 2.2 Time Harmonic Maxwell Equations 10
- 2.3 Material Properties 13
  - 2.3.1 Dielectrics 14
  - 2.3.2 Conductors 16
- 2.4 Spherical Harmonic Conventions: Past and Present 18
  - 2.4.1 Classical Spherical Harmonic Expansion 18
  - 2.4.2 Modern Spherical Harmonic Expansion 20
- 2.5 Scattering of a Sphere 22
  - 2.5.1 Dielectric Sphere 22
  - 2.5.2 Scattering from a Multilayered Sphere 27
  - 2.5.3 Scattering from a Conducting Particle 30
    - 2.5.3.1 Comparison with Dielectric Theory 32
- 2.6 Scattering of a Non-Spherical Particle 38
  - 2.6.1 The T Matrix 38
  - 2.6.2 Extended Boundary Technique 40
  - 2.6.3 Surface Impedance Formulation 40
    - 2.6.3.1 Derivation of Method 42
    - 2.6.3.2 Azimuthally Symmetric Particles 48
  - 2.6.4 Results for Spheroidal Particles 48
- 2.7 Conclusions 53

3 Radiative Transfer Through Particle Clouds **55**

3.1 Towards a Continuum Approximation 55
3.2 Homogenization Error 58
3.3 Introduction 58
3.4 The Beer-Lambert Law 60
3.4.1 Derivation 60
3.4.2 Non-Infinitesimal Particles 61
3.4.3 Mesh Refinement 62
3.5 Single Cell Simulations 66
3.6 Proposed Model 69
3.6.1 Derivation 69
3.6.2 Algorithm 70
3.6.3 Results 71
3.7 Conclusions 75

4 Analysis of a Particle Laden Flow 76

4.1 Brief Overview of Multiphase Flows 76
4.2 Analyzed System 77
4.3 Numerical Methods 80
4.3.1 Coupled system Model 80
4.3.2 High Fidelity Radiative Heat Transfer Model 81
4.3.2.1 Ray Emission Model 83
4.3.2.2 Ray Tracing Model 86
4.3.2.3 Ray Sensing Model 90
4.4 Results 91
4.4.1 Emitter Modeling 91
4.4.2 Small Beam Simulations 92
4.4.3 Mesh Refinement with Homogenization 95
4.4.4 Particle Resolved vs. Homogenization 99
4.5 Discussion 101
4.5.1 Mie Properties 101
4.5.2 Oxide Coating 102
4.5.3 Spheroid Particle 104
4.5.4 Magnetic Particles 107
4.5.5 Particle Sticking 108
4.6 Conclusions 116

5 Radiative Transfer Through Reacting Gas Flows 118

5.1 Introduction 118
5.2 Review of Experiments 123
5.2.1 Axisymetric flow from University of Queensland 123
5.2.2 One Dimension Shocks from EAST 125
5.3 Numerical Methods 126
5.3.1 CFD 126
5.3.2 CFD Chemistry 129
5.3.3 One Dimensional Shock Flows 131

5.3.3.1 Shock Control Derivation 133
5.3.3.2 Application 137
5.3.4 Radiative Heat Transfer 139
5.3.4.1 Hydrogen Atom 140
5.3.4.2 Molecular Hydrogen 141
5.4 Results 145
5.4.1 Queensland Data 145
5.4.2 EAST Data 149
5.5 Summary and Conclusions 175

6 Conclusion 177

6.1 Summary 177
6.2 Novel Research Contributions 179
6.3 Recommendations for Future Work 180

BIBLIOGRAPHY 183

LIST OF FIGURES

FIGURE

2.1 Extinction efficiencies of particles of size parameter 15 with various indices of refraction. The surface impedance and dielectric models are used. The relative errors can be found in Figure 2.2a. 35
2.2 Relative errors between the dielectric and surface impedance models for a class of particles of size parameter 15. 36
2.3 Relative error between Mie and surface impedance scattering calculations for optical efficiencies. The index of refraction used is $3 + 2.5i$. The ratio of skin depth to the radius of the particle is also included 37
2.4 Schematic of the dielectric extended boundary method. The particle is modeled as a surface of currents (both magnetic and electric) which, in vacuum, generate the scattered field and negate the incident field inside the surface. Those same currents generate the internal field in the particle (the fields are different due to the different electrical properties of the particle). 41
2.5 Schematic of the surface impedance extended boundary method. The particle is modeled as a surface of currents (both magnetic and electric) which, in vacuum, generate the scattered field. The internal field is modeled though the surface imedance boundary condition. 43
2.6 Schematic of physical interpretation of the optical efficiency contours as plotted in later figures. The incident beam is always considered to be moving along the X axis. The angle from the X axis is the orientation of the particle and the distance from the origin is the axis ratio. 50
2.7 Optical efficiencies of spheroidal particles with varying elongations, all with effective size parameter 30 and index of refraction $3 + 2.5i$. 51
2.8 Extended boundary method convergence with increasing maximum harmonic. All curves pertain to a spheroid of index of refraction $3 - 2.5i$ with elongation ratio of 2.0. This represents a particle on the outer extremity of Figure 2.7. Q represents an approximate scattering effiecy (Equation 2.78). The dieletric method fails to converge, even at increased computational precision. 52
3.1 Predicted error in transmission of a finite set of particles as calculated by Equation 3.10. 63
3.2 Diagram of the refinement simulations discussed in Section 3.4.3. A linear cartesian mesh is imposed on a cube filled with spherical particles of uniform diameter. Ideally, the transmission through the cube should be independent of the mesh. However, Figure 3.3 shows this is not the case with standard homogenization. . 65

3.3 A graph of the transmission through a cube filled with particles with meshes of different refinement (see Figure 3.2). Each cell is homogenized according to the Beer-Lambert Law. As the cell size decreases the transmission rises. This unphysical behavior is a result of the finite number of particles present in each cell, as opposed to the infinite number of particles assumed in the Beer-Lambert Law. 65
3.4 The same set of particle resolved simulations as shown in Figure 3.5, however, the particles are not allowed to overlap. This represents the physical configurations of solid particles. As the particles become larger, the Beer-Lambert Law overpredicts transmission. 68
3.5 Results of serval particle resolved Monte Carlo simulations of particles in a single cell. The particle diameters are varied and the optical depth is changed by adjusting the number of particles. The particles are dispersed randomly and are allowed to overlap. One can see the Beer-Lambert Law can effectively predict the transmission for all these simulations. 68
3.6 Schematic of parameters used to create the proposed radiative transfer model for solid particles. The finite number of slabs are calculated based on the particle diameter. The particles are then sorted into these slabs. 73
3.7 Comparison of the results of Figure 3.4 with results of the new model. The model captures the effect of decreasing transmission with particle size. The new model becomes inaccurate at the largest tested diameters (0.2 cell lengths) because it uses a low order description of the number of slabs (See Equation 3.11). 74
3.8 Comparison of the results of Figure 3.3 against the same simulation performed with the proposed model. The proposed model exhibits mesh independence. There is still the possibility of divergence with greater mesh refinement when the cell size and the particle diameter are comparable. 74
4.1 Schematic of radiatively heated. A single laser diode array is shown at left illuminating the glass test section contain the turbulent air-nickel mixture. . . 79
4.2 Simple rendering of the full system with one active laser diode array. The particle shown are results of the coupled simulations (Section 4.3.1). The volume is 4 cm by 4 cm by 16 cm. The blue glass is 2mm thick and is modeled as a pure absorber. The red cones denoting the incident radiation are only approximations for clarity (See Section4.3.2.1 for details). 80
4.3 Schematic of the laser diode array. Light is emitted from square chips, 24 of which are arranged in a long array. 84
4.4 Schematic diagram of particle scattering in a cell, 4.4a, and on the scattering plane, 4.4b 90
4.5 Incident flux, as seen by the experimental calorimeter, from various emission sources. The flux is normalized by the total emitted power, and therefore, has units of m^{-2} 93
4.6 Incident flux, as seen by the experimental calorimeter, by various emission sources, with particles in the channel. The flux is normalized by the total emitted power, and therefore, has units of m^{-2} 94
4.7 Scattering functions of the largest and smallest particles under consideration. . 95

4.8 Rendering of the small beam simulations with illuminated particles and both sensing patches visible. 96
4.9 Incident fluxes as seen by the sensing area. Two sensors are shown, one with a 16.5 cm offset from the outer channel wall and the other that is against the channel (no offset). The incident fluxes are normalized by the total energy emitted by the source (units m^{-2}). 96
4.10 Average transmissions predicted by PrMCRT using a sensor which is offset 16.5cm from the channel. The same simulations are performed without this sensor offset. The addition of the offset dramatically changed the perceived transmission of the flow. All error bars represent the standard variation of the transmission over all simulations (or over time in experimental measurements). Note, however, that the high fidelity sensor modeling still overpredicts transmission. 97
4.11 Absorption along the channel line for both Mass Loading cases. Each line represents a quartile boundary (e.g. the bottom line represents the minimum absorption and the middle line represents the median absorption). 97
4.12 Transmission of a single MLR 40% snapshot using homogenization over the cells. Different linear cartesian meshes are used with increasing resolution. 98
4.13 Simple rendering of the full system with one active laser diode array. A spatial averages fluxes along the colorimeter sensor is shown in blue and the total absorbed energy is shown in red. The cones denoting the incident radiation are only approximations for clarity. 100
4.14 Optical properties of nickel particles of various diameters in 973 nm light. The index of refraction is 2.4704 + 5.5117i. 100
4.15 Transmission of a single MLR 40% snapshot using homogenization over the cells. Different linear cartesian meshes are used with increasing resolution. 101
4.16 Scattering properties of a nickel particle of diameter 12 microns in 973 nm light with various indices of refraction. Note, the expected index of refraction is 2.4704 + 5.5117i. At this value, the optical properties are relatively insensitive to the index of refraction. 103
4.17 Scattering properties of nickel particles of various total diameters and oxide shell depths. The index of refraction of the pure nickel is 2.4704 + 5.5117i and the pure oxide is 2 + 0.015i. 105
4.18 Scattering properties of a nickel sphere of diameter 12 microns in 973 nm light with various indices of refraction and a 60 μm nickel oxide shell. Note, the expected index of refraction of the pure nickel is 2.4704 + 5.5117i and the pure oxide is 2 + 0.01i. The optical properties are relatively insensitive to the index of refraction. 106
4.19 Optical efficiencies of spheroidal particles with an index of refraction 2.4704 + 5.5117i and varying elongations but an effective diameter 12 microns. 112
4.20 Change in optical properties of a 11.226 micron diameter sphere exposed to light of wavelength 973 nm (index of refraction $2.4704 + 5.5117i$) with respect to magnetic permeability. 113

4.21 Results from PrMCRT simulations with particles of various scattering and absorption properties. The changes in particle optical properties with respect to material properties are overlaid. The experimentally measured transmission for this case is shown as a single contour line. 113
4.22 Results from PrMCRT simulation with particles of various scattering and absorption properties. The changes in particle optical properties with respect to material properties are overlaid. 114
4.23 Renderings of additional particles added to channel side walls, only a 5 mm slice in the flow direction is rendered. 114
4.24 Example of predicted transmission with additional particles added to the channel walls. An estimate for the number of bound particles is performed by solving a linear fit at the experimentally measured transmission. 115
5.1 Rate constants for all four chemistry rates as a function of temperature. Note that the Modified Hidgon chemistry has the same dissociation rate as the orginal Higdon model. 132
5.2 Rates for the $n = 1$ to $n = 2$ excitation of atomic hydrogen compiled from several sources. 142
5.3 Rates for the $n = 1$ to $n = 3$ excitation of atomic hydrogen compiled from several sources. 143
5.4 Temperature contours of flow around model in Queensland experiment 150
5.5 Species densities along stagnation line of flow in Queensland experiment 151
5.6 Electron number densities along stagnation line 152
5.7 Temperatures along stagnation line 152
5.8 Overhead diagram of extracted lines of sight (LOS) used to predict the spatially resolved spectral radiance. The flow enters from above and impinges on the model. The predicted flow temperature contours are plotted, identical to the results in Figure 5.4a. Lines of sight are extracted normal to the flow towards the camera. The shadowing of the model is included. The camera convolution function is shown in figure 5.9. Although only nine lines are shown, 100 lines of sight are extracted. 153
5.9 Spatial Convulation function for radiance calulations based on experimental measuments. The resultant fit is a Voigt profile with a Gausian Half Width Half Value (HWHV) of 0.10868 mm and a Lorentizan HWHV of 0.032507 mm. 153
5.10 Spatial and spectral contour on the prediced spetral radiance of the Queesnland experiment using Higdon chemiry and Boltman excited states. No convolution is performed 154
5.11 Same as Figure 5.10, however the spatial convolution from Figure 5.9 is performed. 155
5.12 Radiance profiles measured along stagnation steamline with instrument convolution, intensity is averages around the $H\alpha$ band ($476nm-497nm$). Measurements place the shock at $-1.185cm$. 155
5.13 Radiance profiles measured along stagnation steamline with instrument convolution, intensity is averages around the $H\alpha$ band (476 nm - 497 nm). Data is identical to Figure 5.12, but scale is logarithmic. 156
5.14 Radiance profiles measured along stagnation steamline without instrument convolution, intensity is averages around the $H\beta$ band (640 nm - 670 nm). 156

5.15 Radiance profiles measured along stagnation with instrument convolution, intensity is averages around the $H\beta$ band ($640nm - 670nm$). 157
5.16 Radiance profiles measured along stagnation with instrument convolution, intensity is averaged around the $H\beta$ band ($640nm - 670nm$). Data is identical to Figure 5.15, but scale is logarithmic. 157
5.17 Estimated radiative heat transfer to the stagnation point of the flow. These are estimated as π times the radiative heat flux along the stagnation line. One can see that the radiative heat flux spans an order of magnitude depending on the CFD chemistry and excited state model. 158
5.18 Number densities of species in flows representing Shot 18 conditions with different CFD chemistry models. 161
5.19 Number densities of species in flows representing Shot 22 conditions with different CFD chemistry models. 162
5.20 Temperatures in flows representing Shot 18 conditions with different CFD chemistry models 163
5.21 Temperatures in flows representing Shot 22 conditions with different chemistry models 164
5.22 Number densities of electrons of flow in the Shot 18 conditions with various chemical models 165
5.23 Number densities of electrons in flow of the Shot 22 conditions with various chemical models 165
5.24 Experimental measurements from EAST for Shot 18 conditions. Note that the IR reagion (far right) is nearly at the intrument noise floor. 166
5.25 Experimental measurements from EAST for Shot 22 conditions 167
5.26 High resolution plot of the atomic hydrogen 656 nm peak (β emission) for Shot 18. The Boltzmann and QSS results for each CFD chemistry are plotted sperately. 168
5.27 High resolution plot of the atomic hydrogen 656 nm peak (β emission) for Shot 22. The Boltzmann and QSS results for each CFD chemistry are plotted sperately. 169
5.28 Integrated radiance with respect to position over the EAST wavelength bands. The modeled lines compare the Boltzmann and QSS models for the Shot 22 conditions with the same underlying CFD chemistry (Higdon rates). 170
5.29 Integrated radiance as a function of a position for Shot 18, include all QSS predictions. Each EAST spectal region is plotted seperately. 171
5.30 Integrated radiance as a function of a position for Shot 22, include all QSS predictions. Each EAST spectal region is plotted seperately. 172
5.31 Spectral signal averaged over the 2 cm behind the Shot 18 shock. 173
5.32 Spectral signal averaged over the 2 cm behind the Shot 22 shock. 173
5.33 High resolution plot of the atomic hydrogen 656 nm peak (β emission) for Shot 18 including only QSS results. 174
5.34 High resolution plot of the atomic hydrogen 656 nm peak (β emission) for Shot 22 including only QSS results. 174

LIST OF TABLES

TABLE

4.1 Tabulated properties of nickel particles used in simulation modeling 81
4.2 Calculated transmission comparing various emitter models. 92
4.3 Transmission results for multiple heating and mass load cases, followed by the number of particles necessary to be added to the wall to match experimental measurements. 111
5.1 Freestream conditions in the simulations. 124
5.2 Conditions for East data. 126
5.3 H_2-He mixture reaction rate coefficients. The rates proposed by Higdon et al. [130] have multiple co-efficients for some reactions. All rate co-efficients were analyzed in the comparison study and we found that the results did not vary among the co-efficients. The baselines rates are reported here. 131

ABSTRACT

Electromagnetic waves are used in two distinct ways, to transmit information and to carry energy. For aerospace applications, the use of optical methods is excellent for making high fidelity measurements. High temperature flows, such as those found during atmoshperic entry, can also experience significant radiative heat transfer. This energy can lead to added heat loads to vehicles and, in extreme cases, alter the flow chemistry. Radiative transfer can also be affected by the addition of particulate material in the flow. These particles can form optically thick clouds which dramatically affect the flow properties through the process of absorption and scattering.

This work is divided into two principal parts. The first part analyzes the various aspects of radiative transfer in a heated particle laden flow. This includes a summary of methods used to estimate the optical properties of individual particles, as well as the developments to calculate the optical properties of large absorbing particles. This is followed by an analysis of radiative transfer through groups of particles. It is found that the Beer Law can suffer inaccuracies at high particle densities or very fine mesh resolutions. These results are used to develop a Monte Carlo ray tracing (MCRT) framework to analyze the radiative transfer through a particle laden flow, and validate coupled simulations of the system.

The second part of this work discusses hydrogen helium flows at atmospheric entry conditions experienced in the outer gas giants. A non-Boltzmann method to estimate excited states is developed. This is used to analyze chemical models used for computational fluid dynamics (CFD) simulations of these flows and validate them against experimental measurements. It is found that no current CFD chemistry models accurately predict the flow chemistry, likely due to discrepancies in the ionization rate of hydrogen.

CHAPTER 1

Introduction

There are few physical phenomena that life depends on as heavily as light. It is through light that our eyes interpret the natural world, and sight is arguably the most complex sense that humans possess. A single "element" of light requires information on position, direction, spectrum, and polarization in order to be fully defined. Electromagnetic waves are a valuable tool for analysis and communication.

Light not only exists as a means to transport information but also as a carrier of energy. Before the invention of fire, the sun's radiative energy was ancient man's only heat source. Currently, electromagnetic heating is an essential part of modern society, especially after Gould's invention of the laser in the late 1950's [1]. However, the laser is still used just as heavily as a tool for communication. This duality of light as source of information and energy makes understanding electromagnetic transport a necessary component of any field of study, including aerospace engineering.

Because light has the ability to transfer high-quality information it serves as one of the best tools to make experimental measurements of complex physical phenomena. Furthermore, models of physical systems (for this work, these systems will be fluid flows) are validated by predicting the system's optical properties. These can be directly compared against experiments. Optical transfer, or radiative transfer, is the process that permits a meaningful comparison between analytical or numerical prediction and experimental measurements. There are two ways these comparisons can be made. First, there is the forward problem where one takes numerical predictions of a complex physical system and then uses this information as input to a radiative transfer model. Radiative transfer measurements and predictions are directly compared. The most common application of solving the forward problem is computer graphics. The system is a modeled geometry and the radiative transfer model is used to generate an image that is displayed on a monitor.

The first numerical techniques to solve a radiative system were developed in the nuclear science [2]. This was followed by investigations in weather prediction [3] and astrophysics [4]. Aerospace-related analyses have generally neglected radiative energy transfer except at most extreme entry conditions and rocket nozzles. However, advanced imaging techniques such as Schlieren imaging were used nearly half a century before space flight [5,6]. Simulating these images is still an active area of research [7].

Although radiative transfer can be used to predict radiance data for comparison, one can also use the techniques to solve the backward problem. Experimental measurements and a radiative transfer model are used to determine the physics that is taking place. The reverse problem is almost always the more difficult because the number of degrees of freedom in the system is higher than the quantity of information that can be experimentally extracted. Solving the reverse problem is successfully performed as matter of course. Weather predictions, for example, use radar backscattering to determine the particle size distribution of clouds [3]. The electron densities of plasmas may be determined by the transmission of the plasma at radio frequencies [8].

Because radiative transfer has the ability to transfer energy, it can do work on a physical system. This has been known since the supposed ship burning mirrors of Archimedes [9]. We can distinguish two classes of problems that relate to this energy transfer. Firstly, there are problems where the energy transfer is negligible. One might call these imaging problems. These can still be difficult problems because the path of light may not be a straight line, as in scattering problems or problems of aberration. They are distinguished by the fact that the system does not change because of the radiative energy. However, the vast majority of physical systems respond to radiative heating. This response may be as simple as a rise in temperature. Nonetheless, the results of two concurrent physical processes must be solved for at once. This may appear obvious. For example, if the temperature of a solid material is an analytical function of its internal energy, those physical properties can be directly included into the radiative transfer equations leading to the science of radiative heat transfer [10]. However, if radiative transfer is coupled with a hydrodynamic system, complex fluid - radiation effects could arise.

This body of work will focus on the flow, distribution, and magnitude of radiative energy in fluid systems that are highly coupled. Both of these systems are paired with experimental measurements. High fidelity radiative transfer simulations are used to compare results from the system simulation (usually a fluid simulation) to experimental measurements (the forward problem) or use the experimental measurements to deduce errors that may exist in the original simulation (the backward problem). The objective of these studies is twofold, to validate the numerical models which generate the numerical inputs to the radiative transport model, and to determine the required fidelity of the radiative transport model for a fully coupled simulation.

1.1 Multiphase Flows

The following three chapters of this work concern various aspects of a multiphase flow. Multiphase flow is a type of flow where different materials are present and do not mix in a way that the fluid can be approximated as a single homogenous fluid. Examples of such flows are liquids with gaseous bubbles, gases with entrained droplets, dust, soot, or aerosol-laden flows (particle-laden flows).

Particle laden flows have appeared in several disciplines ranging from biomedical [11] simulation to aircraft noise reduction [12], but are very difficult to analyze because the particle can have a different velocity than the surrounding fluid. The drag force that couples the particles to the fluid is inherently non-linear. Furthermore, more particle-laden flows can contain millions of particles. The memory requirements necessary to store all of the position data can be large, and the computation power to simultaneously solve the nonlinear motions of all of the particles (and the fluid) can be cost-prohibitive. (Approximate methods for solving these flows can be found in References [13–21])

The addition of particles to turbulent flows has recently gained attention [15, 22–25]. It has been found that the addition of particles generally attenuates turbulent fluctuations [26]. However, turbulent kinetic energy can increase near the wall of channel flows [27]. Furthermore, these nonlinear motions tend to produce highly irregular arrangements of particles [28].

Turbulent particle laden flows experience strong thermal mixing. It has been hypothesized, for example, that it could be used to reduce the temperature of strongly irradiated solids, reducing the total energy loss due to emission [29]. This would make a particle laden flow and attractive working fluid for solar energy collectors [30].

The clustering that occurs in particle laden flows can have important ramifications for the radiative transfer properties. It is known that a tight grouping of particles absorbs less radiative energy than if those particles are uniformly spread out [31]. This can be explained as a simple problem of shadowing. In the extreme case, one can imagine a line of particles that directly shadow one another. Only the first particle would absorb any light.

Determining the final effectiveness of such a system relies on analyzing a three-way *coupled* system of radiative absorption, particle motion, and fluid turbulence. Recent work has been done to develop an experiment to validate simulation of these systems [32]. This work focuses on the radiative transfer aspects of such a system. The principal question is, given a complex arrangement of clustered particles what is the distribution of energy that is absorbed by the particles and how much energy is transmitted. There are three principal uncertainties, the necessary fidelity of geometry, not only of the particles, but the energy sources and sensors, the necessary fidelity of the radiative transfer model through the particle cloud itself, and lastly the accurate quantification of the optical properties of the particles themselves.

The optical properties of individual particles are an area of study in their own right [33]. The earliest treatment of scattering of particles was performed by Lord Rayleigh, who famously used scattering theory to explain the color of the sky. Gustav Mie and Hendrik Lorentz both analyzed the scattering of light from a dielectric sphere which was used to explain the coloration of metal particle suspensions [34, 35]. Although scatterings can be treated with analytical, classical methods, numerical methods are necessary to predict the optical properties of particles of complex geometry [36]. For a particle-laden flow, accurate prediction of the optical properties of the particles is critical to analyzing the radiative properties of the system as a whole.

1.2 Reacting Flows

The fifth chapter of this dissertation uses radiative transfer models to analyze a different flow regime: a high temperature reacting flow. For multiphase flows, the distinctive uncertainty is the geometric location of absorbers and scatterers and how much radiative energy flows through these stochastic structures. Reacting flows generally can be considered as homogeneous fluids, however, the radiative properties are highly dependent on species concentration in the fluid. Analyzing the specified concentrations from radiative signatures is done by examining the emitted spectrum [37,38]. The radiated spectrum can be calculated from a flow field by determining the rate of molecular and atomic transitions in the flow.

This work focuses on flow experience in atmospheric entry conditions. When an orbital vehicle descends to a planet's surface it must transfer its kinetic energy to heating the atmosphere. In practice, this results in a strong shock layer which forms between the body and the free atmosphere. The critical design aspect for these vehicles is sufficiently protecting them from the thermal loads.

At low speeds, the heat transfer from these flows is primarily convective. However, as the vehicle speed increases, the shock strength increases, raising the post shock temperature. For a calorically perfect gas the rise in temperature scales as the square of the velocity (at large Mach numbers). Radiative emission scales as temperature to the fourth power. One can estimate that the radiative emission from the flow then scales as temperature to the eighth power (In reality, chemical effects reduce this to approximately the fourth power). Therefore, there is a rapid transition from a convection dominated flow to a radiatively dominated flow.

Radiative effects are still important at low temperatures because they can be used to diagnose a flow via its spectrum and therefore the composition. This has been used to analyze the chemical composition of entry conditions in Earth [39, 40], Mars [41], and Titan [41]. Furthermore, a small radiative heating component on the unprotected rear surfaces of entry vehicles has been found to exist [42–45].

The source of uncertainty in this high speed flows is chemical nonequilibrium. As the flow passes through the shock, a rapid temperature change energizes the atoms and molecules, leading to excitation, dissociation, and ionization. The composition tends toward a new equilibrium condition, but as it does so it moves rapidly through the flow. The chemical compositions then depend on location in space. Qualities of interest, notably heat transfer [46] and spectral radiance [39] are highly dependent on this chemical composition.

Nonequilibrium is difficult to analyze because it requires knowledge of the *rates* at which chemical processes occur. For radiative transfer, the emission is dependent on the population of each excited state, and each state is in nonequilibrium. The resultant distribution of excited states is considered non-Boltzmann. The necessary computational power and data required to completely calculate such a system has slowly been developed over recent decades [40, 47, 48].

This work will focus on gas giant atmospheres such as Uranus or Saturn. The specifics of these flows and synopsis of previous work is given in Section 5.1. Unlike other atmospheres, Uranus and Saturn contain mostly Hydrogen and Helium and therefore require their own unique chemical models. Although granular chemical models exist, no non-Boltzmann model has been developed to predict the spectral emission from high temperature flows of this composition. In this work, a new non-Boltzmann model of atomic and molecular excitation is developed and used to evaluate the emitted spectrum from simulated flows. These spectra can then be directly compared against experiments to assess the accuracy of the chemical models used in the original fluid simulation. This work represents the first evaluation of hydrogen chemical models using these modern techniques.

1.3 Dissertation Outline

The following five chapters are organized as follows. Chapter 2 discuss the relevant electromagnetic theory to determine the optical properties of particles. Chapter 3 turns to analyze the optical properties of groups of particles and the appropriateness of continuum assumptions. The work of the previous two chapters is used in Chapter 4, where a particle-laden flow is analyzed and validated against experimental data. This includes the development of a fully particle resolved Monte Carlo Ray tracing framework.

Chapter 5 turns toward a reacting hydrogen-helium flow, similar to that expected in entry conditions on outer gas giants. Radiative transfer predictions are used to assess the accuracy of multiple aerothermochemistry models for these types of flow. Finally, Chapter 6 summarizes the work of the previous chapters and highlights physical processes and numerical methods that warrant further study.

CHAPTER 2

Electromagnetic Waves and Particulates

2.1 Background

Whenever two objects of particular momentum interact, their momentum is likely to change. In fact for many classes of objects, an interaction can be defined as an event which causes the objects to change momentum. Energy transfer is also likely to occur, either by an exchange of kinetic energy from one object to another, or if the objects have internal energy storage (i.e. rotational or thermal energy), the interaction can reduce the total kinetic energy of both objects.

The vague term "object" is used here because this process can be found in many fields concerning many objects, be they two astronomical bodies interacting by gravitation or two electrons under the influences of their electric field. This pairwise interaction is foundational. Complex systems can often be analyzed by reducing the system to a series of these interactions.

One can consider a subset of these interactions: ones where one body is much more massive than the other. In this case the lighter particle interacts with the heavier particle in such a way that the change of momentum of the heavy particle is slight and can be taken as zero, while the lighter particle can drastically change direction. This process will be referred to as scattering.

This chapter will focus on the scattering of photon beams against macroscopic objects, hereafter called particles or particulates. Photons, and especially beams of photons, are best treated as waves with classical electromagnetic theory. This chapter begins by introducing the governing equations, followed by a discussion of several analytical solutions. Finally, several methods will be introduced for computing the scattering of particles too complex to be analytically solved for, but instead require numerical approaches.

2.2 Time Harmonic Maxwell Equations

Any classical electromagnetic theory must begin with some form of the Maxwell equations. This work will use the macroscopic Maxwell equations in macroscopic form. These are given as

$$\begin{aligned} \nabla \cdot D &= \rho \\ \nabla \cdot B &= 0 \\ \frac{\partial D}{\partial t} &= j + \nabla \times H \\ \frac{\partial B}{\partial t} &= -\nabla \times E \end{aligned} \tag{2.1}$$

where D is the electric displacement, E is the electric field, B is the magnetic induction and H is the magnetic field. The values ρ and j represent the free charge density and current respectively. The macroscopic form allows for the background to be a homogenous material that is not vacuum. The material properties are formulated as the relationship between the electric displacement and electric field and between the magnetic induction and magnetic field. Furthermore, the material must provide a relationship between the charge current, the charge density, and the electromagnetic fields. For this dissertation the material properties will be inserted as a conductivity, σ, an electric susceptibility χ, and a magnetic permeability μ, which define the displacement, induction and current as

$$\begin{aligned} D &= (1+\chi)\epsilon_0 E \\ B &= \mu H \\ j &= \sigma E \end{aligned} \tag{2.2}$$

The permittivity and permeability of vacuum are defined as ϵ_0 and μ_0 respectively. Maxwell's equations can now be simplified to the forms more useful for discussing macroscopic scattering.

$$\begin{aligned} \nabla \cdot (1+\chi)\epsilon_0 E &= \rho \\ \nabla \cdot \mu H &= 0 \\ (1+\chi)\epsilon_0 \frac{\partial E}{\partial t} &= \sigma E + \nabla \times H \\ \frac{\partial \mu H}{\partial t} &= -\nabla \times E \end{aligned} \tag{2.3}$$

The fields E and H are functions of both time and space. When discussing optical scattering, one is interested in the scattering of one particular color or frequency. This can be achieved by introducing a time harmonic solution of the form

$$\begin{aligned} E(\vec{x},t) &= E(\vec{x})e^{-i\omega t} \\ H(\vec{x},t) &= H(\vec{x})e^{-i\omega t} \end{aligned} \tag{2.4}$$

where ω is the frequency of oscillation, t is time, and i is the imaginary unit. This simplification reduces Maxwell's equations to the following

$$\begin{gathered} \nabla \cdot (1+\chi)\epsilon_0 E = \rho \\ \nabla \cdot \mu H = 0 \\ -i\omega(1+\chi)\epsilon_0 E = j + \nabla \times H \\ -i\omega\mu H = -\nabla \times E \end{gathered} \tag{2.5}$$

Further simplification can be performed by recognizing the time harmonic conservation of charge, $i\omega\rho = \nabla \cdot j$, and by defining the complex permittivity, ϵ as

$$\epsilon(\omega) = \epsilon_0(1+\chi) + i\frac{\sigma}{\omega} \tag{2.6}$$

the time harmonic Maxwell equation can be reduced to

$$\begin{aligned}
\nabla \epsilon E &= 0 \\
\nabla \cdot \mu H &= 0 \\
-i\omega\epsilon E &= \nabla \times H \\
i\omega\mu H &= \nabla \times E
\end{aligned} \tag{2.7}$$

Further discussion of the complex permittivity is given below (Section 2.3.1). Substituting the latter two equations into each other yields

$$\begin{aligned}
\omega^2\epsilon\mu E + \nabla^2 E &= 0 \\
H &= \frac{-i}{\omega\mu}\nabla \times E
\end{aligned} \tag{2.8}$$

The first equation will be referred to as the wave equation. Notice that H is not independent of E. Also notice that the wave equation is linear (i.e. if E_1 is a solution to the wave equation as is E_2 then $E_1 + E_2$ is a solution).

2.3 Material Properties

Equations 2.2 and 2.6 introduced the constitutive relations, relating the electric displacement to the electric field and the magnetic induction to the magnetic field. These relations are integral to describing a macroscopic material. Although all materials can in theory be analyzed using these relations, further models can be developed for particular classes of materials. This work will focus on two broad categories, dielectrics and imperfect conductors.

2.3.1 Dielectrics

Dielectrics exhibit the effect of polarization in an electric field. When a field is applied, the electrons of the material displace relative to their nucleus in the direction opposite to the electric field. This serves, on average, to negate the field inside the medium. How this polarization is set up in the medium can be a complex function of the electric field, dependent on the strength of the field and its orientation to the material (this is specifically relevant to polarized crystals). For this work, however, all materials will be assumed to be linear isotropic materials. That is to say that the permitity is linearly related to a single scalar.

$$\epsilon = \epsilon_0(1+\chi) \tag{2.9}$$

where χ, the susceptibility, is a real constant, and therefore ϵ is a constant.

Equation 2.9 is a useful model for electrostatics, where the polarization is set up and held. However, for time harmonic electrodynamics, one must also account for the fact that the polarization takes a finite time to set up in the material. During this process electrons are moving, on average, from one side of the atom to the other. This motion appears like a free current which induces a curl in the magnetic field. This added current can be directly included into the formulation of ϵ as

$$\epsilon(\omega) = \epsilon_0(1+\chi) + i\frac{\sigma}{\omega} \tag{2.10}$$

Note that the permittivity is a function of the frequency of oscillation ω in the imaginary part.

The electric permittivity is not a unitless property; it is related to a unitless parameter, the index of refraction. The index of refraction, **n**, is defined as the speed of light in a medium compared to the speed of light in free space.

$$\mathbf{n} = c\sqrt{\epsilon\mu} \tag{2.11}$$

assuming that $\mu = \mu_0$

$$\mathbf{n} = \frac{\epsilon}{\epsilon_0} \tag{2.12}$$

The index of refraction simplifies the underlying mathematics. For example, the wave equations (Equation 2.8) reduce to

$$\begin{aligned} (\mathbf{n}k)^2 E + \nabla^2 E &= 0 \\ H &= \frac{-i}{\omega\mu}\nabla \times E \end{aligned} \tag{2.13}$$

where k is the wavenumber of light in vacuum, and $\mathbf{n}k$ is identified as the wavenumber of light in the medium ($kc = \omega$). Note this is equivalent to saying that the index of refraction of vacuum is $1 + 0i$. The wavelength in the medium is then

$$\lambda = \frac{2\pi}{\mathbf{n}k} \tag{2.14}$$

where λ is the wavelength.

2.3.2 Conductors

In electrostatics, there is a categorical difference between a dielectric and a conductor. A dielectric exhibits a displacment of bound electrons while a conductor permits the flow of free electrons. However, in the time harmonic form, the motion of bound electrons and the constant reversal of free electrons due to the oscillating field make the two materials appear more and more mathematically similar. The dielectric properties of materials normally categorized as conductors are known and tabulated for time harmonic fields. Note, that a perfect conductor has a permittivity of $\epsilon = i\infty$, however, the resistivity of most materials in the optical range is usually large enough that the magnitude of the index of refraction is less than 10.

The high frencency impedance in conductors does not rescind one of the most notable characteristics of conductors, the development of skin currents on their surface. These currents, set up just inside the surface (with a penetration depth called the skin depth), reduce the field, and therefore the current, that exists deeper in the material. For a perfect conductor this yields the well known result that currents do not exist in any volume element [49]. For imperfect conductors, the skin effect can be captured in time harmonic oscillation with the above formation of the index of refraction. However, the small size of these skin currents make their numerical calculation very difficult. This can necessitate a simplified model of these currents as a two dimensional phenomenon. The associated material property for this model is the surface impedance.

When the electric field only penetrates a small depth (the skin depth) into a material, setting up a thin (i.e. two dimensional) layer of current near the surface, a tangential magnetic field is induced in response. Without directly calculating the field inside the conductor, one can arrive at a boundary condition just above the surface that takes the form.

$$E = Z(\hat{n} \times H) \tag{2.15}$$

where $\hat{n}$ is the unit vector normal to the surface and Z is the surface impedance. This formulation assumes that the surface is flat. For a particle, this approximation is most accurate when the skin depth is small relative to the local radius of curvature of the particle. The skin depth is defined as

$$\delta = \sqrt{\frac{2}{\mu\omega\sigma}} \tag{2.16}$$

where μ is the magnetic permeability, ω is the frequency, and σ is the conductivity. Neglecting the anomalous skin effect, the conductivity can be alternatively expressed as

$$\sigma = i\omega\epsilon = i\omega\epsilon_0\mathbf{n}^2 \tag{2.17}$$

where ϵ is the particle permittivity and $\mathbf{n}$ is the index of refraction. This permits converting an index of refraction into surface impedance and skin depth:

$$Z = \frac{Z_0}{\mathbf{n}}; \delta = \frac{1}{k\Im(\mathbf{n})} \tag{2.18}$$

where Z_0 is the characteristic impedance for free space, $\Im(\mathbf{n})$ is the imaginary part of the index of refraction, and k is the wave number in vacuum.

2.4 Spherical Harmonic Conventions: Past and Present

Because the wave equations are linear, there exists a straightforward strategy to solve classical scattering problems by decomposing the field into harmonics. This process reduces a series of partial differential equations into a problem of linear algebra.

Because scattered light moves radially from a particle (in the far field), the scattering problem is often solved in spherical coordinates with a series of spherical harmonics. The coordinates are r, θ and ϕ where r is the radius, θ is the zenith angle measured from the z axis, and ϕ is the azimuthal angle from the x axis. r can be nondimensionalized into $\rho = kr$ where k is defined as $\omega\sqrt{\epsilon\mu}$.

Any vector harmonic solution to the wave equation takes the form of two orthogonal sets of functions, each with a pair of independent indices. However, there is no unique expansion of the fields. Two principal expansions have evolved, one that has been used for analytical solutions and one that is better suited for numerical solutions (e.g. the extended boundary method in Section 2.6.2).

2.4.1 Classical Spherical Harmonic Expansion

The classical method (following Borhen [33] and Statton [50]) of spherical harmonic decomposition reduces a field E ocilating as $e^{-i\omega t}$ into a linear combination of four functions

$$\begin{aligned}
M_{emn} =& \frac{-m}{sin(\theta)} sin(m\phi) P_n^m(cos(\theta)) z_n(\rho)\hat{\theta} + \\
& - cos(m\phi) \frac{dP_n^m(cos(\theta))}{d\theta} z_n(\rho)\hat{\phi} \\
M_{omn} =& \frac{-m}{sin(\theta)} cos(m\phi) P_n^m(cos(\theta)) z_n(\rho)\hat{\theta} + \\
& - sin(m\phi) \frac{dP_n^m(cos(\theta))}{d\theta} z_n(\rho)\hat{\phi} \\
N_{emn} =& \frac{z_n(\rho)}{\rho} cos(m\phi) n(n+1) P_n^m(cos(\theta)) z_n(\rho)\hat{\rho} + \\
& cos(m\phi) \frac{dP_n^m(cos(\theta))}{d\theta} \frac{d\rho z_n(\rho)}{d\rho} \hat{\theta} + \\
& - \frac{-m}{sin(\theta)} sin(m\phi) P_n^m(cos(\theta)) \frac{d\rho z_n(\rho)}{d\rho} \hat{\phi} \\
N_{omn} =& \frac{z_n(\rho)}{\rho} sin(m\phi) n(n+1) P_n^m(cos(\theta)) z_n(\rho)\hat{\rho} + \\
& sin(m\phi) \frac{dP_n^m(cos(\theta))}{d\theta} \frac{d\rho z_n(\rho)}{d\rho} \hat{\theta} + \\
& - \frac{-m}{sin(\theta)} cos(m\phi) P_n^m(cos(\theta)) \frac{d\rho z_n(\rho)}{d\rho} \hat{\phi}
\end{aligned} \tag{2.19}$$

where P_n^m is the associated Legendre polynomial, $z_n(\rho)$ is a spherical Bessel function, and n and m are natural numbers with $m \leq n$. o and e mean even and odd functions, which are used instead of allowing m to become negative. The Einstein convention of summing over like indices is implied. The associated Legendre polynomials have two conventions regarding the Condon-Shortley phase factor (a factor of -1^m). The old convention, which doesn't include that factor, states that if $cos(\theta) = 1$, then $\frac{dP_n^m(cos(\theta))}{dcos(\theta)}$ is negative for all m except $m = 0$.

This a general solution for an electromagnetic wave in a linear isotropic medium (i.e. as a solution to Equation 2.8) would be

$$\begin{aligned} E &= a_{enm}M_{emn} + a_{onm}M_{omn} + b_{enm}N_{emn} + b_{onm}N_{omn} \\ H &= \frac{-ki}{\omega\mu}\left(a_{enm}N_{emn} + a_{onm}N_{omn} + b_{enm}M_{emn} + b_{onm}M_{omn}\right) \end{aligned} \tag{2.20}$$

using the fact that $\nabla \times N = kM$ and $\frac{\partial \mu H}{\partial t} = -\nabla \times E$.

2.4.2 Modern Spherical Harmonic Expansion

Another convention born originally from group theory (following Mishchenko [51], [52]) is presented. A given electric field, E, and magnetic field, H, oscillating as $e^{i\omega t}$ can be expanded as

$$E = \sum_{n=0}^{\infty}\sum_{m=-n}^{n} a_{nm}M_{nm}^{(i)} + b_{nm}N_{nm}^{(i)};\ H = \frac{-ik}{\omega\mu}\sum_{n=0}^{\infty}\sum_{m=-n}^{n} a_{nm}N_{nm}^{(i)} + b_{nm}M_{nm}^{(i)} \tag{2.21}$$

$$M_{nm}^{(i)}(\rho,\theta,\phi) = d_n z_n^{(i)}(\rho)(\pi_{nm}(\theta)\hat{\theta} - \tau_{nm}(\theta)\hat{\phi})e^{im\phi} \tag{2.22}$$

$$N_{nm}^{(i)}(\rho,\theta,\phi) = d_n\left(\frac{n(n+1)z_n^{(i)}(\rho)d_{0m}^{\ n}(cos(\theta))}{\rho} + \frac{1}{\rho}\frac{d(\rho z_n^{(i)}(\rho))}{d\rho}(\tau_{nm}(\theta)\hat{\theta} + \pi_{nm}(\theta)\hat{\phi})\right)e^{im\phi} \tag{2.23}$$

$$\pi_{nm}(\theta) = \frac{im}{sin(\theta)}d_{0m}^{\ n}(cos(\theta)) \tag{2.24}$$

$$\tau_{nm}(\theta) = \frac{d}{d\theta} {d_{0m}}^{n}(cos(\theta)) \tag{2.25}$$

$${d_{0m}}^{n} = -1^{m} \sqrt{\frac{(n-m)!}{(n+m)!}} P_{n}^{m}(\theta) \tag{2.26}$$

$$d_n = \sqrt{\frac{2n+1}{4\pi n(n+1)}} \tag{2.27}$$

where k and ω are the wavenumber and frequency of the wave and μ is the magnetic permeability of the medium. ${d_{0m}}^{n}$, the Wigner functions (or matrix elements), are expressed in terms of $P_{n}^{m}(\theta)$, the associated Legendre polynomial (with the Condon-Shortley phase factor). $z^{(i)}(\rho)$ denotes a spherical Bessel function of the ith kind $(j(\rho), y(\rho), h^{(1)}(\rho), h^{(2)}(\rho)$ being the first, second, etc.). In this study, the incident field is always assumed to be expanded with the spherical Bessel function of the first kind $(j(\rho))$ and the scattered field with the spherical Hankel function of the first kind $(h^{(1)}(\rho))$.

In preparation for Section 2.6.2, the Green's function is given as

$$G(\vec{\rho_1}, \vec{\rho_2}) = ik \sum_{n=0}^{\infty} \sum_{m=-n}^{n} d_n \left(M_{nm}^{(3)}(\vec{\rho}_{>}) M_{nm}^{(1)}(\vec{\rho}_{<}) + N_{nm}^{(3)}(\vec{\rho}_{>}) N_{nm}^{(1)}(\vec{\rho}_{<}) \right) \tag{2.28}$$

where the $<$ and $>$ denote the vector with the smaller or larger radial component.

This form is more cumbersome to write out, but has consistent normalization and permits a less laborious analysis of harmonics.

2.5 Scattering of a Sphere

Using the above system of spherical harmonics, one begins with a field representing the incoming radiation labels E_{inc}. By including a scattering particle, another field is added to the outer region E_{scat} which represents the energy redistribution outside the particle due to the particle. For a dielectric particle a new field is also created that only exists inside the particle, E_{int}. When the incident field is given and the boundary conditions on the particle are known, the fields E_{scat} and E_{int} are uniquely defined.

2.5.1 Dielectric Sphere

The scattering of a sphere is a standard problem in classical electrodynamics. The problem was first treated by Lorentz and Mie and the solution is often referred to as Mie scattering. The solution to this problem is presented in Stratton [50], Jackson [49], and Borhen [33]. Borhen's convention is the more common, and it will be presented here.

The solution to the electromagnetic scattering problem begins with the expansion of a linearly polarized plane wave for the incident field followed by expansions with unknown coefficients for the internal and scattered fields.

$$\begin{aligned}
E_{inc} &= E_0 i^n \frac{2n+1}{n(n+1)} \left(M_{o1n} - i N_{e1n}\right) \\
E_{int} &= E_0 i^n \frac{2n+1}{n(n+1)} \left(c_n M_{o1n} - i d_n N_{e1n}\right) \\
E_{scat} &= E_0 i^n \frac{2n+1}{n(n+1)} \left(-b_n M_{o1n} + i a_n N_{e1n}\right)
\end{aligned} \tag{2.29}$$

For a plane wave the incident field only exists in the $m = 1$ modes. Half of the even or odd modes (representing the orthogonal polarization) also have no magnitude in this expansion. The boundary condition at the particle surface is that the component of the field tangent to the particle is equal on both sides of the interface. The normal component changes due to the particle's material polarization.

The boundary condition at the particle surface enforces that the tranjectial fields are equal, symbolically written as

$$\begin{aligned} \hat{n} \times (E_{inc} + E_{scat}) &= \hat{n} \times E_{int} \\ \hat{n} \times (H_{inc} + H_{scat}) &= \hat{n} \times H_{int} \end{aligned} \tag{2.30}$$

where $\hat{n}$ is the normal to the surface (equal to $\hat{\rho}$ for a sphere). The solution for the scattering field of this problem is

$$\begin{aligned} a_n &= \frac{m\psi_n(mx)\psi'(x) - \psi_n(x)\psi'(mx)}{m\psi_n(mx)\xi'(x) - \psi_n(x)\xi'(mx)} \\ b_n &= \frac{\psi_n(mx)\psi'(x) - m\psi_n(x)\psi'(mx)}{\psi_n(mx)\xi'(x) - m\psi_n(x)\xi'(mx)} \end{aligned} \tag{2.31}$$

where $m = \frac{\mathbf{n_{int}}}{\mathbf{n_{ext}}}$ is the particle index of refraction (the internal index) relative to the external medium, $\Psi_n(x)$ and $\xi_n(x)$ are the Riccati-Bessel functions $\Psi_n(x) = xj_n(x)$ and $\xi_n(x) = xh_n^{(1)}(x)$.

One of the first quantities of interest is the radiative power that is scattered by the particle and the quantity that is absorbed. It is easier to analyze two fields, the external field ($E_{ext} = E_{inc} + E_{scat}$) and the scattered field alone. The energy flow at any point in space is related to the Poynting vector, S.

$$S = E \times H \tag{2.32}$$

Which, when time averaged becomes

$$S = \frac{1}{2}\Re(E \times H^*) \tag{2.33}$$

where $\Re$ is the real part and H^* is the complex conjugate of the magnetic field. The total power scattered for example is

$$W_{scat} = \frac{1}{2}\int S * \hat{n} d\Omega \tag{2.34}$$

where Ω is the solid angle ($d\Omega = sin(\theta)d\theta d\phi$). This reduces to

$$W_{scat} = \frac{\pi E_0^2}{k\omega\mu}\sum_n ((2n+1)(a_n a_n^* + b_n b_n^*)) \tag{2.35}$$

This total power can be normalized by the incident energy flux, I_0, which is related to the field parameters as

$$I_0 = \frac{\epsilon_0}{2c}E_0^2 \tag{2.36}$$

The division of a power by an energy flux yields a quantity of unit area, called the cross section. The scattering cross section, σ_s is then

$$\sigma_s = \frac{W_{scat}}{I_0} = \frac{\pi}{k^2}\sum_n ((2n+1)(a_n a_n^* + b_n b_n^*)) \tag{2.37}$$

These cross sections are entirely abstract values, but can be normalized to the geometric cross sections (σ_g) of the particle to yield the efficiency. For example the scattering efficiency is

$$Q_s = \frac{\sigma_s}{\sigma_g} = \frac{2}{\chi^2}\sum_n((2n+1)(a_n a_n^* + b_n b_n^*)) \tag{2.38}$$

Likewise the same procedure over the external field yields the extinction efficiency, a measure of the total energy flow disrupted by the particle.

$$Q_e = \frac{2}{\chi^2}\sum_n((2n+1)\Re(a_n + b_n)) \tag{2.39}$$

the absorption efficiency is simply $Q_a = Q_e - Q_s$.

If however, one is interested in the exact distribution of energy with regards to angle, further calculation and simplification is necessary. First the energy distribution is only calculated in the far field, where the Hankel function reduces to spherical waves. The electric field is then

$$\begin{aligned} E_{s\theta} &= E_0\frac{2n+1}{n(n+1)}\frac{e^{ikr}}{-ikr}(a_n\frac{dP_n^1(cos(\theta))}{d\theta} + b_n\frac{P_n^1(cos(\theta))}{sin(\theta)})cos(\phi) \\ E_{s\theta} &= -E_0\frac{2n+1}{n(n+1)}\frac{e^{ikr}}{-ikr}(a_n\frac{P_n^1(cos(\theta))}{sin(\theta)} + b_n\frac{dP_n^1(cos(\theta))}{d\theta})sin(\phi) \end{aligned} \tag{2.40}$$

or

$$\begin{aligned}
E_{s\theta} &= E_0 S_2 \frac{e^{ikr}}{-ikr} cos(\phi) \\
E_{s\theta} &= -E_0 S_1 \frac{e^{ikr}}{-ikr} sin(\phi) \\
S_1(\theta) &= \frac{2n+1}{n(n+1)}(a_n \frac{P_n^1(cos(\theta))}{sin(\theta)} + b_n \frac{dP_n^1(cos(\theta))}{d\theta}) \\
S_2(\theta) &= \frac{2n+1}{n(n+1)}(a_n \frac{dP_n^1(cos(\theta))}{d\theta} + b_n \frac{P_n^1(cos(\theta))}{sin(\theta)})
\end{aligned} \tag{2.41}$$

The polarization and energy distribution are dependent on both spherical angles. However, this is in part due to the fact that the incident field was taken as a linearly polarized plane wave of field strength E_0. One can also consider an unpolarized wave of the same strength by averaging over the azimuthal angle. The resultant energy distribution is then

$$I_s/I_0 = \frac{1}{2\chi^2}(|S_1(\theta)|^2 + |S_2(\theta)|^2) \tag{2.42}$$

Notice that the unpolarized scattering distribution is dependent only on the zenith angle.

Many scattering particles scatter in a roughly isotropic distribution with the addition of a large forward peak. If these small deflection scattering events are ignored, one can calculate the efficiency of only the isotropic scattering. The efficiency associated with the process, the isotropic scattering efficiency is defined as:

$$Q_{si} = Q_s(1-g) \tag{2.43}$$

where g is the asymmetry parameter. In this convention, g can be calculated as

$$g = \frac{4}{\chi^2}\left[\sum_n \left(\frac{n(n+2)}{n+1} Re(a_n a_{n+1}^* + b_n b_{n+1}^*)\right) + \sum_n \left(\frac{2n+1}{n(n+1)}(a_n b_n^*)\right)\right] \tag{2.44}$$

This is equivalent to only considering parts of the scattering function which have a corresponding part across the midplane of the particle.

2.5.2 Scattering from a Multilayered Sphere

The solution for a single homogenous, dielectric sphere has been solved for over a century [34]. However, inhomogeneous spheres have proven less straightforward to solve. The solution to a sphere of multiple radial layers had a solution [33], but that solution was shown to be numerically unstable [53]. This was especially true with small, absorbing layers existing on the outside of a dielectric sphere.

The solution to this problem is similar to the problem of a homogeneous sphere, however, instead of a single internal field, a new field is calculated for each of the l layers. The innermost layer, the core, is expanded with the spherical Bessel functions. The intermediate layers however, experience spherical waves transmitting both into and out of the particle. Therefore, they must be expanded with two sets of waves. For a linearly polarized incident wave, the fields take the form.

$$
\begin{aligned}
E_{inc} &= E_0 i^n \frac{2n+1}{n(n+1)} \left(M_{o1n} - iN_{e1n}\right) \\
E_0 &= E_0 i^n \frac{2n+1}{n(n+1)} \left(c_{0n}M_{o1n} - id_{0n}N_{e1n} + e_{0n}M_{o1n} - if_{0n}N_{e1n}\right) \\
E_1 &= E_0 i^n \frac{2n+1}{n(n+1)} \left(c_{1n}M_{o1n} + id_{1n}N_{e1n} + e_{1n}M_{o1n} - if_{1n}N_{e1n}\right) \\
&\dots \\
E_L &= E_0 i^n \frac{2n+1}{n(n+1)} \left(c_{Ln}M_{o1n} + id_{Ln}N_{e1n} + e_{Ln}M_{o1n} - if_{Ln}N_{e1n}\right) \\
E_{scat} &= E_0 i^n \frac{2n+1}{n(n+1)} \left(-b_nM_{o1n} + ia_nN_{e1n}\right)
\end{aligned}
\tag{2.45}
$$

where L is the number of layers. The boundary conditions of Equation 2.30 are held between each layer. The tangential components of all fields are continous across an interface.

The solution to such a problem is tractable and analytically available, however, it suffers from numerical instability. Terms emerge as part of the solution that appear as follows.

$$
\mathbf{n}_1\psi_n(\mathbf{n}_2\chi)\psi_n\prime(\mathbf{n}_1\chi) - \mathbf{n}_2\psi_n(\mathbf{n}_1\chi)\psi_n\prime(\mathbf{n}_2\chi) \tag{2.46}
$$

if $\mathbf{n}$ has an imaginary component, the size of $\psi_n(\mathbf{n}_2\chi)\psi_n\prime(\mathbf{n}_1\chi)$ may be over 15 orders of magnitude larger than their difference. This leads to enormous truncation errors for any numerical calculation. s Yang [53] provided an improved recursion algorithm that reduced these errors, by recasting the equations as a quotient instead a difference. This has enabled accurate calculation of particles with small layers. Furthermore, it remains usable for the case of one layer i.e. a homogeneous sphere. Yangs's algorithm can then be used as a complete replacement for Mie calculations using the previous mathematics.

Yang's paper does make the simplifying assumption that the relative magnetic permeability of the substance is 1.0. This is generally accurate in the optical range; however, for completeness, the algorithm can be altered as

$$
\begin{aligned}
A_{1n} &= 0 \\
Ha_{1n} &= D^{(1})_n(\mathbf{n}_1\chi_1)
\end{aligned}
$$

$$
\begin{aligned}
Ha_{ln} &= \frac{G_2 D_n^{(1)}(\mathbf{n}_l\chi_l) - Q_{ln}G_1 D^{(3)}(\mathbf{n}_l\chi_l)}{G_2 - Q_{ln}G_1} \\
A_{(l+1)n} &= R(\mathbf{n}_{l+1}\chi l)\frac{\mathbf{n}_{l+1}\mu_l Ha_{ln} - \mathbf{n}_l\mu_{l+1}D_n^{(1)}(\mathbf{n}_{l+1}\chi_l)}{\mathbf{n}_{l+1}\mu_l Ha_{ln} - \mathbf{n}_l\mu_{l+1}D_n^{(3)}(\mathbf{n}_{l+1}\chi_l)}
\end{aligned}
\tag{2.47}
$$

$$
a_n = A_{L+1}
$$

$$
\begin{aligned}
B_{1n} &= 0 \\
Hb_{1n} &= D^{(1})_n(\mathbf{n}_1\chi_1)
\end{aligned}
$$

$$
\begin{aligned}
Hb_{ln} &= \frac{G_4 D_n^{(1)}(\mathbf{n}_l\chi_l) - Q_{ln}G_3 D^{(3)}(\mathbf{n}_l\chi_l)}{G_4 - Q_{ln}G_1} \\
B_{(l+1)n} &= R(\mathbf{n}_{l+1}\chi l)\frac{\mathbf{n}_l\mu_{l+1}Hb_{ln} - \mathbf{n}_{l+1}\mu_l D_n^{(1)}(\mathbf{n}_{l+1}\chi_l)}{\mathbf{n}_l\mu_{l+1}Hb_{ln} - \mathbf{n}_{l+1}\mu_l D_n^{(3)}(\mathbf{n}_{l+1}\chi_l)}
\end{aligned}
\tag{2.48}
$$

$$
b_n = B_{L+1}
$$

$$\begin{aligned} D_n^{(1)}(x) &= \frac{\psi\prime_n(x)}{\psi_n(x)} \\ D_n^{(3)} &= \frac{\xi\prime_n(x)}{\xi_n(x)} \\ R_n &= \frac{\psi_n(x)}{\xi_n(x)} \end{aligned} \tag{2.49}$$

$$Q_{ln} = \frac{\psi(\mathbf{n}_l\chi_{l-1})\xi(\mathbf{n}_l\chi_l)}{\psi(\mathbf{n}_l\chi_l)\xi(\mathbf{n}_l\chi_{l-1})} \tag{2.50}$$

$$\begin{aligned} G_1 &= \mathbf{n}_l\mu_{l-1}Ha_n(\mathbf{n}_{l-1}\chi_{l-1}) - \mathbf{n}_{l-1}\mu_l D_n^{(1)}(\mathbf{n}_l\chi_{l-1}) \\ G_2 &= \mathbf{n}_l\mu_{l-1}Ha_n(\mathbf{n}_{l-1}\chi_{l-1}) - \mathbf{n}_{l-1}\mu_l D_n^{(3)}(\mathbf{n}_l\chi_{l-1}) \\ G_3 &= \mathbf{n}_{l-1}\mu_l Hb_n(\mathbf{n}_{l-1}\chi_{l-1}) - \mathbf{n}_l\mu_{l-1} D_n^{(1)}(\mathbf{n}_l\chi_{l-1}) \\ G_4 &= \mathbf{n}_{l-1}\mu_l Hb_n(\mathbf{n}_{l-1}\chi_{l-1}) - \mathbf{n}_l\mu_{l-1} D_n^{(3)}(\mathbf{n}_l\chi_{l-1}) \end{aligned} \tag{2.51}$$

where L is the total number of layers, and μ is the relative permeability.

2.5.3 Scattering from a Conducting Particle

The scattering of a sphere with a given surface impedance is given as an example in Jackson [49]. However, his notation differs from that primarily used in the scattering literature. The problem is set up as two sets of fields expanded in spherical harmonics: the incident field, E_{inc}, and the scattered field E_{scat}. These impinge on a sphere of radius r_0 with surface impedance Z. The incident field is taken as a plane wave polarized in the x direction moving in the z direction with field strength E_0 and wavenumber k [33]. In the current convention, this is expanded as

$$E_{inc} = E_0 \sum_n i^{n+1} \sqrt{\pi(2n+1)} \left(M_{n1}^{(1)} - N_{n1}^{(1)} + M_{n-1}^{(1)} + N_{n-1}^{(1)} \right) \tag{2.52}$$

Here the radial part of the harmonics M and N are taken as functions of kr_0 which is often called the size parameter, χ.

$$\chi = kr = \frac{2\pi r_0}{\lambda} \tag{2.53}$$

The solution to the scattering problem is one where the total field ($E_{tot} = E_{inc} + E_{scat}$) at the surface of the sphere satisfies

$$E_{\|} = Z \left(\hat{\rho} \times H_{tot} \right) \tag{2.54}$$

where $E_{\|} = E_{tot} - \hat{\rho} \cdot E_{tot}$ is the component of the electric field tangent to the sphere.

The scattered electric field can be solved as

$$E_{scat} = E_0 \sum_n \sum_n i^{n+1} \sqrt{\pi(2n+1)} \left(-b_n M_{n1}^{(3)} - a_n N_{n1}^{(3)} - b_n M_{n-1}^{(3)} + a_n N_{n-1}^{(3)} \right) \tag{2.55}$$

where

$$a_n = \frac{i\mathbf{n}\Psi_n{\prime}(\chi) - \Psi(\chi)}{in\xi_n{\prime}(\chi) - \xi_n(\chi)} \tag{2.56}$$

$$b_n = \frac{i\Psi_n\prime(\chi) - \mathbf{n}\Psi(\chi)}{i\xi_n\prime(\chi) - \mathbf{n}\xi_n(\chi)} \tag{2.57}$$

where $\Psi_n(x)$ and $\xi_n(x)$ are the Riccati-Bessel functions $\Psi_n(x) = xj_n(x)$ and $\xi_n(x) = xh_n^{(1)}(x)$. The coefficients a_n and b_n are formed so that one may be directly used in Borhen's convention [33] as well.

2.5.3.1 Comparison with Dielectric Theory

Because the surface impedance of a material can be directly related to its index of refraction by Equation 2.18, the surface impedance model and a more accurate dielectric model can be directly compared. For this study, the scattering efficiencies will be considered as the properties of interest. Scattering problems of this type have three principal inputs: the real part of the index of refraction, the imaginary part, and the size parameter of the particle (the product of the wavenumber of the incident radiation and the particle radius). In order to present the effects of the entire input space, two different sets of data are presented. First, one can consider a particle of a given size parameter with a range of indices of refraction. Second, the index of a particle can be held fixed with varying size parameters.

Figure 2.1 shows the extinction efficiencies for this set of particles all of size parameter $\chi = 15$ and various indices of refraction, using both the dielectric and impedance models. Figure 2.2 shows the relative error between the dielectric model and the surface impedance model for the extinction efficiency as well as the absorption, scattering, and isotropic scattering efficiencies. There are several features to note in these contours. The most striking is the horizontal band along the real axis, i.e. the region of small imaginary index. Here, the relative error between the two models rises dramatically above 10%. This is consistent with the hypothesis that the error should be largest when the skin depth is largest. Equation 2.18 shows that the skin depth is inversely proportional to the imaginary part of the index of refraction. Thus, the real axis is the region of highest error. Physically this region represents the class of particles which are not good conductors; there is no means to set up the surface currents which are the foundation of a surface impedance model.

Qualitatively, one will also note in Figure 2.2 that the errors in the scattering efficiency are larger than those in the absorption efficiency. Extinction efficiency, being the sum of the scattering and absorption efficiencies, has an average error between them. The surface impedance model scatters more than the dielectric would predict. However, one may also note that the isotropic scattering efficiencies have much lower error compared to the total scattering. The difference is the forward component of the scattering. All particles of this size parameter show scattering which is very forward peaked. Much of the scattered energy only deflects slightly from the incident path. The surface impedance model predicts that more energy is slightly deflected than the dielectric model predicts. However, any interaction, however slight, is measured in the scattering efficiency. For engineering applications, this difference is secondary to the isotropic scattering, where the models are more similar.

As a complement to Figure 2.2, Figure 2.3 shows the various cross sections of particles with constant index $(3 + 2.5i)$ but changing size parameter. Here, one can see the expected trend, where the two models converge as the particle size increases. The models diverge in the limit of small size parameters because the surface impedance model assumes a constant depth of current, even if the radius of the particle is less than that limit. The optical cross sections remain finite as the geometric cross section tends to zero, driving the relative error to infinity.

To conclude this section, one should note that there is almost no practical reason to calculate the scattering properties of a sphere with a surface impedance model. The calculation time is almost identical to the dielectric model but is less accurate. However, this analysis is a necessary foundation before developing surface impedance models of non-spherical models, where a dielectric model may not be computationally accessible.

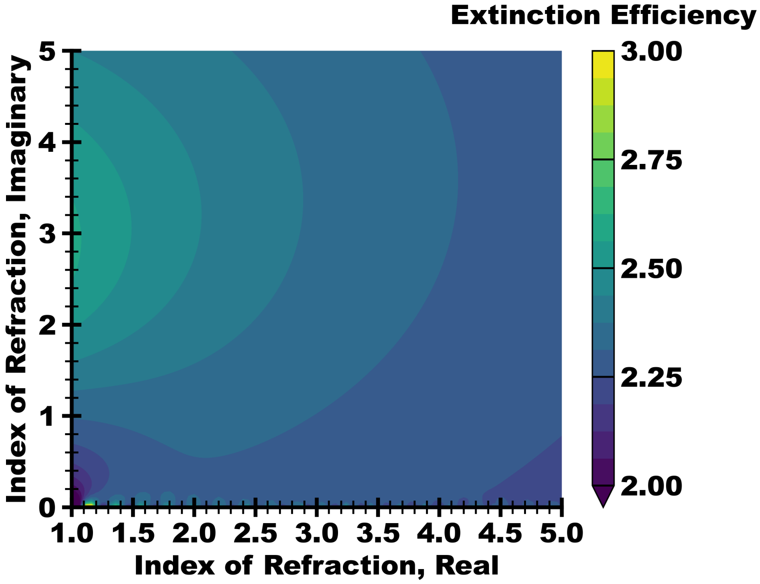

(a) Dielectric Model

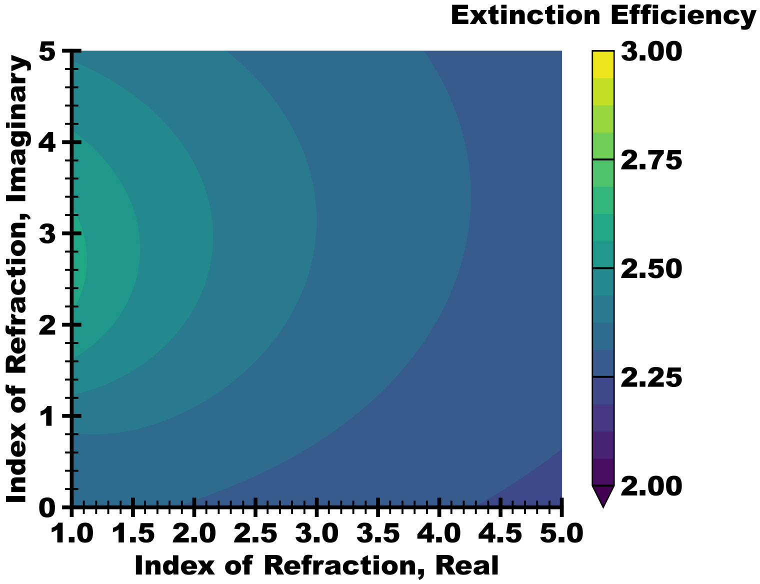

(b) Surface Impedance Model

Figure 2.1: Extinction efficiencies of particles of size parameter 15 with various indices of refraction. The surface impedance and dielectric models are used. The relative errors can be found in Figure 2.2a.

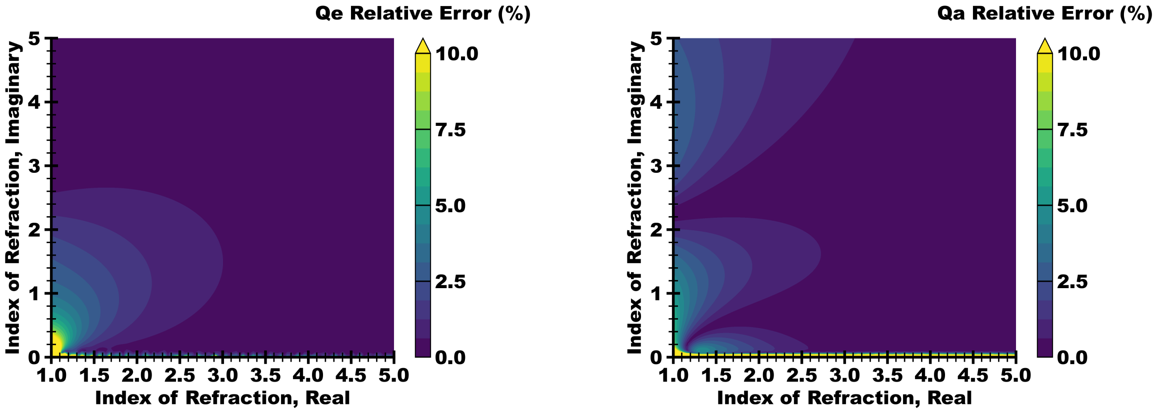

(a) Relative Error in Extinction Efficiency (b) Relative Error in Absorption Efficiency

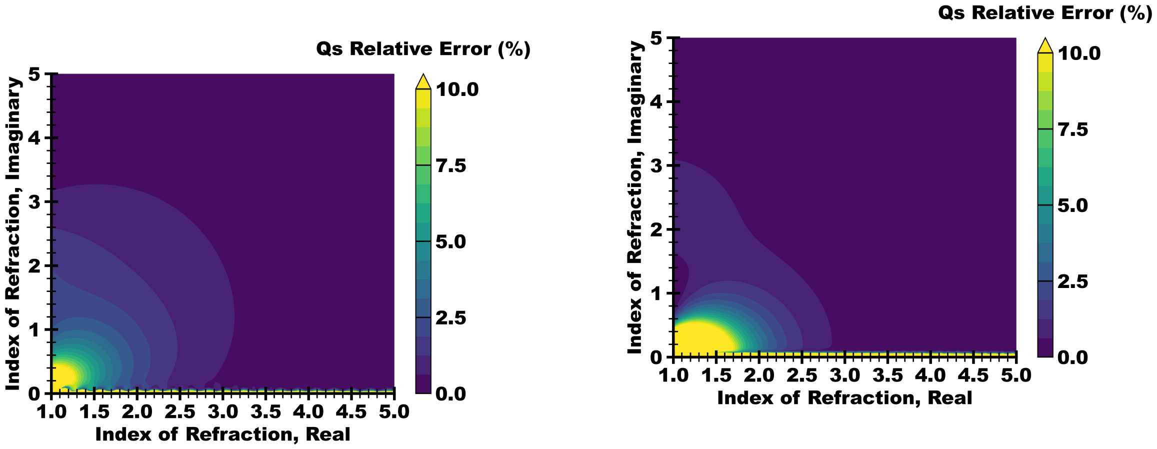

(c) Relative Error in Scattering Efficiency

(d) Relative Error in Isotropic Scattering Efficiency

Figure 2.2: Relative errors between the dielectric and surface impedance models for a class of particles of size parameter 15.

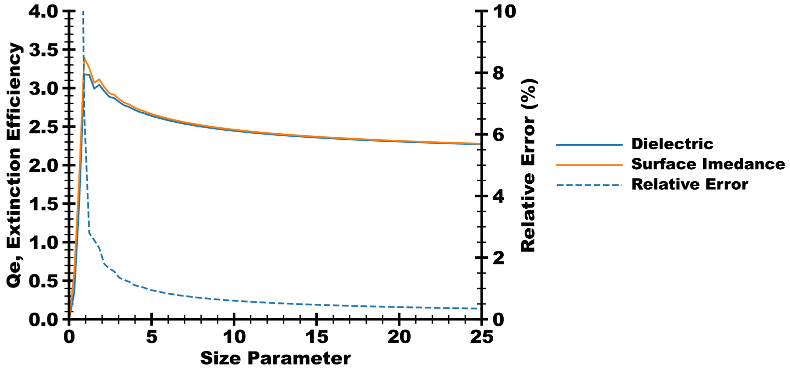

(a) Extinction Efficiency

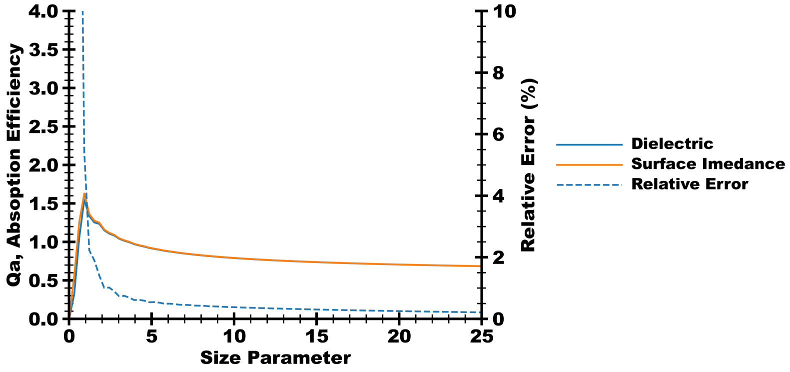

(b) Absorption Efficiency

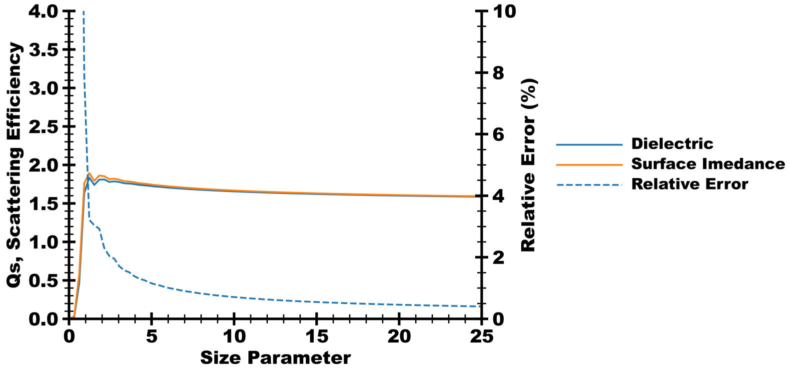

(c) Scattering Efficiency

Figure 2.3: Relative error between Mie and surface impedance scattering calculations for optical efficiencies. The index of refraction used is $3 + 2.5i$. The ratio of skin depth to the radius of the particle is also included

2.6 Scattering of a Non-Spherical Particle

In the previous sections, spherical particles were analyzed from the perspective of a scattered incident plane wave. The symmetry of the problem and linearity of the wave equation permits this solution to be used to account for multiple beams at any angle. The solution was reduced to harmonics of only $m = 1$. However, for asymmetric particles, one must account for the orientation of the particle with respect to the beam, greatly increasing the scope of the problem. A more systematic approach using modern spherical harmonic notation as well as matrix methods is necessary.

2.6.1 The T Matrix

In Section 2.4.2 an arbitrary field is expanded as a sum of spherical harmonics. The coefficients of these harmonics were denoted a_{nm} and b_{nm} where n is a positive integer and m is an integer such that $|m| \leq n$. These coefficients represent the field structure. From a quantum mechanical perspective they are exactly the angular momentum representation. In a scattering problem, one is interested in determining the scattered field with respect to the incident field. However, the independent field can take on an arbitrary representation in harmonic coefficients. Furthermore, the scattered coefficients can be linearly related to the incident coefficients via some matrix denoted T often called the transition matrix or just the T-matrix. The T matrix relates the scattered field coefficients P_{nm} and Q_{nm} to the incident field expanded as $a_{n^1m^1}$ and $b_{n^1m^1}$.

$$\begin{bmatrix} P_{nm} \\ \\ Q_{nm} \end{bmatrix} = Tnmn^1m^1 \begin{bmatrix} a_{n^1m^1} \\ \\ b_{n^1m^1} \end{bmatrix} \tag{2.58}$$

The T-matrix fully characterizes the scattering behavior of a particle at a particular frequency independent of the incident field. The scattering properties of a particle at various orientations can determined by expanding multiple field configurations representing incoming waves of different incident directions, multiplying these fields by the T-matrix, and examining the results.

The T-matrix has many other useful properties for determining the scattering of axisymmetric particles and rotationally averaged particles. If the particle is axisymmetric, then the incident harmonics only interact with harmonics of the same azimuthal harmonic index. This means that the T-matrix is reduced to a set of $2n_{tot} - 1$ matrices of size n_{tot} where n_{tot} is the maximum harmonic under consideration.

Oftentimes the properties of a suspension of non-spherical particles in random orientation are desired. Mishchenko has shown that one readily calculates the scattering properties of such a particle as

$$Q_e = \frac{-1}{\chi^2} \Re \left(T^{11}_{mnmn} + T^{22}_{mnmn} \right) \tag{2.59}$$

The T matrix itself is a representation of the properties of a particle. In itself it is not a means of calculating those properties. There are many technique to calculate the T-matrix. For optical scattering the most popular is the extended boundary technique.

2.6.2 Extended Boundary Technique

The calculation of the photon scattering properties of a particle is critical for high fidelity calculations of radiation transport. For small particles, several methods are available to perform this calculation, including analytical methods for dielectric spheres (the Mie solution). The extended boundary technique developed by Waterman [54] was shown to successfully predict the optical properties of many irregular dielectric particles. Waterman and others further developed the extended boundary method to perform calculations for dielectric particles.

The extended boundary method models the particle as a sheet of currents. If the particle is a sheet of currents (with no internal material), these currents would radiate, both creating the scattered field and negating the internal field. From an outside viewer this situation is identical to a real dielectric scatterer. To solve the equations, these currents also radiate into the particle as the internal field. Notice that in vacuum the currents radiate the negative of the incident field, but in the particle medium they radiate the internal field. Furthermore, the currents can be calculated by taking the curl of the internal field at the surface. This equation allows for all the fields to be solved in the system.

2.6.3 Surface Impedance Formulation

The extended boundary technique is a popular technique to determine the scattering properties of non-spherical particles. The technique has been used for perfectly conducting spheres and dielectric materials. It has been shown [55, 56] that the technique is unstable for

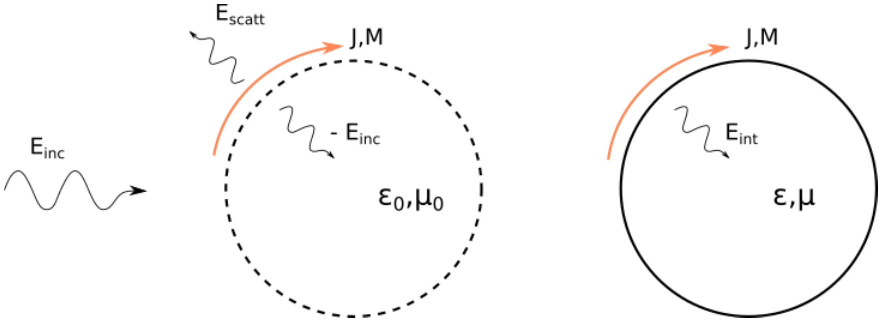

Figure 2.4: Schematic of the dielectric extended boundary method. The particle is modeled as a surface of currents (both magnetic and electric) which, in vacuum, generate the scattered field and negate the incident field inside the surface. Those same currents generate the internal field in the particle (the fields are different due to the different electrical properties of the particle).

large, absorbing particles. Although it has been improved with the use of higher numerical precision, there appears to always be a moment of divergence where the particle is simply too large or absorbing for the dielectric method to produce accurate results.

Since calculations tend to diverge as the particles become larger and more absorbing, the ranges of size and absorption properties of the particle are limited by the numerical accuracy of the computer. The use of extended precision has permitted the calculation to be effective for large particles [57], however, convergence is still difficult to attain for highly aspherical particles.

Although very large particles may be analyzed using geometric optics, there remains a class of particles which are sufficiently small to require a wave based analysis, but are yet too large to be treated by the current formulations of the extended boundary technique. While these difficulties do not prevent the study of radiative transfer though aerosolized clouds or droplets, the study of radiative transfer through metallic clouds [58] requires an accurate prediction of large, absorbing, non-spherical particle scattering properties that is currently missing. Without such a model, large radiative transport simulations which are sensitive to the optical model will remain inaccurate.

To achieve a general model, the dielectric material model of the particle is dropped in favor of a surface impedance. The surface impedance assumes that a thin layer of currents exists at the surface of a conducting material. The original formulation of the extended boundary technique was developed for a perfect conductor [59], but not one with a lossy impedance. This is only valid when the skin depth is small relative to the radius of curvature of the material [49]. The exact error introduced for the scattering of small particles is unknown.

This section will address scattering calculations using a surface impedance model in two parts. First, a comparison of the dielectric versus the surface impedance model will be discussed. This will define an approximate parameter space over which this model is valid. Second, the surface impedance model will be applied to the extended boundary technique to produce a T-matrix for these particles. Using this technique, the optical properties of large absorbing spheroids will be presented.

2.6.3.1 Derivation of Method

Following the physical arguments of Barber et al [60], consider a particle to be modeled as a shell of surface currents as shown in Figure 2.5. These currents are related to the external fields as

$$\begin{aligned} \vec{j} &= \hat{n} \times \vec{H}_{ext} \\ \vec{m} &= \hat{n} \times \vec{E}_{ext} \end{aligned} \tag{2.60}$$

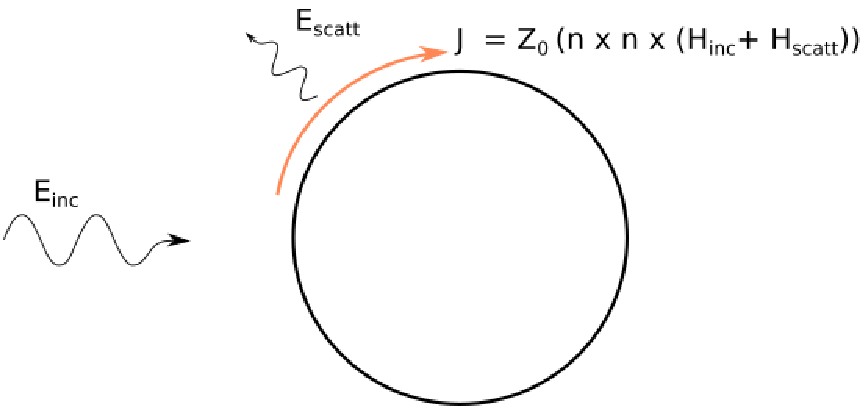

Figure 2.5: Schematic of the surface impedance extended boundary method. The particle is modeled as a surface of currents (both magnetic and electric) which, in vacuum, generate the scattered field. The internal field is modeled though the surface imedance boundary condition.

where $\vec{E}_{ext}$ is the external field. These currents are assumed to generate the scattered field away from the particle, given as

$$E_s(\vec{\rho}) = \nabla \times \int_s (\hat{n} \times E_{ext}(\rho_s)) \cdot G(\rho_s, \rho) ds + \frac{i}{\omega \epsilon} \nabla \times \nabla \times \int_s (\hat{n} \times H_{ext}(\rho_s)) \cdot G(\rho_s, \rho) ds \quad (2.61)$$

where ρ_s denotes the position vector on the surface of the particle and G is the Green's function (Equation 2.28). The surface impedance condition is then introduced.

$$E_{\parallel} = Z(\hat{n} \times H) \quad (2.62)$$

where Z is the surface impedance, $E_{\parallel}$ is the tangential component of the electric field to the surface, and $\hat{n}$ is the unit normal. Note that

$$\hat{n} \times E = \hat{n} \times E_{\perp} + \hat{n} \times E_{\parallel} = 0 + Z\left(\hat{n} \times \hat{n} \times H\right) \quad (2.63)$$

enables one to substitute Equation 2.62 into Equation 2.61.

$$E_s(\vec{\rho}) = Z\nabla \times \int_s (\hat{n} \times \hat{n} \times H_{ext}(\rho_s)) \cdot G(\rho_s, \rho) ds + \frac{i}{\omega\epsilon} \nabla \times \nabla \times \int_s (\hat{n} \times H_{ext}(\rho_s)) \cdot G(\rho_s, \rho) ds \tag{2.64}$$

Using the fields

$$E_s = \sum_{n=0}^{\infty} \sum_{m=-n}^{n} P_{nm} M_{nm}^{(3)} + Q_{nm} N_{nm}^{(3)};\ H_s = \frac{-ik}{\omega\mu} \sum_{n=0}^{\infty} \sum_{m=-n}^{n} P_{nm} N_{nm}^{(3)} + Q_{nm} M_{nm}^{(3)} \tag{2.65}$$

$$E_{inc} = \sum_{n=0}^{\infty} \sum_{m=-n}^{n} a_{nm} M_{nm}^{(1)} + b_{nm} N_{nm}^{(1)};\ H_{inc} = \frac{-ik}{\omega\mu} \sum_{n=0}^{\infty} \sum_{m=-n}^{n} a_{nm} N_{nm}^{(1)} + b_{nm} M_{nm}^{(1)} \tag{2.66}$$

$$E_{ext} = E_s + E_{inc};\ H_{ext} = H_s + H_{inc} \tag{2.67}$$

as well as the Green's function (Equation 2.28), one arrives at

$$\begin{aligned}
0 = &- P_{n^1m^1} M_{n^1m^1}^{(3)} - Q_{n^1m^1} N_{n^1m^1}^{(3)} \\
&+ \frac{Zk^2}{\omega\mu} \nabla \times \int_s \left(\hat{n} \times \hat{n} \times (P_{nm} N_{nm}^{(3)} + Q_{nm} M_{nm}^{(3)} + a_{nm} N_{nm}^{(1)} + b_{nm} M_{nm}^{(1)})(\rho_s)\right) \\
&\cdot \left(M_{n^1m^1}^{(3)}(\vec{\rho}) M_{n^1m^1}^{(1)}(\vec{\rho}_s) + N_{n^1m^1}^{(3)}(\vec{\rho}) N_{n^1m^1}^{(1)}(\vec{\rho}_s)\right) ds \\
&+ \frac{ik^2}{\omega^2\mu\epsilon} \nabla \times \nabla \times \int_s \left(\hat{n} \times (P_{nm} N_{nm}^{(3)} + Q_{nm} M_{nm}^{(3)} + a_{nm} N_{nm}^{(1)} + b_{nm} M_{nm}^{(1)})(\rho_s)\right) \\
&\cdot \left(M_{n^1m^1}^{(3)}(\vec{\rho}) M_{n^1m^1}^{(1)}(\vec{\rho}_s) + N_{n^1m^1}^{(3)}(\vec{\rho}) N_{n^1m^1}^{(1)}(\vec{\rho}_s)\right) ds
\end{aligned} \tag{2.68}$$

$$
\begin{aligned}
0 = & -P_{n^1m^1}M^{(3)}_{n^1m^1} - Q_{n^1m^1}N^{(3)}_{n^1m^1} \\
& + \frac{Zk^2}{\omega\mu}\nabla \times M^{(3)}_{n^1m^1} \\
& \cdot \int_s \big(\hat{n} \times \hat{n} \times (P_{nm}N^{(3)}_{nm} + Q_{nm}M^{(3)}_{nm} + a_{nm}N^{(1)}_{nm} + b_{nm}M^{(1)}_{nm)}(\rho_s)\big) \cdot M^{(1)}_{n^1m^1}ds \\
& + \frac{Zk^2}{\omega\mu}\nabla \times N^{(3)}_{n^1m^1} \\
& \cdot \int_s \big(\hat{n} \times \hat{n} \times (P_{nm}N^{(3)}_{nm} + Q_{nm}M^{(3)}_{nm} + a_{nm}N^{(1)}_{nm} + b_{nm}M^{(1)}_{nm)}(\rho_s)\big) \cdot N^{(1)}_{n^1m^1}ds \\
& + \frac{ik^2}{\omega^2\mu\epsilon}\nabla \times \nabla \times M^{(3)}_{n^1m^1} \\
& \cdot \int_s \big(\hat{n} \times (P_{nm}N^{(3)}_{nm} + Q_{nm}M^{(3)}_{nm} + a_{nm}N^{(1)}_{nm} + b_{nm}M^{(1)}_{nm)}(\rho_s)\big) \cdot M^{(1)}_{n^1m^1}ds \\
& + \frac{ik^2}{\omega^2\mu\epsilon}\nabla \times \nabla \times N^{(3)}_{n^1m^1} \\
& \cdot \int_s \big(\hat{n} \times (P_{nm}N^{(3)}_{nm} + Q_{nm}M^{(3)}_{nm} + a_{nm}N^{(1)}_{nm} + b_{nm}M^{(1)}_{nm)}(\rho_s)\big) \cdot N^{(1)}_{n^1m^1}ds
\end{aligned} \tag{2.69}
$$

$$
\begin{aligned}
0 = & -\delta_{nn^1}\delta_{mm^1}P_{nm}M^{(3)}_{nm} - \delta_{nn^1}\delta_{mm^1}Q_{nm}N^{(3)}_{nm} \\
& + \frac{Zk^2}{Z_0}N^{(3)}_{n^1m^1}\int_s \big(\hat{n} \times \hat{n} \times (P_{nm}N^{(3)}_{nm} + Q_{nm}M^{(3)}_{nm} + a_{nm}N^{(1)}_{nm} + b_{nm}M^{(1)}_{nm)}(\rho_s)\big) \cdot M^{(1)}_{n^1m^1}ds \\
& + \frac{Zk^2}{Z_0}M^{(3)}_{n^1m^1}\int_s \big(\hat{n} \times \hat{n} \times (P_{nm}N^{(3)}_{nm} + Q_{nm}M^{(3)}_{nm} + a_{nm}N^{(1)}_{nm} + b_{nm}M^{(1)}_{nm)}(\rho_s)\big) \cdot N^{(1)}_{n^1m^1}ds \\
& + ik^2M^{(3)}_{n^1m^1}\int_s \big(\hat{n} \times (P_{nm}N^{(3)}_{nm} + Q_{nm}M^{(3)}_{nm} + a_{nm}N^{(1)}_{nm} + b_{nm}M^{(1)}_{nm)}(\rho_s)\big) \cdot M^{(1)}_{n^1m^1}ds \\
& + ik^2N^{(3)}_{n^1m^1}\int_s \big(\hat{n} \times (P_{nm}N^{(3)}_{nm} + Q_{nm}M^{(3)}_{nm} + a_{nm}N^{(1)}_{nm} + b_{nm}M^{(1)}_{nm)}(\rho_s)\big) \cdot N^{(1)}_{n^1m^1}ds
\end{aligned} \tag{2.70}
$$

where δ_{nm} is the Kronecker delta function. Defining the quantities

$$C^{(i)(j)}_{nmn^1m^1}{}^{uv} = k^2 \begin{bmatrix} \int_s (M^{(i)}_{nm} \times M^{(j)}_{n^1m^1}) \cdot \hat{n} ds & \int_s (M^{(i)}_{nm} \times N^{(j)}_{n^1m^1}) \cdot \hat{n} ds \\ \int_s (N^{(i)}_{nm} \times M^{(j)}_{n^1m^1}) \cdot \hat{n} ds & \int_s (N^{(i)}_{nm} \times N^{(j)}_{n^1m^1}) \cdot \hat{n} ds \end{bmatrix} \tag{2.71}$$

$$D^{(i)(j)}_{nmn^1m^1}{}^{uv} = k^2 \begin{bmatrix} \int_s (\hat{n} \times M^{(i)}_{nm}) \cdot (\hat{n} \times M^{(j)}_{n^1m^1}) ds & \int_s (\hat{n} \times M^{(i)}_{nm}) \cdot (\hat{n} \times N^{(j)}_{n^1m^1}) ds \\ \int_s (\hat{n} \times N^{(i)}_{nm}) \cdot (\hat{n} \times M^{(j)}_{n^1m^1}) ds & \int_s (\hat{n} \times N^{(i)}_{nm}) \cdot (\hat{n} \times N^{(j)}_{n^1m^1}) ds \end{bmatrix} \tag{2.72}$$

letting u and v be the matrix indices and knowing that M_{nm} and N_{nm} are orthogonal, one can decompose the single Equation 2.70 into the following pair

$$\begin{aligned} 0 = -P_{n^1m^1} &+ \frac{Z}{Z_0}(P_{nm} D^{(3)(1)}_{nmn^1m^1}{}^{22} + Q_{nm} D^{(3)(1)}_{nmn^1m^1}{}^{12} + a_{nm} D^{(1)(1)}_{nmn^1m^1}{}^{22} + b_{nm} D^{(1)(1)}_{nmn^1m^1}{}^{12}) \\ &+ i(P_{nm} C^{(3)(1)}_{nmn^1m^1}{}^{21} + Q_{nm} C^{(3)(1)}_{nmn^1m^1}{}^{11} + a_{nm} C^{(1)(1)}_{nmn^1m^1}{}^{21} + b_{nm} C^{(1)(1)}_{nmn^1m^1}{}^{11}) \\ 0 = -Q_{n^1m^1} &+ \frac{Z}{Z_0}(P_{nm} D^{(3)(1)}_{nmn^1m^1}{}^{21} + Q_{nm} D^{(3)(1)}_{nmn^1m^1}{}^{11} + a_{nm} D^{(1)(1)}_{nmn^1m^1}{}^{21} + b_{nm} D^{(1)(1)}_{nmn^1m^1}{}^{11}) \\ &+ i(P_{nm} C^{(3)(1)}_{nmn^1m^1}{}^{22} + Q_{nm} C^{(3)(1)}_{nmn^1m^1}{}^{12} + a_{nm} C^{(1)(1)}_{nmn^1m^1}{}^{22} + b_{nm} C^{(1)(1)}_{nmn^1m^1}{}^{12}) \end{aligned} \tag{2.73}$$

in block matrix form

$$
\begin{aligned}
0 = {} & \\
& \begin{bmatrix} -\delta_{nn^1}\delta_{mm^1} + \frac{Z}{Z_0} D_{nmn^1m^1}^{(3)(1)\quad 22} + iC_{nmn^1m^1}^{(3)(1)\quad 22} & \frac{Z}{Z_0} D_{nmn^1m^1}^{(3)(1)\quad 12} + iC_{nmn^1m^1}^{(3)(1)\quad 12} \\ \frac{Z}{Z_0} D_{nmn^1m^1}^{(3)(1)\quad 21} + iC_{nmn^1m^1}^{(3)(1)\quad 21} & -\delta_{nn^1}\delta_{mm^1} + \frac{Z}{Z_0} D_{nmn^1m^1}^{(3)(1)\quad 11} + iC_{nmn^1m^1}^{(3)(1)\quad 11} \end{bmatrix} \\
& \begin{bmatrix} P_{nm} \\ \\ Q_{nm} \end{bmatrix} \\
& + \\
& \begin{bmatrix} \frac{Z}{Z_0} D_{nmn^1m^1}^{(3)(1)\quad 12} + iC_{nmn^1m^1}^{(3)(1)\quad 12} & \frac{Z}{Z_0} D_{nmn^1m^1}^{(3)(1)\quad 22} + iC_{nmn^1m^1}^{(3)(1)\quad 22} \\ \frac{Z}{Z_0} D_{nmn^1m^1}^{(3)(1)\quad 11} + iC_{nmn^1m^1}^{(3)(1)\quad 11} & - + \frac{Z}{Z_0} D_{nmn^1m^1}^{(3)(1)\quad 21} + iC_{nmn^1m^1}^{(3)(1)\quad 21} \end{bmatrix} \\
& \begin{bmatrix} a_{nm} \\ \\ b_{nm} \end{bmatrix}
\end{aligned}
\tag{2.74}
$$

which can be notated as

$$
0 = R_{nmn^1m^1} \begin{bmatrix} P_{nm} \\ \\ Q_{nm} \end{bmatrix} + Q_{nmn^1m^1} \begin{bmatrix} a_{nm} \\ \\ b_{nm} \end{bmatrix} \tag{2.75}
$$

such that the T-matrix is given as

$$
\begin{bmatrix} P_{nm} \\ \\ Q_{nm} \end{bmatrix} = Tnmn^1m^1 \begin{bmatrix} a_{n^1m^1} \\ \\ b_{n^1m^1} \end{bmatrix} = -Q_{nmn^1m^1}^{-1} R_{n^1m^1n^2m^2} \begin{bmatrix} a_{n^2m^2} \\ \\ b_{n^2m^2} \end{bmatrix} \tag{2.76}
$$

2.6.3.2 Azimuthally Symmetric Particles

For azimuthally symmetric particles, the integrals along the surface yield zero for all but the case when $m^1 = -m$. This permits the simplification

$$T_{(\phi_{sym}) \quad nn^1m} = T_{nmn^1m^1}\delta_{m-m^1} \tag{2.77}$$

This is the form usually calculated for droplets and particles since the computation is reduced from inverting a single $n * m$-by-$n * m$ matrix to inverting m matrices of size n-by-n.

2.6.4 Results for Spheroidal Particles

Many particles can be modeled as a perfect sphere. For very distorted particles, however, a spheroid is the next highest order approximation. Having data on spheroid behavior can help determine if high-order modeling is necessary to capture the scattering properties of a general particle.

There are two characteristic dimensions of a spheroidal particle, the axial radius and the azimuthal radius. The ratio between the two is called the axis ratio, η. An axis ratio greater than one is an oblate spheroid and an axis ratio less than one is a prolate spheroid. An extended boundary surface impedance calculation can be performed in the natural frame of the spheroid so that the azimuthal simplification can be used. By adjusting the incident harmonics (Equation 2.66) to represent an incoming plane wave from an arbitrary zenith angle [61], a spheroid in an arbitrary orientation can be modeled.

The surface impedance method permits the calculation of the T-matrix for a spheroid that cannot be analyzed with a general dielectric method. There is no number of harmonics that will produce a converged solution. Figure 2.8 plots the convergence profile for the spheroid with an elongation ratio of 2.0 and an index of refraction $3 - 2.5i$. Convergence is determined by calculating a submatrix of the T-matrix with all $m = 0$ for $n < N$. The quantity Q is then calculated as

$$Q_N = \frac{2}{\chi^2} \sum_{n}^{N} (2n+1) \left(|T^{11}_{(\phi_{sym})nn0}| + |T^{22}_{(\phi_{sym})nn0}| \right) \tag{2.78}$$

where T^{11} and T^{22} are the upper left and lower right block elements of the T-matrix (see Equation 2.76). This quantity is similar to the scattering efficiency but does not include all terms. Convergence is considered to have occurred when the relative change of Q with the additional harmonic is less than 0.001%. This condition is not met using a dielectric extended boundary method. This is consistent with a large body of research on the extended boundary method [36, 56, 62]. It has been shown that increasing the numerical precision can induce convergence. However, this case fails to converge with up to 50 decimal places of precision (166 bits). The surface impedance method provides a general method (as opposed to, for example, the spheroid-specific method of Somerville [63]) of modeling the optical properties of these particles using the same framework as a standard extended boundary method. Furthermore, the surface impedance method has a significantly lower runtime.

This method enables the examination of a set of spheroids of given surface impedance and volume. All axis ratios in the range of 0.5 to 2.0 are considered as well as incident beam angles of 0 to $\frac{\pi}{2}$. By symmetry, the cross sections at all other beam angles can be determined. Figure 2.6 illustrates how the contours of optical efficiency are plotted in the figures which follow. The incident beam is always considered to be moving along the x axis.

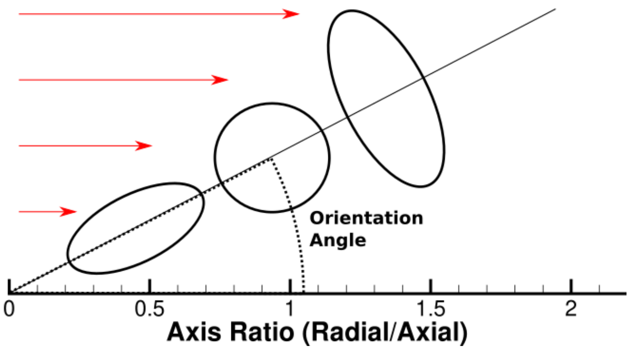

Figure 2.6: Schematic of physical interpretation of the optical efficiency contours as plotted in later figures. The incident beam is always considered to be moving along the X axis. The angle from the X axis is the orientation of the particle and the distance from the origin is the axis ratio.

The angle from the x axis is the orientation of the particle and the distance from the origin is the axis ratio.

Figure 2.7 presents the optical efficiencies for a particle of size parameter 30 and index of refraction $3 + 2.5i$. As expected, in all plots there exists a ring of constant efficiencies at an axis ratio of 1. This describes a sphere with optical properties independent of orientation. As the axis ratios deviate from 1, the majority of the deviation from the spherical case is present in the absorption efficiency, which can deviate by as much as 40% from the spherical condition. The scattering efficiency, on the other hand, only varies by approximately 20%.

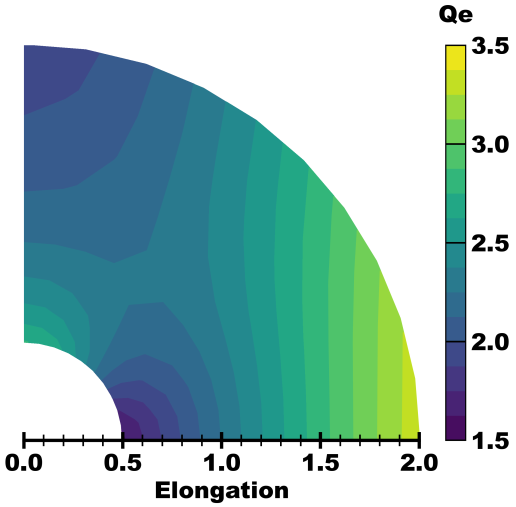

(a) Extinction Efficiency

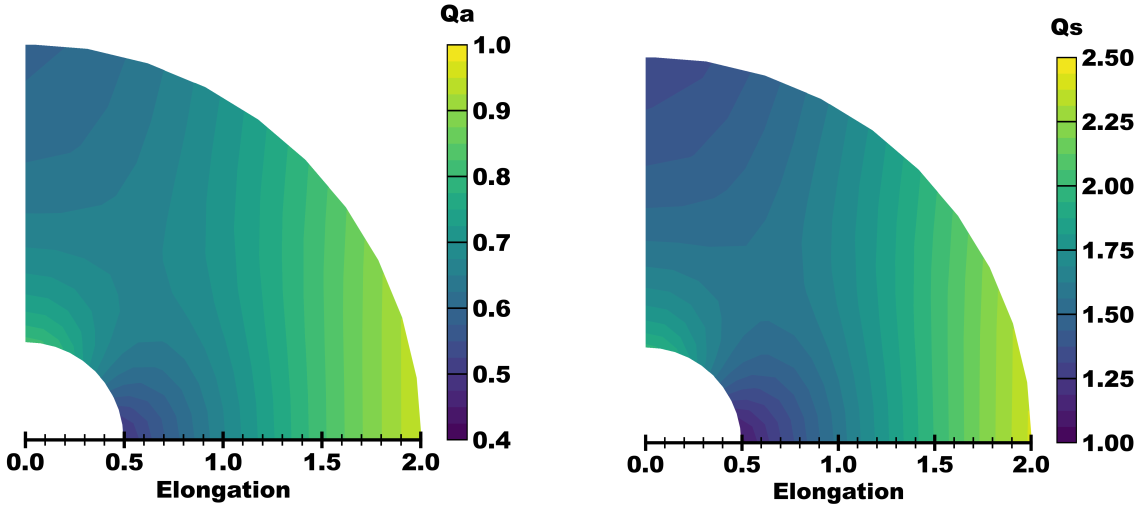

(b) Absorption Efficiency

(c) Scattering Efficiency

Figure 2.7: Optical efficiencies of spheroidal particles with varying elongations, all with effective size parameter 30 and index of refraction $3 + 2.5i$.

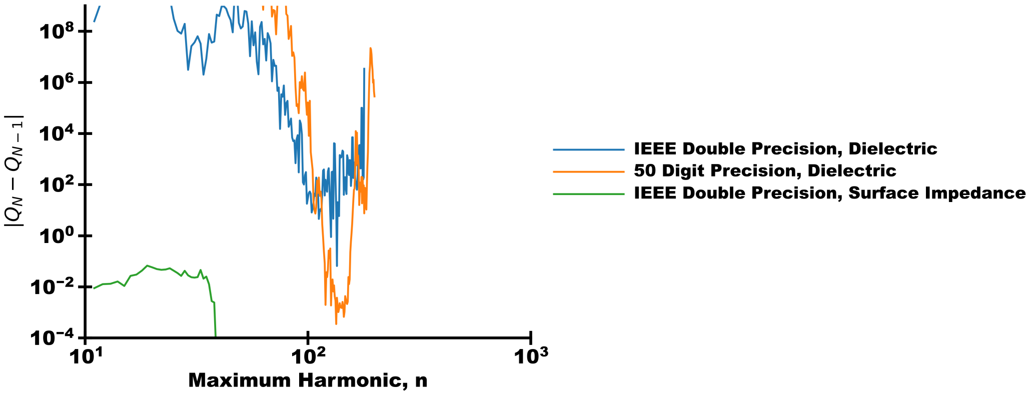

Figure 2.8: Extended boundary method convergence with increasing maximum harmonic. All curves pertain to a spheroid of index of refraction $3 - 2.5i$ with elongation ratio of 2.0. This represents a particle on the outer extremity of Figure 2.7. Q represents an approximate scattering effiecy (Equation 2.78). The dieletric method fails to converge, even at increased computational precision.

2.7 Conclusions

This chapter has outlined the essentials of optical scattering theory. This can include the governing equations and material property models. This was followed with a discussion of spherical harmonics which are usually employed for analyzing the scattering of a sphere. The quantities of interest in scattering, namely the scattering efficiencies and the scattering function were outlined with respect to this mathematical framework.

Scattering theory was also introduced for other particles that could be solved analytically. Yang's method for layed spheres was extended to include various particle magnetic permeabilities. Furthermore, the scattering of a sphere of given surface impedance was examined and compared against dielectric theory.

Attention was then turned to nonspherical particles. In general, these particles can not be examined analytically and must be solved numerically. The numerical method empoyled was the extended boundary technique, which calculates the transition matrix, T, by integrating harmonics over the particle.

The calculations of a particle using the extended boundary method is generally unstable if the particle is large and absorbing. This leaves a class of particles that are large, but not large enough to be examined with geometric optics that cannot be analyzed. This gap can be bridged by reformulating the extended boundary technique with a surface impedance model.

The surface impedance is a model for a flat conductive boundary condition. The curved surface of a particle will always introduce some error into the calculations. By analyzing the solution of scattering of a sphere in both a dielectric and surface impedance solution, it was shown that errors in the cross section will remain under 5% provided that non-dimensional value $\frac{\Im(n)^{0.2}}{\chi}$ remained under 0.1.

This solution will enable researchers to understand the transition between wave optics and geometric optics, and between spherical and non-spherical absorbing particles. This is especially useful for large radiative transport simulations where both the runtime and results are sensitive to the optical model.

CHAPTER 3

Radiative Transfer Through Particle Clouds

3.1 Towards a Continuum Approximation

Chapter 2 introduced multiple methods for calculating the scattering of a single particle of various configurations. This analysis has been used to great effect in weather modeling and small particle control, a situation where a scattered signal is the quantity of interest. However, this chapter will focus on expanding and compounding the previous analysis in order to calculate the *heat transfer* through a particulate medium.

Radiative transfer processes focus on three physical phenomena: emission, absorption, and scattering. Particles may be hot enough to spontaneously emit photons in some direction. Photons may collide with a particle and photons may interact with a particle in a way that changes its momentum.

In chapter 2 the emission and absorption of photons were modeled as a change in the electric and magnetic field around the particle. Abstract quantities were defined such as the absorption and scattering cross-section (σ_a and σ_s respectively) however, these did not correspond to an actual "shadow" cast by the particle. The energy flow around a particle was not forced to resemble an elastic scattering process, for example.

This may suggest that the transfer of energy through a particle cloud must be approached from an electromagnetic perspective, which is directly solving for the electric and magnetic fields in all points in space. This has been accomplished [], however, these methods are limited in the number of particles that can be analyzed.

For larger clouds, one must take the far-field approximation. That is that the particle is small relative to the length scales of the problem of interest and the flow of energy around the particle is purely radial. Neglecting polarization permits one to fully define a particle with three parameters, a scattering cross-section, an absorption cross-section, and a scattering phase function $P(\Omega_1, \Omega_2)$. The scattering phase function is left as a function of two solid angles to account for particle orientation and asymmetry. For the unpolarized scattering of a sphere, P reduces to a function of the angle between scattering and incident directions.

Because the particles are assumed to be small, the effect of the cross-sections is limited to as small a radius about the particle center as possible. The cross-sections are taken as physical areas which interact with a flux of photons.

A large number of particles, even if they are represented by their far-field signatures, are still almost impossible to treat analytically, and only recently have computational resources made numerical analysis possible (see Chapter 4). The last approximation is to consider the photons to be a homogenous beam with a variation that is very slow compared to the particle size. By non-localizing the beam with respect to the particle, one effectively non-localizes the particle.

Mathematically, this is to consider that the energy distribution, which will be represented as $I(\vec{x}, \hat{\Omega})$, has spatial derivatives that change on a length scale much larger than the particle size

$$\left(\frac{\nabla I(\vec{x},\hat{\Omega})}{I(\vec{x},\hat{\Omega})}\right)^{-1} \gg \sqrt{\sigma_g} \tag{3.1}$$

where σ_g is the particle geometric cross-section. This suggests that at any $\vec{x}$ the energy beam can interact with the local distribution of particles and it interacts with that differential cloud with a certain probability.

One can imagine that such a continuous cloud element exists. Here the discrete particle approach is forgotten for a purely continuous one. In this approach, one constructs a cross-section density, also called opacity, with units of inverse length. This will be denoted β. One can hypothesize that the interaction with the beam is dependent on the length that the beam travels as it passes through the cloud. Note, as was mentioned in Chapter 2, this interaction must change a particular photon's momentum. This is tantamount to removing the energy from the initial beam. Mathematically, The loss of energy in the beam $I(\vec{x},\hat{\Omega})$ can be written as

$$I(\vec{x}+\Delta\hat{\Omega},\hat{\Omega}) - I_0(\vec{x},\hat{\Omega}) = -\beta \left\|\Delta\hat{\Omega}\right\| \bar{I}(\vec{x}+\Delta\hat{\Omega},\hat{\Omega}) \tag{3.2}$$

where I_0 is the initial intensity, $\bar{I}$ is the average intensity over the path, and Ω is a direction vector. One can take the limit of small $\Delta\Omega$ to arrive at the familiar result

$$\nabla I(\vec{x},\hat{\Omega}) \cdot \hat{\Omega} + \beta I(\vec{x},\hat{\Omega}) = 0 \tag{3.3}$$

This model currently models a pure beam loss – effective for a purely absorbing medium. One can introduce scattering as

$$\nabla I(\vec{x},\hat{\Omega})\cdot\hat{\Omega}+\beta_e I(\vec{x},\hat{\Omega})=\int_{4\pi}\beta_s P(\hat{\Omega},\Omega\prime)I(\vec{x},\hat{\Omega})d\Omega\prime+\epsilon(\vec{x}) \tag{3.4}$$

where β_e is identified as the extinction opacity, β_s is the absorption opacity, $\epsilon(\vec{x})$ represents some emission source. Equation 3.4 is referred to as the radiative transfer equation.

3.2 Homogenization Error

3.3 Introduction

The study of radiative transfer often involves the presence of a particulate that interacts with the flow of energy. Many challenges in the study of radiative transfer include modeling a cloud of particulates in a way to accurately determine transmission and absorption with as few calculations as possible.

Numerical simulations, for example, rarely can accommodate the memory and processing power necessary to explicitly model all particles present in a physical system. The standard treatment of this problem is to produce a mesh with average quantities of the cloud ascribed to each volume element. The simulation then interacts with the cloud element. In a Monte Carlo ray trace (MCRT) simulation, the element generates a statistical path distribution determining how far the ray will travel. For a discrete ordinates simulation, this directly enters into the energy loss of the sweep in that particular direction. How the model then converts a set of particles to a cloud element will be referred to as the homogenization model. The most common model is the Beer-Lambert-Bouger Law (see Section 3.4), which will be simply called the Beer-Lambert Law for the remainder of the dissertation.

This homogenization model can produce inaccuracies in a radiative transfer calculation [65–67]. The cloud model does not predict what the individual particles would transmit, scatter, and absorb. Many studies have been dedicated to understanding how an error is introduced by homogenizing a group of particles with a non-uniform density. As particles cluster together, the total absorption tends to decrease [31]. For computational speed, this clustering may be impossible to resolve by the domain discretization. One must add a model to modify the Beer-Lambert Law to account for the fact that the cloud does not have a uniform density across a finite volume. These models are analogous to subscale modeling in turbulence simulations [68].

This work will show that there are, in addition to the errors discussed above, errors in the Beer-Lambert Law which arise purely due to the particulate nature of the material. These errors manifest either when the length scale of the homogenized volume is on the same order as the size of the particle or when the particles are highly concentrated. This discrepancy has been observed before. For example, Frankel [69] claimed that there was no verifiable solution to the radiative transfer equations, based on the notion from computational fluid mechanics that as a mesh is refined, the solution should converge to a single solution. When a particle field is homogenized with the Beer-Lambert Law, the solution will diverge as the mesh is refined. This divergence is addressed throughout the following.

This study will be composed of four principal parts. First, a discussion of the Beer-Lambert Law will be presented. Secondly, a series of small simulations representing one computational cell of a larger simulation will be shown. These simulations will demonstrate two principle errors that occur in the Beer-Lambert Law. Next, a new model is presented to determine the radiative characteristic of the cloud. Lastly, these models will be used in calculations involving many particles and many computational cells, addressing the applicability of the Beer-Lambert Law and the benefits of the new model.

3.4 The Beer-Lambert Law

3.4.1 Derivation

Consider a volume, V, filled with particles. The real particles may have various diameters and cross-sectional areas. Let the sum of the particles' cross-sectional area be Σ. Divide the total area, Σ, into N idealized particles, each with an average area σ, such that $\Sigma = N \cdot \sigma$. Consider a beam of energy I_o incident on these particles. Divide the volume into N sub-volumes with interfaces perpendicular to I_o, and place one particle in each sub-volume. There are then N slabs such that the radiative energy travels through every slab. Allow each sub-volume to have a cross-sectional area A with respect to the beam. The expected change in I, the local beam intensity, as it traverses one sub-volume is

$$\frac{I}{I_0} = 1 - \frac{\sigma}{A} \tag{3.5}$$

The total transmission through all the sublayers is then

$$\frac{I}{I_0} = \prod_{i=0}^{N} \left(1 - \frac{\sigma}{A}\right) = \left(1 - \frac{\sigma}{A}\right)^N = \left(1 - \frac{\Sigma/A}{N}\right)^N \tag{3.6}$$

If one permits the number of particles to tend towards infinity

$$\frac{I}{I_0} = \lim_{N \to \infty} \left(1 - \frac{\Sigma/A}{N}\right)^N = e^{-\Sigma/A} \tag{3.7}$$

By idenifying Σ/A as τ, the optical depth, one recovers the Beer-Lambert Law

$$I_{Beer} = I_0 e^{-\tau} \tag{3.8}$$

Two assumptions were applied in this derivation. The particles were redistributed into N particles and N was taken to infinity. Secondly, the particles were assumed to reside in independent bins. This permits the position of the particle with respect to the beam to be independent of every other particle. These assumptions can be expressed most succinctly as

A.1 A set of particles can be considered infinite

A.2 The particles positions orthogonal with respect to a beam are independent.

3.4.2 Non-Infinitesimal Particles

The Beer-Lambert Law was originally derived to calculate the transmission of light through liquid mixtures. It is accurate for this application because the number of particles (i.e. atoms) can be taken as nearly infinite. However, there are many instances where the number of particles is finite. One can directly make predictions concerning groups of particles that do not meet Assumption *A.1* (but do meet *A.2*). The expected transmission for a set of N_0 particles of uniform size is

$$T = \frac{I}{I_0} = \left(1 - \frac{\tau}{N_0}\right)^{N_0} \tag{3.9}$$

based on Equation 3.6. The transmission error with respect to the Beer-Lambert Law is calulated as

$$\Delta\left(T\right) = \left\| e^{-\tau} - \left(1 - \frac{\tau}{N_0}\right)^{N_0} \right\| \tag{3.10}$$

This is plotted in Figure 3.1. The most striking feature of this plot is the rise in error with decreasing number of particles. However, it is also clear that the error is also highly dependent on the size of the individual particles. At low optical depths, as the particle size increases, the error increases. For multiple particles, there is an optical depth of maximum error. This is the point where the transmission through the cell is approximately equal to the error. As the optical depth continues to rise, the error is constrained to the maximum transmission. It should also be noted that the curves are truncated to the condition where the optical depth is equal to the number of particles. This is because at high optical depths, the particle is by definition larger in cross-section than the cell area. Equation 3.10 will calculate unphysical errors at this point.

3.4.3 Mesh Refinement

The expected error between the Beer-Lambert Law and a cloud of a finite number of particles is the primary source of error that exists as a mesh is refined. Consider a cube of

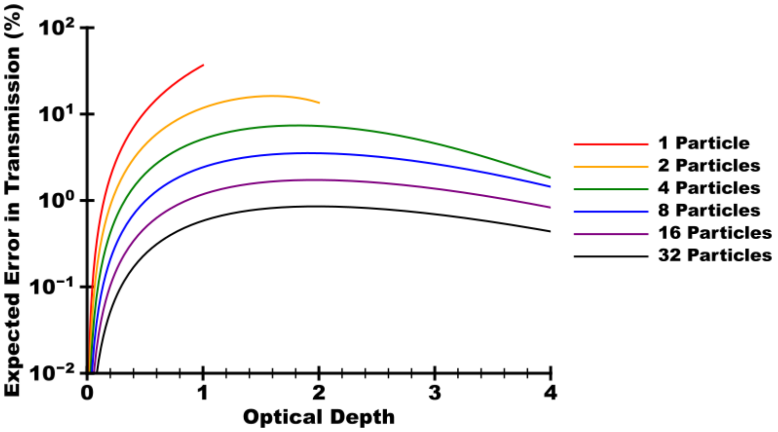

Figure 3.1: Predicted error in transmission of a finite set of particles as calculated by Equation 3.10.

side lengths of one unit filled with particles of diameter 0.01 unit such that the optical depth in a direction normal to any face is 0.5. The expected transmission is $e^{-0.5}$ or 60.7%. This can be calculated using a homogenized Monte Carlo ray trace, by emitting rays normal to one surface and determining if they traverse the cube. Traversal is determined by sampling a real number i on the range $[0, 1)$ and then determining the ray's distance to interaction with the cloud as $s = ln(i) * 0.5$. If s is less than one, then the ray is considered absorbed, if not, the ray traverses the cube. One can also consider taking the original cube and imposing a mesh (Figure 3.2). The ray trace would then be performed through multiple cells each with their own particles until the ray had traversed the mesh or had been absorbed. For simplicity, a linear cartesian mesh is considered with an equivalent number of elements in each direction. The opacity can be calculated in each element as the sum of the particle cross-sectional areas over the cell volume. The opacity multiplied by the ray path length is the optical depth. If many rays are traced, the transmission is approximately the fraction of rays which traverse the meshed cube.

Using a series of simulations, the transmission of the cube with respect to the refinement of the mesh is calculated. The mesh refinement is defined as the number of elements along each side. Since the cloud itself is unchanged by the refinement, a constant function should be anticipated (within the error of the Monte Carlo simulation). Furthermore, this constant value should be the expected transmission predicted by the Beer-Lambert Law in the unrefined case (i.e. 60.7%). However, the results of these calculations, as presented in Figure 3.3, show that this is not the case. As the mesh is refined, the transmission increases.

This numerical artifact exists because, as the mesh is refined, the number of particles in each cell tends toward small values (e.g. zero or one) where the Beer-Lambert Law has already been shown not to apply. In other words, Assumption *A.1* of the Beer-Lambert Law is invalidated. Even if the error committed in one cell is small (because the particle is small), that error is compounded over the many cells the ray traverses, leading to errors of multiple percentage points for the total transmission.

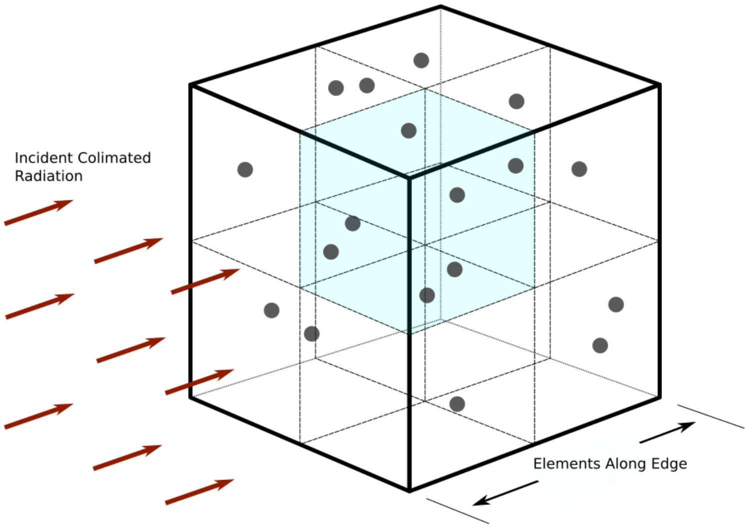

Figure 3.2: Diagram of the refinement simulations discussed in Section 3.4.3. A linear cartesian mesh is imposed on a cube filled with spherical particles of uniform diameter. Ideally, the transmission through the cube should be independent of the mesh. However, Figure 3.3 shows this is not the case with standard homogenization.

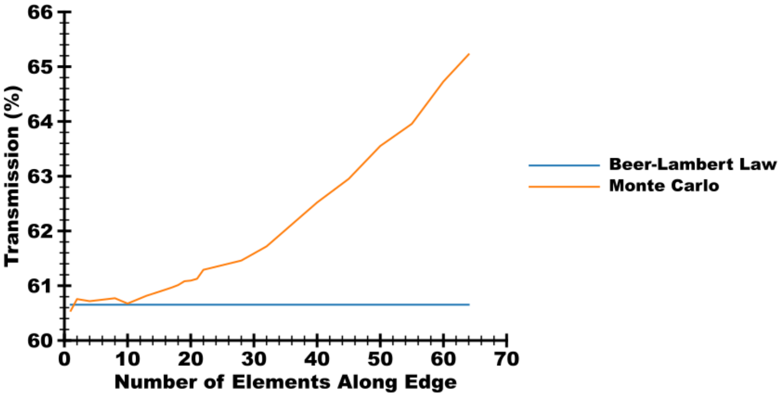

Figure 3.3: A graph of the transmission through a cube filled with particles with meshes of different refinement (see Figure 3.2). Each cell is homogenized according to the Beer-Lambert Law. As the cell size decreases the transmission rises. This unphysical behavior is a result of the finite number of particles present in each cell, as opposed to the infinite number of particles assumed in the Beer-Lambert Law.

3.5 Single Cell Simulations

To investigate the possible sources of error in the Beer-Lambert Law homogenization, high fidelity simulations of a small cell of particles are performed and compared to the results of homogenization of those particles. For this section, cubes of side length 1.0 unit are considered. The cube has a designated “front” face, which emits radiation of arbitrary intensity perpendicularly into the cell. The opposite face (i.e. the rear one) is a sensing element which measures the incoming radiation. The transmission is defined as the quotient of the sensed radiation on the rear face divided by the total front face radiative flux.

Inside the cube are purely absorbing particles of uniform diameter. Simulations are performed using various particle diameters, varying from .01 to .2 times the cell side length. The remaining “side” walls of the cell are given periodic boundary conditions such that a particle which penetrates a sidewall is copied such that the penetrating section appears through the opposite wall. This ensures that the optical depth of the cell is exactly the sum of the particles’ cross-sectional areas divided by the cell frontal area. Since the rays can only move parallel to the side walls, no ray motion thorugh the side walls is required.

Physically, the particles should be positioned such that no particle intersects another. This is accomplished using a hybrid algorithm of Wei [70] and Ebeida [71]. Both algorithms involve sampling particle positions on a subgrid. Wei’s algorithm is invoked while the subgrid cell size is much larger than the particle diameters. As the subgrid is refined, Ebeida’s algorithm is applied once the subgrid diagonal is smaller than a particle.

To calculate the transmission, a particle resolved Monte Carlo Ray Tracing (PrMRCT) simulation framework is used. In the method, rays are spawned randomly across the emitting surface, though their direction is always normal to the surface (per the boundary conditions described above). The rays are traced through the cell by first determining the impact parameter with each particle in the cell. If the impact parameter is less than the particle radius, the ray is absorbed. The rays that do not interact with particles are collected by the sensing surface. The transmission is then the number of traversing rays divided by the emitted rays. To get a statistically significant number of transmitting rays (at least 40% of all rays), 250 thousand rays are generated. This yields an error in the transmission due to the statistical noise of the rays at approximately 0.3%. More statistical noise is present from the finite number of cloud realizations.

Figure 3.4 shows averaged transmission data for a series of small cell simulations. Each data point represents a transmission averaged over 100 generated clouds. As the diameter of the particles increase, the transmission decreases beyond that predicted by the Beer-Lambert Law. Figure 3.5 presents the same data except the particles are allowed to intersect. One can see that the Beer-Lambert Law makes a much more accurate prediction for this case. However, particles are rarely allowed to intersect in any real cloud. Thus, for dense clouds with large particles, Assumption *A.2* is invalidated.

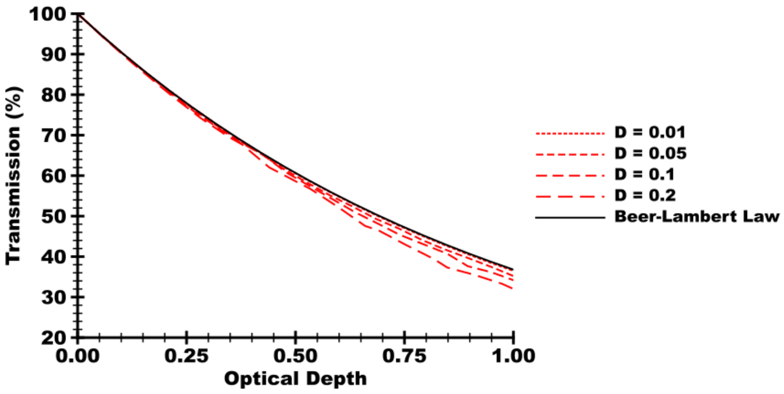

Figure 3.4: The same set of particle resolved simulations as shown in Figure 3.5, however, the particles are not allowed to overlap. This represents the physical configurations of solid particles. As the particles become larger, the Beer-Lambert Law over-predicts transmission.

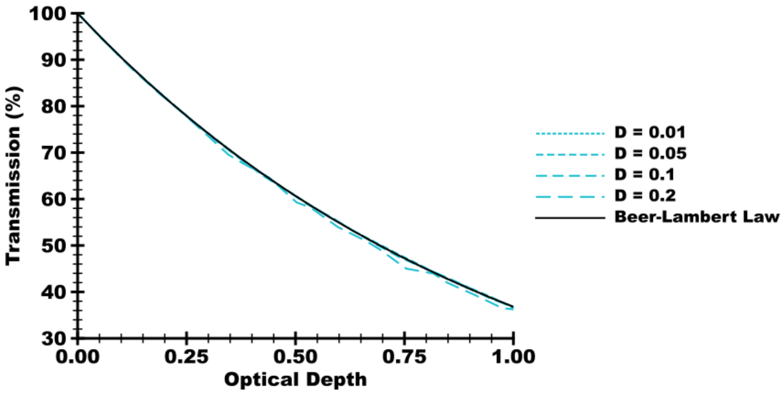

Figure 3.5: Results of serval particle resolved Monte Carlo simulations of particles in a single cell. The particle diameters are varied and the optical depth is changed by adjusting the number of particles. The particles are dispersed randomly and are allowed to overlap. One can see the Beer-Lambert Law can effectively predict the transmission for all these simulations.

3.6 Proposed Model

Given the results of the previous sections, it appears necessary to develop a correction to the Beer-Lambert Law that captures the physical properties of real clouds, i.e. the fact that the number of particles is finite and that the particles cannot intersect.

3.6.1 Derivation

Consider a prismatic cell of base area A and length L containing N_p particles of diameter D. Collimated radiation enters from the base in what will be referred to as the $\hat{x}$ direction. Instead of permitting each particle to reside in an independent $\hat{x}$ slab, a finite number of discrete regions are permitted. A representation of this situation is shown in Figure 3.6. The number of regions N_s is defined as

$$N_s = \frac{L}{\gamma D} \tag{3.11}$$

where γ is a scale factor depending on the shape of the particle. For cubic particles, this can be taken as 1. For spheres, a value of 0.7 is found to be effective. This factor expresses the geometric fact that particles in the same slab can slightly overlap if they are offset in $\hat{x}$ by a small amount.

The number of particles in each slab can be determined by a binomial distribution. The likelihood, p, of there being n particles in a given slab is given as

$$p(n) = B(n, N_p, \frac{1}{N_s}) \tag{3.12}$$

where $B(a, b, c)$ is the binomial distribution representing the likelihood of a successes of b trials where a success has a probability c. Using this distribution the expected number of slabs with a number of particles n, denoted $n_s(n)$ is simply

$$n_s(n) = N_s B(n, N_p, \frac{1}{N_s}) \tag{3.13}$$

Each slab is a two-dimensional radiative transfer problem, so the transmission rate, t, for one slab of n particles is

$$t = \left(1 - \frac{n\pi D^2}{4A}\right) \tag{3.14}$$

The total transmission T is then the product over all slabs which can be expressed as

$$T = \prod_{n=1}^{N_p} N_s B(n, N_p, \frac{1}{N_s}) \left(1 - \frac{n\pi D^2}{4A}\right) \tag{3.15}$$

3.6.2 Algorithm

The form of Equation 3.15 is not of a form suited to Monte Carlo simulations. However, one can develop an algorithmic approach that contains the same physics. It is assumed that each cell stores the number of particles, the particle cross-sectional area, and the cell volume. This is one more variable than Beer-Lambert Law homogenization, which only needs the cell volume and the total particle cross-section. When a ray enters a cell, the following process occurs.

1. The ray calculates the distance to the next cell wall. This is stored as L

2. The effective area A is approximated as the cell volume divided by L
3. An array of length N_s is initialized
4. For each particle in the cell, sample a random index on $[0, Ns)$ and increment the array at this index by the particle cross-section
5. Iterate over the array. At each element generate a random real number on the range $[0, A)$. If this number is less than the element's stored value, consider the ray to have struck a particle
6. If the entire array is traversed, the ray is transmitted

There are many possible variations on this algorithm depending on how one wishes to model a struck particle and the branch prediction optimization of a particular computer.

3.6.3 Results

One can compare the above algorithm against a standard Beer-Lambert Law homogenization in both situations where the Beer-Lambert Law mispredicted radiative transfer. Figure 3.7 shows the particle resolved radiative transfer through a disjoint cloud (identical to Figure 3.4) as well as the results of radiative transfer simulations using the proposed algorithm. The new algorithm captures the increase in absorption due to highly packed, disjoint clouds. This is because the algorithm creates a finite number of layers, producing less particle overlap and more transmission. The new algorithm over-absorbs at very large particles (diameter of 0.2 cell lengths). This occurs because the model for the number of slabs, given in Equation 3.11, is only correct in the first order for spheres. Densely packed spheres do not organize onto unique slabs. One could increase the accuracy of the model by taking higher-order terms such as

$$N_s = \frac{1}{\gamma_1}\left(\frac{L}{D}\right) + \frac{1}{\gamma_2}\left(\frac{L}{D}\right)^2 + \dots \tag{3.16}$$

However, this approach will increase computational cost. Furthermore, at these densities, the particles are close enough together that treating them as independent particles is likely insufficient for many real radiative transfer problems, such as optical transport, where wave effects would become relevant [33].

Figure 3.8 compares the results of a refined mesh over a cloud of particles with Beer-Lambert Law homogenization (as shown in Figure 3.3) against simulations with the same refinement using the new algorithm. The new algorithm preserves mesh independence of the radiative transmission due to a finite number of traced rays and a finite number of sampled clouds. There is still noise present due to the statistical noise of finite rays and finite cloud realization. The proposed algorithm is successful because the radiative transfer in each cell is approximately calculated as

$$t = (1 - \frac{\sigma}{A})^n \tag{3.17}$$

provided that the particle density is low enough that the independent arrangement approximation (*A.2*) holds. An algorithm built solely on Equation 3.17 would successfully predict the transmission of very refined meshes provided that particle density was low. However, the proposed algorithm has the increased robustness to treat highly refined or very dense particle fields.

One should note that this algorithm cannot reach infinite refinement. Once a particle becomes large relative to the mesh, it interacts with radiation in multiple cells anisotropically. The current algorithm will model any cell which contains an oversized particle as a completely absorbing cell. This leads to a voxel representation of the particle which is inherently inaccurate. To accurately predict transfer for such a situation, particle resolved methods must be employed.

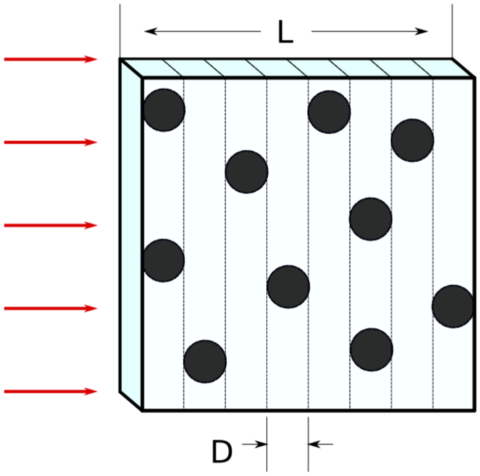

Figure 3.6: Schematic of parameters used to create the proposed radiative transfer model for solid particles. The finite number of slabs are calculated based on the particle diameter. The particles are then sorted into these slabs.

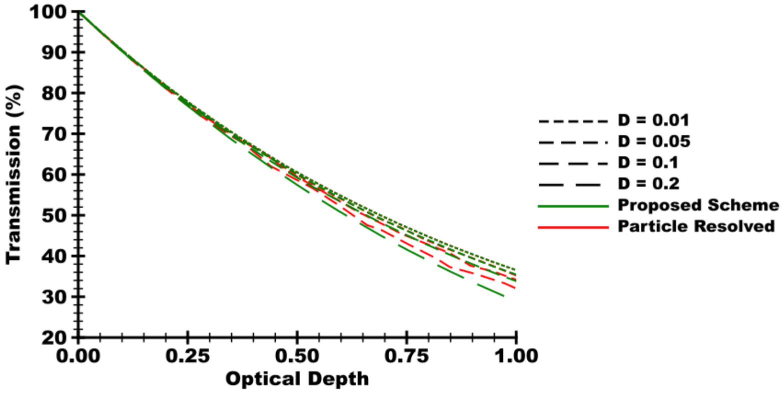

Figure 3.7: Comparison of the results of Figure 3.4 with results of the new model. The model captures the effect of decreasing transmission with particle size. The new model becomes inaccurate at the largest tested diameters (0.2 cell lengths) because it uses a low order description of the number of slabs (See Equation 3.11).

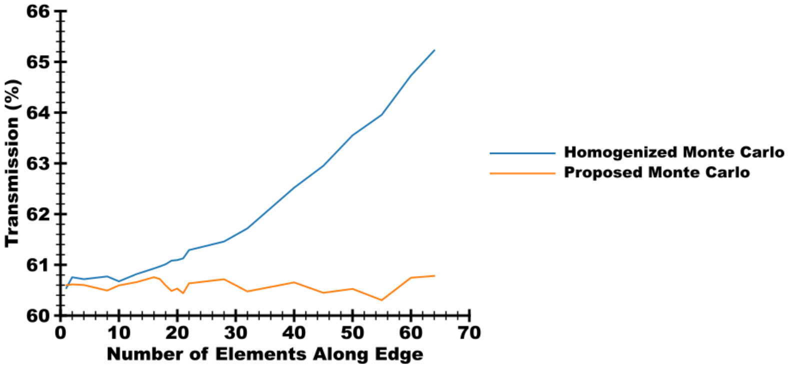

Figure 3.8: Comparison of the results of Figure 3.3 against the same simulation performed with the proposed model. The proposed model exhibits mesh independence. There is still the possibility of divergence with greater mesh refinement when the cell size and the particle diameter are comparable.

3.7 Conclusions

When modeling radiative transfer through particle clouds, it is customary to model cells of particles as a homogenized medium where the transmission likelihood is governed by the Beer-Lambert Law. This model is effective in many situations but can be invalidated in two cases. First, the number of particles can be too small, and second, the particles can be so densely packed that the fact they cannot overlap significantly affects their arrangement and radiative transfer properties. Monte Carlo simulations of simple radiative transfer problems have been presented which exhibit both of these effects.

To enable simulation in these regimes, a new algorithm has been presented which accurately calculates the radiative transfer through such particle clouds, at the cost of storing at least one more variable in each cell. The algorithm calculates the radiative transfer by creating a series of two-dimensional slabs. The number of particles in each slab is sampled at every ray trace. It was shown that the model exhibits better mesh independence as well as accurately capturing the higher absorption observed in very dense clouds. This algorithm does not provide for infinite mesh refinement, it is still limited to cells that are larger than the particles they contain.

CHAPTER 4

Analysis of a Particle Laden Flow

4.1 Brief Overview of Multiphase Flows

Flows which involve materials of different phases are a common occurrence in the natural world. Gaseous species can enter a liquid as bubbles, liquid droplets can be suspended in gas, and solid particles can travel in both. These added phases can change the properties of any flow. This occurs for several reasons. First, the addition of another phase will change the local density of the flow (a liquid with air bubbles, for example). Also, the added material itself can experience velocities which are different from the local fluid velocity (e.g. rain in a gust of wind). Momentum transfer, through drag forces, can alter the velocity distribution of both phases in a highly time-dependent way. Analysis of these flows necessarily involves considering the coupled system at once, including what is often a very complex internal geometry and structure.

This study will focus on a gas flow altered by the addition of solid particles. This has been leveraged in man-made systems and has created deviations in natural flows from what continuum theory would predict. Heat and momentum transfer can be altered with the addition of particulate. They have a variety of applications, including aerosol deposition properties [72] and aircraft combustors [16]. The turbulent flow of this kind features a unique particle clustering. The strength of the clustering is dependent on the time scale of the particles [28].

Many of these regimes also experience high temperatures where radiation effects are relevant. Situations such as rocket exhaust [73] and solar heat collectors [74] involve a coupled physics environment of turbulent gas, particle drag, and radiative heating. The heating of a flow can alter the local gas properties (e.g. density and viscosity). This can then alter the fluid properties, the particle clustering, the local absorption properties, and therefore the radiative heating. A fluid-particle-radiation flow is highly coupled, involving disparate physics.

Numerical methods are necessary to analyze flows of this type. The computing power necessary to produce accurate simulations has only become available within the last two decades. However, the necessary fidelity to model these flows is still unknown. This study analyzes a single aspect of these flows: the radiative heating due to clustering. Using new data from a benchmark particle-laden turbulence study (Section 4.2), radiative transfer models can be used to analyze the required fidelity of the model and validate simulations of the coupled system.

4.2 Analyzed System

This study will focus on the experiment carried out at Stanford University, reported by Villafane et al. [58] and Banko et al. [75, 76]. The apparatus consists of a long, square duct with 4 cm sides. Atmospheric air is pulled into the duct. There are four principal regions:

the injection region, the development region, the radiative heating regions, and the outlet region. In the injection region atmospheric air is pulled into the duct while at the same time adding particles by means of a screw hopper. The screw hopper is calibrated to add particles at a given mass flow rate. The air particle mixture then enters a long region with a Reynolds number that is sufficiently high to ensure that turbulence is fully developed. The flow then enters the radiative heating region. In this region the metal duct walls are replaced with a glass test section. The glass walls have a thickness of 2 mm. This 16 cm x 4 cm x 4 cm region has the same cross sectional area as the duct; however, it permits light to enter and interact with the particulate. Once the flow has passed through this region, temperature measurements are made on the flow, the particles are filtered out, and the air is rejected to the atmosphere.

The particles used in this experiment were nickel microspheres; their diameters were measured using a Coulter counter. The average particle diameter was approximately 12 microns.

When discussing the quantity of particles in the flow, it is useful to define two quantities. The Mass Fraction Ratio (MFR) and the Mass Loading Ratio (MLR) are defined as

$$MLR = \frac{\dot{m}_{Ni}}{c}\dot{m}_{air}MFR = \frac{\bar{\rho}_{Ni}}{\bar{\rho}_{air}} \tag{4.1}$$

where $\dot{m}$ is the mass flow rate of the species and $\bar{\rho}$ is the average density. Note that because of turbophoresis effects, local density of particles in air may drastically differ from the average density taken over the entire duct area and length. It is also important to note that the MLR and the MFR are not the same value. Because particles have a tendency to move to

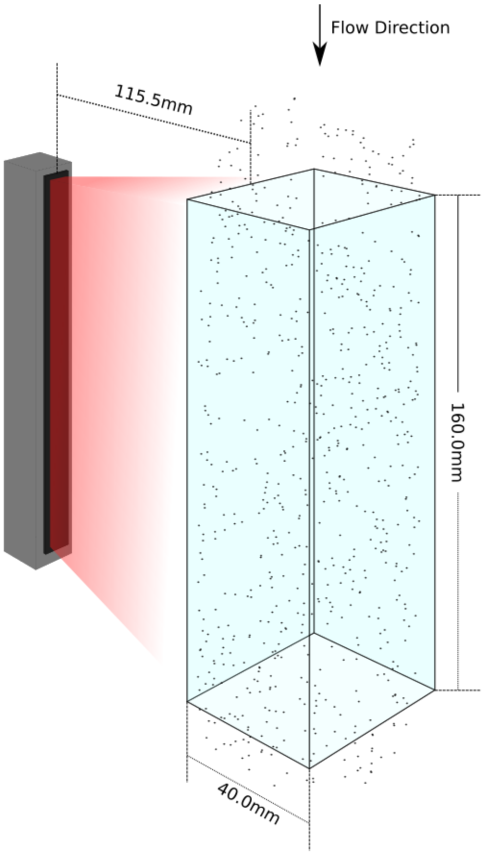

Figure 4.1: Schematic of radiatively heated. A single laser diode array is shown at left illuminating the glass test section contain the turbulent air-nickel mixture.

the boundary layer (generally particles move to areas of high shear), they have a tendency to move slower on average than the air that is carrying them. This causes the density of particles to rise, leading to a MFR that is, in general, higher than the MLR. The radiative section can be heated using two different sources, a large laser diode array and a single laser (detailed in Section 4.3.2.1). The diode array is the primary heating source, outputting up to 2 kW of energy. A diagram of this heating source and the test section is shown in Figure 4.1

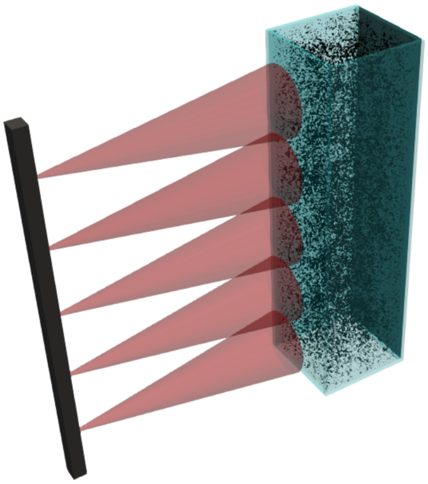

Figure 4.2: Simple rendering of the full system with one active laser diode array. The particle shown are results of the coupled simulations (Section 4.3.1). The volume is 4 cm by 4 cm by 16 cm. The blue glass is 2mm thick and is modeled as a pure absorber. The red cones denoting the incident radiation are only approximations for clarity (See Section4.3.2.1 for details).

4.3 Numerical Methods

4.3.1 Coupled system Model

Although this analysis will focus on the radiative transfer through cloud snapshots, these clouds have to be generated using a fully fluid-particle-radiation solver. Discussion of this solver can be found in [32,77]. The simulation is a compressible Direct Numerical Simulation (DNS) with Lagrangian point-point particle tracking. Radiative transfer is computed using a discrete ordinate solver.

To address the polydispersity of the particle, the particle diameters are binned into five unique diameters. These are given in Table 4.1. The Stoke's numbers of these particles are on order 10. Momentum is two-way coupled between the fluid and the particle and momentum is transferred between particle collisions.

Table 4.1: Tabulated properties of nickel particles used in simulation modeling

Diameters	8.369, 9.761 11.153 12.197 14.634 μm
Material Density	$8900 kg/m^3$
Index of Refraction at 973 nm	$2.4704 + 5.5117i$
Index of Refraction at 632 nm	$1.9900 + 4.1057i$

To model the entire apparatus, the simulation uses a two step procedure. First the particles and fluid are initialized in a periodic channel domain. Once the simulation has run to fully develop a turbulent flow, the outlet is copied to another nonperiodic domain where heating occurs.

The number of particles are initialized with a given mass fraction of particles to air. This is not the same as the mass flux ratio that is measured in the experiments. Because particles tend to move into the slow moving boundary layer, the mass flow ratio tends to be less than the mass fraction. The periodic simulation therefore had to be iteratively adjusted until the time averaged mass flow matched experimental measurements.

Radiative transfer analysis is performed on a series of instantaneous snapshots of particle positions in the heated test section. For the one array heating case, 5 MLR = 20% and 14 MLR = 40% snapshots are taken. Three snapshots of other heating cases (Section 4.5.5) are also used.

4.3.2 High Fidelity Radiative Heat Transfer Model

To simulate the radiative energy distribution throughout the system, several numerical methods are available. One could directly solve the electric and magnetic fields through the system. This has several limitations due to computational times. If a finite element method were to be used, the cell size would have to be on the order of a wavelength. The wavelengths inside the particle are on the order of 0.2 microns (due to the increased index of refraction). For a system that is on the scale of tens of centimeters, the total number of computation cells in three dimensions would have to be greater than $1 \cdot 10^{17}$. Also, one could make an aggregated T-matrix representing the entire particle cloud [78–80]. The state of the art for this method has been performed on thousands of dense packed particles. Mackowski and Mishchenko [81] could perform this calculation in 10 hours using a large high performance computer. These particles did not individually require a large number of harmonics. The nickel particles of interest are not only larger, requiring more harmonics, but the average snapshot contains tens of millions of particles. Assuming a linear scaling, this would require over a year to calculate using Mackowski's and Mishchenko's computational resources, if the computational time scales as the number of particles to the third power (as is usually estimated for matrix inversion) then the time required extends into the centuries.

Performing a complete electromagnetic analysis also required accurate modeling of the emission sources. Gaussian beams can be analytically described. However, the multiple laser sources that are used in this system defy a simple model, especially in terms of spherical harmonics. This issue is also present in discrete ordinates methods (DOM). DOM uses an Eulerian mesh that stores the intensities as a function of discrete directions. This is useful for situations where the intensity is relatively uniform with respect to solid angle; however, in the current investigation, the laser source must travel through a large, empty volume before interacting with the particles. This requires either quadrupling the mesh size to include the emission region or developing a complex boundary condition on the glass surface.

The difficulties of a direct electromagnetic simulation or a DOM simulation can be mitigated by employing a Monte Carlo ray tracing (MCRT) method. MCRT can easily trace rays from the emission source to the cloud boundary *and* navigate the stochastic particle clouds. The disadvantage of this method is that statistical noise can dominate field features. For example, the required time to predict the radiative heat transfer to a single particle may be extremely large. However, for integrated quantities such as the transmission or the total absorption, MCRT has a distinct advantage in computation time.

The Monte Carlo analysis is performed on a single time instance (a snapshot). Because the particle temperature rise is small, radiative emission from the particles is neglected. The total radiative field is also assumed to be monochromatic. Rays are traced in three stages: emission, tracing, and sensing.

4.3.2.1 Ray Emission Model

In the experimental apparatus, several radiative sources were used. The primary heating mechanism was an array of laser diodes. However, small laser beams were also used for some measurements. Each of these sources had a unique positional and directional emission pattern. Capturing these variations proved paramount to accurately predicting the transmission and absorption properties of a particulate cloud.

The laser diode array is composed of a series of sub-arrays attached end to end. A single sub-array is a square chip with side lengths of 4.8mm. This chip is, in reality, composed of several discrete emitters; however, the variation in emission power across the chip is neglected. This chip is surrounded by a housing that is 0.9 mm thick such that when the sub arrays are placed end to end, the spacing between each chip is 1.8 mm. Twenty four sub-arrays are attached together to make a single, 16 cm array (see Figure 4.3). This array

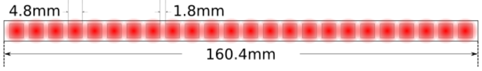

Figure 4.3: Schematic of the laser diode array. Light is emitted from square chips, 24 of which are arranged in a long array.

is mounted 11.55 cm away from the glass wall of the test section and is arranged so that the longest axes of the emitter and test section are parallel.

The emission from any point is rated as a 9alf angle cone. This is interpreted to mean that the emission in spherical coordinates takes a gaussian distribution in zenith angle, i.e.

$$P(\Omega) \sim e^{-\frac{\theta^2}{(9^\circ)^2}} \tag{4.2}$$

where Ω is solid angle and θ is the zenith angle.

The experimental apparatus contained three of such arrays outlined above. One was aligned with the channel centerline, and one was mounted on either side so that the offset in array centerlines was 12.7 mm. Because overheating of the glass channel could lead to catastrophic failure of the apparatus, only two configurations were ever run: the single center array was activated at 1 kW and the two outer arrays were activated at either 0.5 kW or 1lW each. These conditions will be described as the one array or two array conditions respectively.

Numerically, the rays are sampled first by selecting the array at random (for the two array case), then by selecting the chip at random and lastly by sampling across the single 4.8mm square at random. The ray is initialized 11.55 cm away from the test section. Once the ray position is selected, the direction is calculated using an exclusion method. If two real numbers are sampled, one, denoted θ, on the range 0 to $\pi/2$ and the other (α) on the range 0 to 1.0. If the condition

$$\alpha <\sim e^{-\frac{\theta^2}{0.02467}} \tag{4.3}$$

is met, where $0.02467 = (9^\circ)^2$ in radians, then the ray is initialized, otherwise both α and θ are resampled.

Other emission sources were also considered. A Gaussian beam was modeled by selecting an initial position from emission. A radial offset was sampled from a normal distribution. The experimental width of the beam was 0.6mm with a 99% power width at 3mm. A slight beam divergence is also included as

$$\beta = \frac{\lambda}{\pi\mu}\frac{r}{\mu} \tag{4.4}$$

where λ is the emitted wavelength, mu is the Gaussian width and r is the sampled radial offset.

To compare with the work of [77], several plate sources were also included as approximate models for the laser array. All rays were sampled uniformly across the outer face of the glass test channel. Three different direction samplings were considered: perfectly collimated, the same 9mission, and an isotropic emission. Note that all these direction samplings were azimuthally symmetric. A ray sampled at the far right of the channel could be initialized in a direction such that it would move towards the far left of the channel.

The last aspect of modeling the experiment was to include a model for the glass. The glass is modeled as a pure absorbing medium. In reality, it is known that the glass is 3.5%

reflective with a small diffractive component. However, it is found that the reflectance or absorption had a negligible effect on prediction while increasing run time substantially. In the present simulations, the glass is given an opacity of 20.715 m^{-1}. This leads to a total absorbance of 3.5% over 2 mm.

4.3.2.2 Ray Tracing Model

The majority of the computation time of the radiative transfer simulation is devoted to calculating the ray transfer through the particles. The primary method used to calculate the ray trajectory was a particle resolved Monte Carlo ray tracing (PrMCRT) approach. This method captures and stores in the positions, diameters, optical properties, and incident radiance of each particle separately.

The optical wavelengths of interest in this analysis are on the order of one micron. The particle diameters are all on the order of 10 microns. The size parameters, χ, defined as

$$\chi = \frac{\pi D}{\lambda} \tag{4.5}$$

where D is the particle diameter and λ is the incident wavelength. The size parameter for this regime is on the order of 30. This is too small for a geometric optics approximation to be valid [3]. Mie theory is employed to calculate the absorption and scattering properties. Mie theory uses the particle size, incident wavelength, and material index of refraction to calculate the energy transfer into the particle and into space. These energy fluxes, divided by the incident flux, yield the particle cross sections. These can then be normalized by the particle's geometric cross section to yield the efficiency.

The particle geometric cross section is denoted σ_g. The cross sections for scattering and absorption are denoted σ_s and σ_a respectively. The sum of the two, or the total energy loss cross section, called the extinction cross section, is denoted σ_e. The efficiencies for scattering and absorption are denoted Q_s and Q_a.

The scattered energy from a particle is generally a function of solid angle and polarization. However, for a spherical particle in unpolarized light, this distribution reduces to only a function of zenith angle (with respect to the incident beam). This function is denoted $P(\theta)$ where θ is the zenith angle. However, the probability for a ray to scatter at a particular zenith angle is equal to $P(\theta)sin(\theta)$. This function, which will be called the scattering function, is the true probability density of scattering angles. It is the integral of this function that is stored, representing a cumulative distribution function of scattering angle.

The particle resolved method uses a hard sphere model to determine the ray-particle interaction. However, the critical impact parameter of the particle is defined as $\frac{\sqrt(Qe)D}{2}$ where D is the particle geometric diameter. This is determined as

$$\frac{|\vec{R_d} \times (\vec{P_p} - \vec{R_p})|}{|\vec{R_p} - \vec{P_p}|} < \frac{\sqrt(Qe)D}{2} \tag{4.6}$$

where $\vec{R_d}$ is the ray direction and the quantities $\vec{R_p}$ and $\vec{P_p}$ are the ray and particle positions respectively. Figure 4.4 shows a schematic of this process. Calculation of the impact parameter is only performed if the particle center is in front of the ray.

When a particle interacts with a particle, it is transported forward until the direction to the particle is exactly normal to the ray direction. This calculated as

$$\vec{R_p} + \vec{R_d}\cot(\vec{P_p} - \vec{R_p}) \rightarrow \vec{R_p} \tag{4.7}$$

where → represents the changing of the value on the left side. The ray energy is attenuated by a factor of Q_s/Q_e. A scattering angle is determined by sampling a number of the range 0 to 1 and finding the respective angle on the stored distribution function. Scattering occurs away from the particle center on the scattering plane (the plane formed by the ray direction and the relative position of the particle). The ray direction is updated as

$$\vec{R_d}cos(\theta) - sin(\theta)\frac{\vec{P_p} - \vec{R_p}}{|\vec{P_p} - \vec{R_p}|} \rightarrow \vec{R_d} \tag{4.8}$$

where θ is the determined scattering angle. The care to ensure that the ray scatters in the plane containing the particle center is necessary to ensure that the ray does not re-intersect with the particle. Because the test for ray impact is only performed on particles that are in front of the ray and because this scattering algorithm necessarily places the particle behind the ray, re-scattering on the same particle cannot occur.

Although the particle resolved method should, in theory, not require any other information besides a list of all particles in the domain, inclusion of a mesh is necessary to reduce the number of particles that need to be searched at any ray tracing step. By sorting all particles onto the mesh, the list of particles that must be tested for collision is greatly reduced. However, the sorting procedure must include all particles that intersect with the mesh, not only those whose centers line in the mesh. For a linear cartesian cell, this is a trivial calculation.

It has been found that for the studied cases, because the energy flow is primarily in one direction, highly skewed elements lead to the fastest run times. This maximizes the possible length a ray can travel if the cell is empty and minimizes the number of possible particles that need to be searched for impact if the cell is not empty.

At times it is useful to compare the particle resolved method to a traditional homogenization method. A homogenization provides an opacity, β to each cell defined as

$$\beta = \frac{\sum_{particles} Q_e \sigma_g}{V} \tag{4.9}$$

where the quantity $Q_e \sigma_g$ is accumulated for every particle whose center lies in the cell, and V is the cell volume. A ray which enters a cell calculates a distance to interact with a particle by sampling a random number, α, on the range 0 to 1. The distance to interaction, d, is calculated as

$$d = \frac{ln(\alpha)}{\beta} \tag{4.10}$$

If d is less than the distance to the cell wall, the ray moves that distance. A particle is selected at random in the cell to determine the optical properties. The ray is attenuated by a factor of Q_s/Q_e, and then scatters by an angle θ. Because no particle is present, the azimuthal scattering angle is selected randomly. This is done by randomly sampling a unit vector $\hat{p}$. Using $\hat{p}$ and θ, the ray direction is updated as

$$cos(\theta)\vec{R_d} + sin(\theta)\vec{R_d} \times \hat{p} \rightarrow \vec{R_d} \tag{4.11}$$

There are several ways to implement a homogenization scheme. Using the same opacity, one can alternatively create an algorithm to decide to either completely scatter a particle or completely absorb the particle. There is also a version where two opacities are calculated, one for scattering and one for absorption. The ray continuously attenuates and only scatters discreetly. All of these methods are equivalent in the limit of many rays. The method outlined above is chosen because it is most similar to the particle resolved approach.

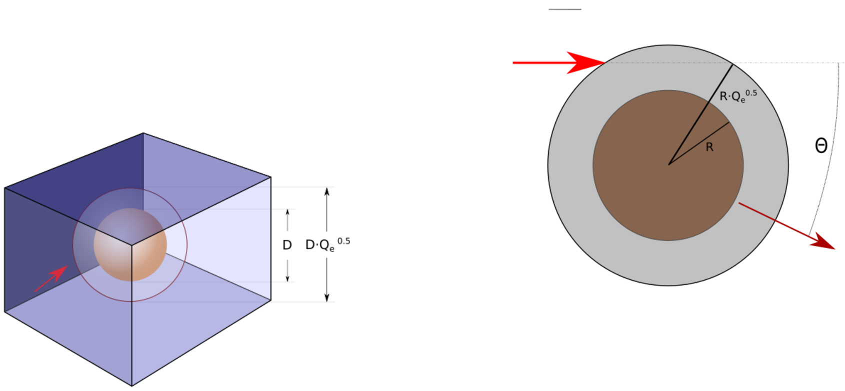

(a) Ray trace through cell (b) Ray motion in scattering plane

Figure 4.4: Schematic diagram of particle scattering in a cell, 4.4a, and on the scattering plane, 4.4b

4.3.2.3 Ray Sensing Model

When rays traverse the particle domain, they are first traced through the glass as described in section 4.3.2.1 then they are traced to a sensing patch. The patch may be located arbitrarily in space. To match experiments, two sensing patches are considered. The first is a large patch the same size as the outer channel wall (4.4 cm by 16 cm) which represents the thermal calorimeter used in the experiments to measure the transmitted emission from the laser diode arrays. A small 3.5 mm square photosensor was also employed to measure local transmittance from the single laser source. The sensor was located 16.5 cm away from the channel wall.

All sensors used were numerically discretized into 400 by 400 grids to capture the spatial variation across the surface. However, all comparisons to experiments only consider the integrated values.

4.4 Results

Using the methods outlined above. Simulations were performed to answer specific uncertainties about numerical methods necessary to accurately predict transmission and to validate the models.

4.4.1 Emitter Modeling

In section 4.3.2.1, the exact emission model for the laser diode array was discussed, as well as simplified models. These included a collimated plate source (such as used by Farbar et. al. [77]), a similar plate source but with the same directional pattern as the experimental array, and an isotropic source.

When analyzing these sources, there are three transmissions that can be calculated: the transmission of just an empty channel (but with the glass side wall), the transmission of the channel with particles, and the transmission of just the particles, which is calculated by dividing the previous two transmissions.

For each emitter two PrMCRT calculations were performed, one with an empty channel and one with a single snapshot of the MLR 0.4 flow. The energy fluxes impinging the colorimeter for the empty case are shown in Figure 4.5. The same data for the cases with particles is shown in Figure 4.6. The various transmissions are tabulated in Table 4.2. It is expected that the transmission of the emitters varies with the geometry of the emitter. However, it is also clear that the measured transmission of *only* the particles is dependent on the emitter model. The relative error, for example, between the particle transmission of the exact array model and of the collimated model is 3.44%.

Table 4.2: Calculated transmission comparing various emitter models.

Emitter Type	Transmission Without Particles (%)	Transmission with Particles (%)	Particle Transmission (%)
Collimated	83.68	64.01	76.50
9° Cone	78.68	61.17	77.74
Isotropic	28.11	22.06	78.47
Experimental 1 Strip	76.54	60.64	79.23
Experimental 2 Strip	61.59	48.25	78.33

4.4.2 Small Beam Simulations

In Section 4.4.1 it was shown that the modeling of the emitter needed to be modeled to high fidelity in order to accurately capture the transmission of the particles. When modeling the small laser beams, the same is true for the sensor.

To reduce computational cost, modeling the sensor beam is reduced to a 2 cm by 2 cm by 4 cm core that is extracted from the centerline of the channel. By sampling many cores from multiple clouds, a higher sample size can be produced. Figure 4.10 shows the transmission averaged over all cases for both the offset sensor case and the case with no offset. The

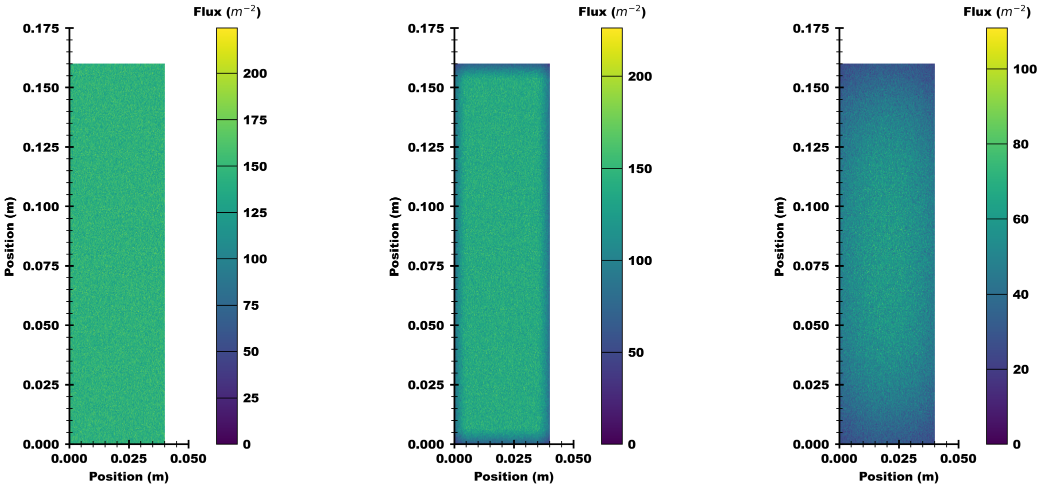

(a) Collimated Plate Source (b) 9onical Plate Source (c) Isotropic Plate Source

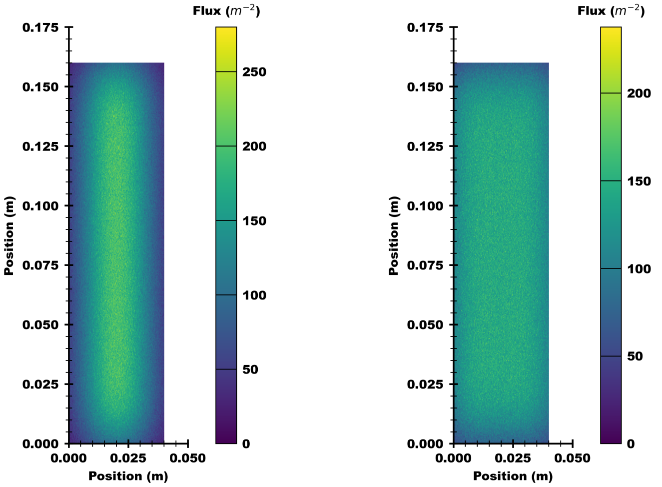

(d) Single Array (e) Two Arrays

Figure 4.5: Incident flux, as seen by the experimental calorimeter, from various emission sources. The flux is normalized by the total emitted power, and therefore, has units of m^{-2}

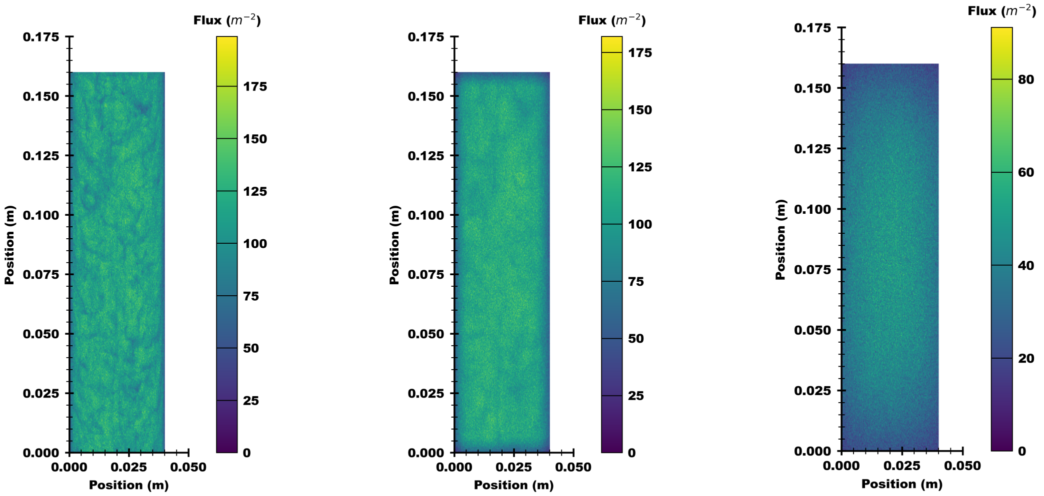

(a) Collimated Plate Source (b) 9onical Plate Source (c) Isotropic Plate Source

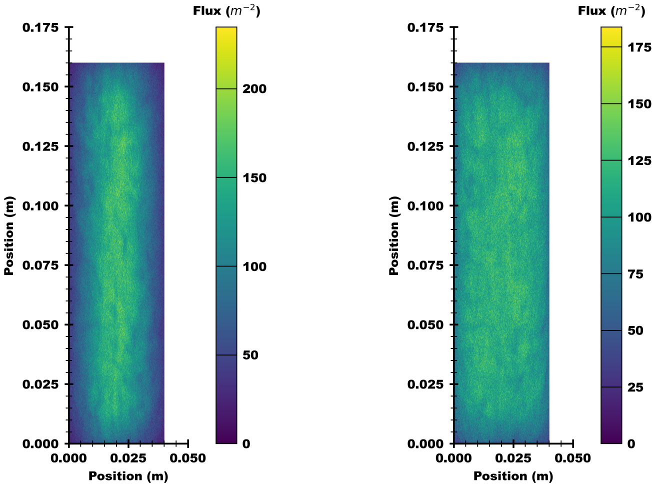

(d) Single Array (e) Two Arrays

Figure 4.6: Incident flux, as seen by the experimental calorimeter, by various emission sources, with particles in the channel. The flux is normalized by the total emitted power, and therefore, has units of m^{-2}

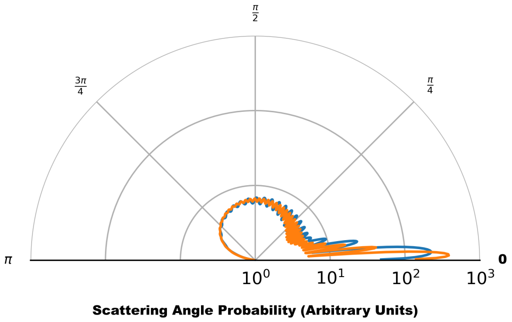

Figure 4.7: Scattering functions of the largest and smallest particles under consideration.

addition of the offset reduced the transmission by approximately 15%. This is because the scattered light that would hit the sensor in the offset case misses the sensor as it is drawn away from the channel.

Figure 4.11 displays the spatial variation of absorption along the beam path. Five lines are plotted, one representing the boundaries of the quartiles of all samples. This shows that all simulations have an increase in absorption near the wall (due to particle clustering there). The variation in absorption, however, is relatively small near the wall. The maximum absorptions occur in the channel center. This is where fast, dense clusters of particles move quickly through the channel. The average absorption is much lower in this region, however.

4.4.3 Mesh Refinement with Homogenization

Because the cloud snapshot exhibits significant clustering, considering the cloud as a homogenous block of a given opacity is unlikely to result in accurate predictions. It is useful to determine, however, if there exists a length scale over while elements of the cloud can

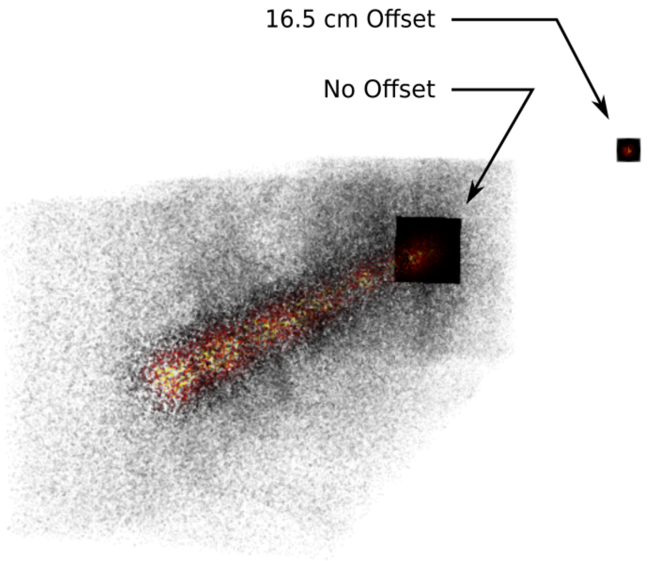

Figure 4.8: Rendering of the small beam simulations with illuminated particles and both sensing patches visible.

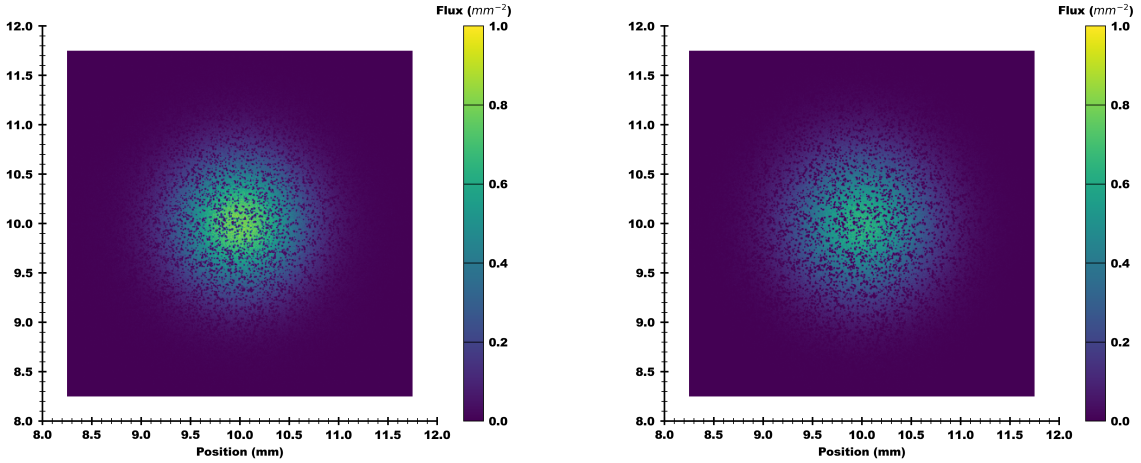

(a) No Offset

(b) Offset

Figure 4.9: Incident fluxes as seen by the sensing area. Two sensors are shown, one with a 16.5 cm offset from the outer channel wall and the other that is against the channel (no offset). The incident fluxes are normalized by the total energy emitted by the source (units m^{-2}).

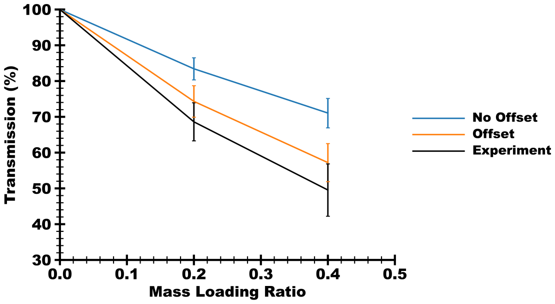

Figure 4.10: Average transmissions predicted by PrMCRT using a sensor which is offset 16.5cm from the channel. The same simulations are performed without this sensor offset. The addition of the offset dramatically changed the perceived transmission of the flow. All error bars represent the standard variation of the transmission over all simulations (or over time in experimental measurements). Note, however, that the high fidelity sensor modeling still overpredicts transmission.

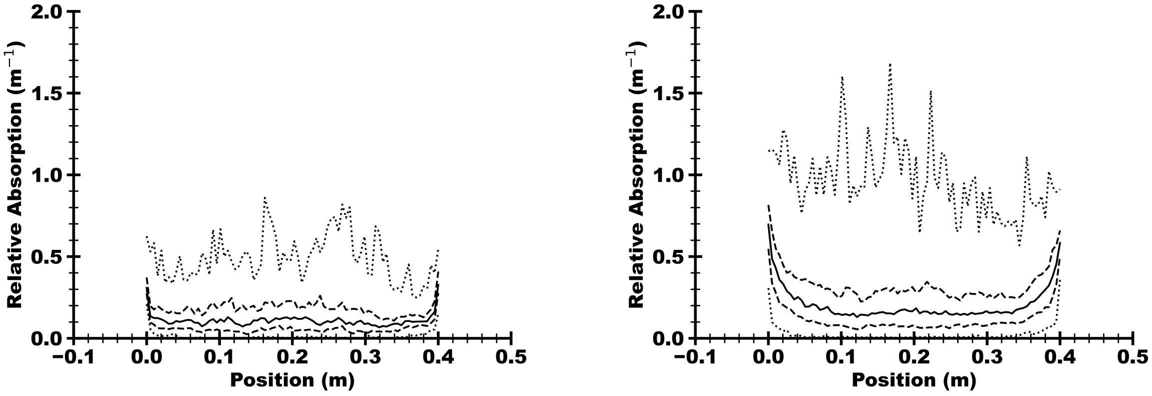

(a) MLR = 20%

(b) MLR = 40%

Figure 4.11: Absorption along the channel line for both Mass Loading cases. Each line represents a quartile boundary (e.g. the bottom line represents the minimum absorption and the middle line represents the median absorption).

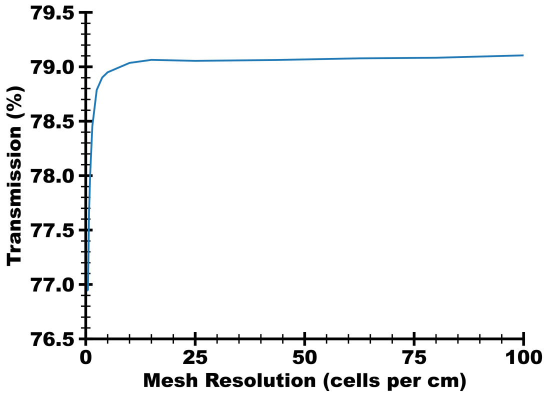

Figure 4.12: Transmission of a single MLR 40% snapshot using homogenization over the cells. Different linear cartesian meshes are used with increasing resolution.

be homogenized. This is tested by homogenizing a single snapshot with various meshes. All meshes are linear cartesian meshes with an equal number of particles in each direction. (Because the domain aspect ratio is 1 to 1 to 4, the elements have the same aspect ratio.) As this number of elements increases, the volume homogenized becomes smaller. One expects that as the cloud is homogenized, the transmission will tend to a constant value (assuming the mesh size remains larger than a particle diameter).

Figure 4.12 shows the results of such a mesh refinement study on a single MLR 40% snapshot, the emitter is the signal array model. One can see that the single homogenized volume (the leftmost point on the curve) differs in transmission by only 2 %. The mesh refinement has little effect when resolution reaches 25 cells per centimeter. This is equivalent to a cell width of 0.4 mm and a length of 1.6 mm.

4.4.4 Particle Resolved vs. Homogenization

Section 4.4.3 showed that homogenization led to a converged solution when the mesh was refined to approximately 100 elements for side length. However, it did not address if this converged solution was equal to the transmission of a PrMCRT solution.

Another open consideration is the use of the delta-isotropic approximation. Figure 4.14 shows that the particle optic efficiencies are weakly dependent on the particle diameter. Furthermore, Figure 4.7 shows that the majority of the scattered energy is only slightly deflected. This suggests that all particles can be modeled with a single absorption efficiency and isotropic scattering efficiency. The isotropic scattering efficiency is defined as

$$Q_{si} = Q_s(1 - g) \tag{4.12}$$

where g is the scattering asymmetry parameter. As is shown in Section 4.5.5, this model can reduce the transmission to a function of only this pair of efficiencies.

The results of all single array simulations are presented in Figure 4.15. A rendering of the absorbed energy in the particles as well as the energy incident on the calorimeter is shown in Figure 4.13. The transmission results for all MRCT methods lie within 1% of each other. This suggests both that a homogenized model is sufficient to capture the transmission, and that a delta isotropic model is sufficient to capture the particle optical properties. However, all predictions lie outside of the experimental data.

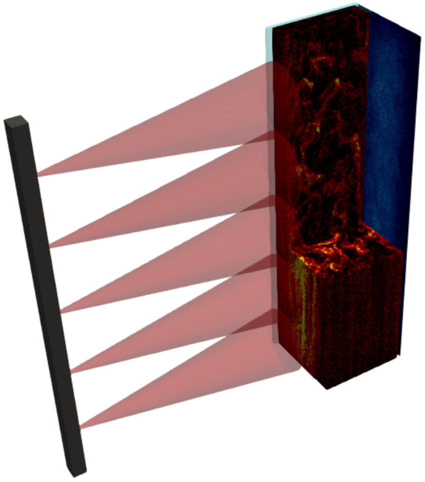

Figure 4.13: Simple rendering of the full system with one active laser diode array. A spatial averages fluxes along the colorimeter sensor is shown in blue and the total absorbed energy is shown in red. The cones denoting the incident radiation are only approximations for clarity.

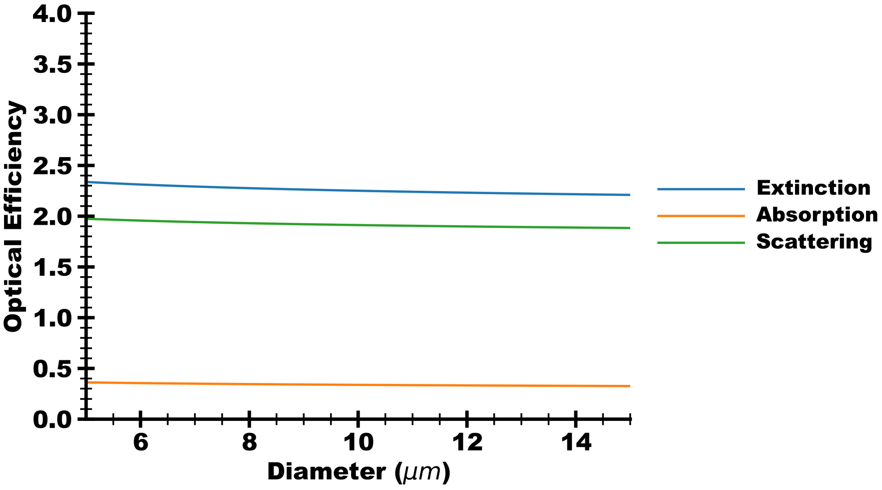

Figure 4.14: Optical properties of nickel particles of various diameters in 973 nm light. The index of refraction is 2.4704 + 5.5117i.

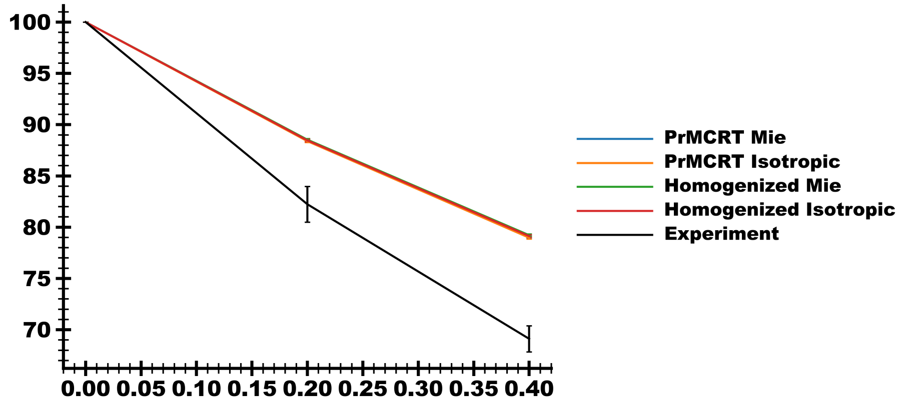

Figure 4.15: Transmission of a single MLR 40% snapshot using homogenization over the cells. Different linear cartesian meshes are used with increasing resolution.

4.5 Discussion

In all simulations presented, the transmission was over predicted compared to the experimental measurements. This could easily be explained by a reasonable change in the absorption properties of the particles. However, a physical mechanism would be required for this change. A series of analyses are performed to examine the optical behavior of the particle to various transforms.

4.5.1 Mie Properties

The Mie calculation is dependent on three quantities: The size parameter, χ of the particle with respect to the incident light, and by the real and imaginary parts of the index of refraction of the material. The incident wavelength is considered well quantified, and Figure 4.14 has shown that the optical properties are relatively insensitive to the particle diameter. However, the index of refraction of a material experiences a complex behavior both with respect to frequency and temperature. Figure 4.16 plots the optical properties of a 12 micron particle exposed to 973 nm light. The nominal nickel index of refraction is taken to be $2.4704 + 5.5117i$ [82]. Although the extinction and total scattering efficiency are relatively insensitive to the index of refraction, the relative change in absorption or isotropic scattering efficiency optical efficiency is equal to the relative change in the index of refraction within a 10% variation. This suggests that a change in the index of refraction may affect the transmission.

4.5.2 Oxide Coating

In section 4.4 it was assumed that the particles could be modeled as pure nickel spheres. However, there was potential for a layer of nickel oxide (NiO) to have formed on the surface of the hot particles. Yang's method [53] was employed to calculate the optical properties with thin concentric layers. The index of refraction of NiO is estimated as $1.8 + 0.01i$ [83–85]. This assumes that the particle's temperature rise is well below 100.

Figure 4.17 displays all of the optical properties of particles of various diameters and nickel oxide shell depths. A shell depth is shown here, as opposed to an added thickness, because the experimental measurements would have measured the total diameter regardless of the particle composition. The X axis of these figures is directly comparable to experimental measurements. The optical properties of the particles are more strongly dependent on the shell depth as opposed to the particle diameter. However, significant changes in the isotropic scattering efficiency or the absorption efficiency do not occur until the shell is approximately 50 microns thick.

Farbar's analysis [77] also included an analysis of nickel oxide. However, the nominal shell

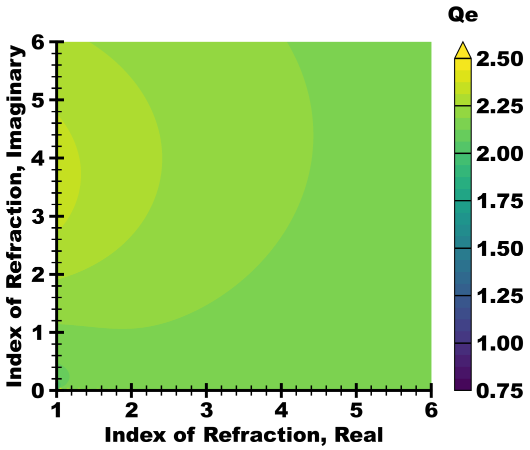

(a) Extinction Efficiency

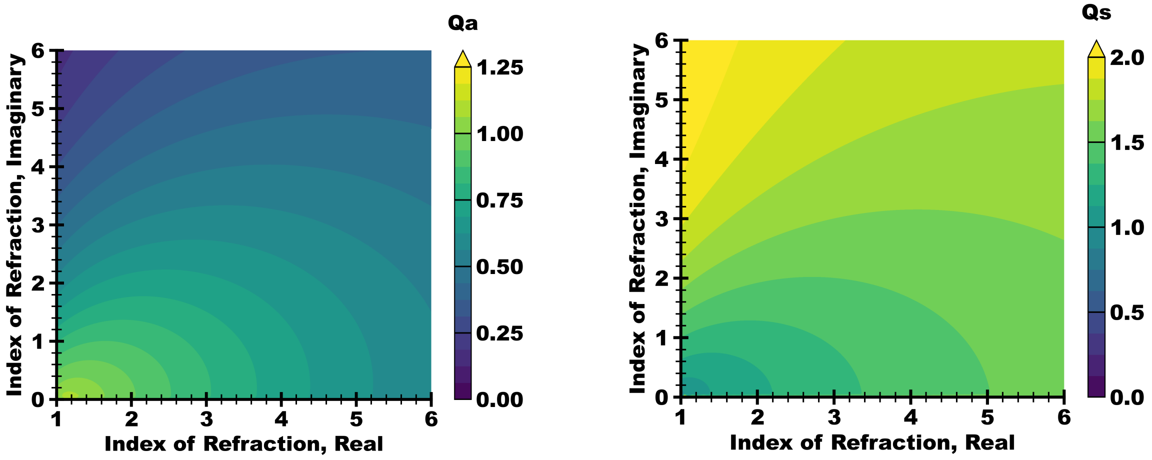

(b) Absorption Efficiency

(c) Scattering Efficiency

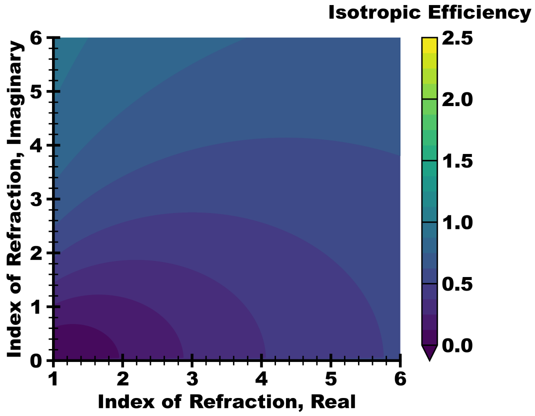

(d) Isotropic Scattering Efficiency

Figure 4.16: Scattering properties of a nickel particle of diameter 12 microns in 973 nm light with various indices of refraction. Note, the expected index of refraction is 2.4704 + 5.5117i. At this value, the optical properties are relatively insensitive to the index of refraction.

depth was taken at 60 nm, while the index of refraction of NiO was taken to be $2 + 10^-6i$. Figure 4.18 displays the optical properties of a 11.153 micron particle (the mean particle diameter) with a 60 nm NiO shell, with various indices of refraction for the NiO. One can see that the optical properties are relatively insensitive to the imaginary part of the index of refraction. The variation between a real part of 2 and 1.8 is less than 10% for the absorption and isotropic scattering efficiencies. However, because they change in opposite directions, their sum, the extinction efficiency, changes by less than 2%.

4.5.3 Spheroid Particle

Analysis of the particle properties has assumed that the particles are approximately spherical. However, it is known that the actual particles used could have significant elongation. Farbar [77] studied surface roughness as a possible source of increased absorption. This was done by analyzing Chebyshev particles [51] whose overall shape was, on average, still spherical.

Spheroidal particles have the potential to increase the overall absorption, because the geometric cross section can be increased in certain orientations. Because the particles are still in the Mie regime, a wave optics approach is necessary to calculate the optical properties accurately.

Following Farbar, an extended boundary method was used to calculate the optical properties of spheroids of various elongations (ratio of major to minor axis). However, due to numerical instability of the extended boundary method [57], no calculations could be performed. A surface impedance formulation of the extended boundary method was employed

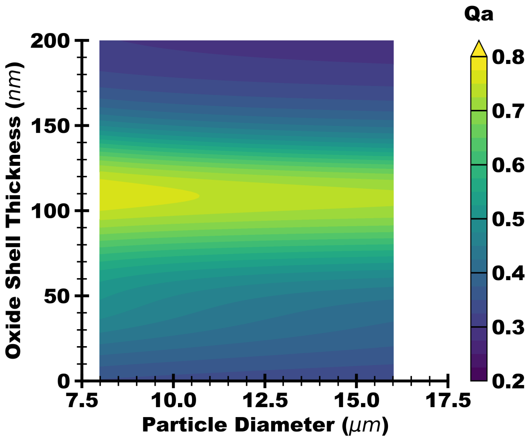

(a) Extinction Efficiency

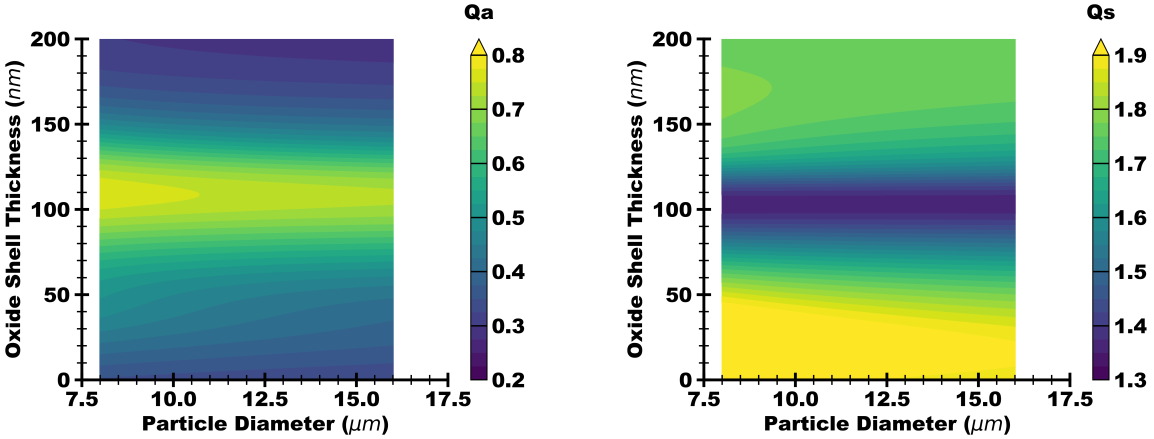

(b) Absorption Efficiency

(c) Scattering Efficiency

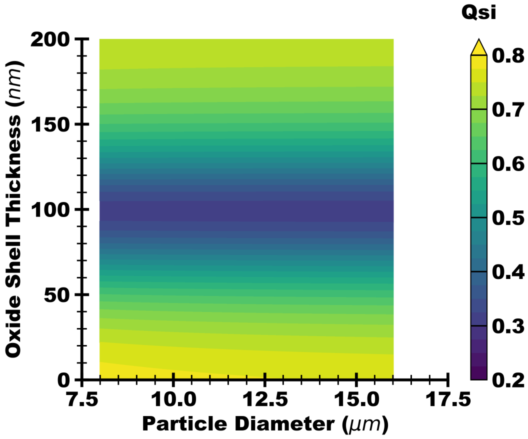

(d) Isotropic Scattering Efficiency

Figure 4.17: Scattering properties of nickel particles of various total diameters and oxide shell depths. The index of refraction of the pure nickel is 2.4704 + 5.5117i and the pure oxide is 2 + 0.015i.

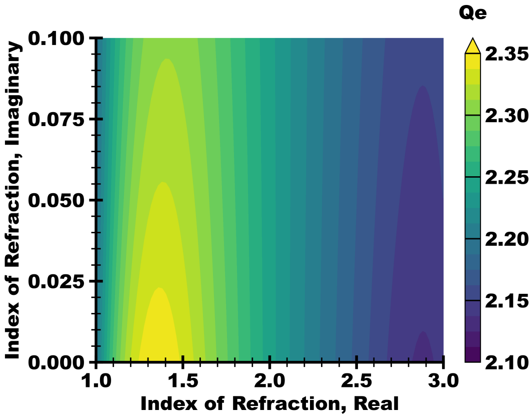

(a) Extinction Efficiency

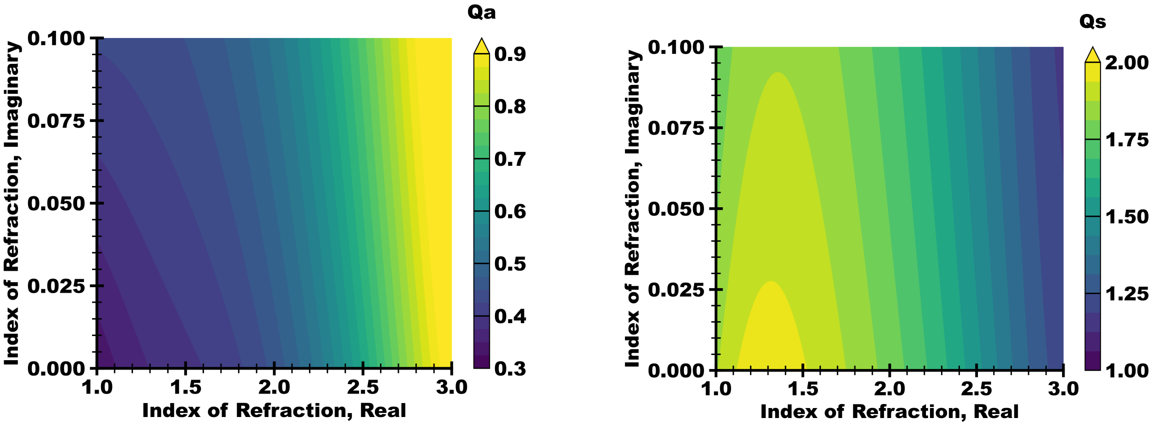

(b) Absorption Efficiency

(c) Scattering Efficiency

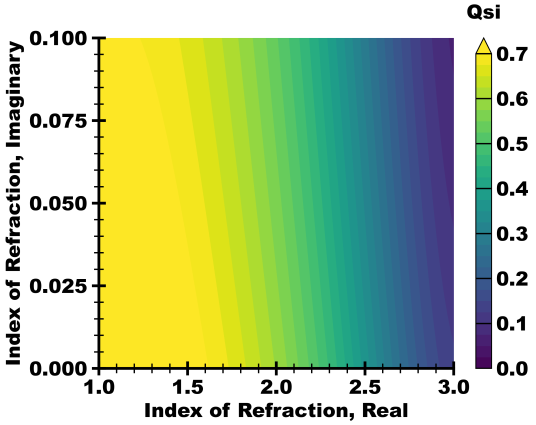

(d) Isotropic Scattering Efficiency

Figure 4.18: Scattering properties of a nickel sphere of diameter 12 microns in 973 nm light with various indices of refraction and a 60 μm nickel oxide shell. Note, the expected index of refraction of the pure nickel is 2.4704 + 5.5117i and the pure oxide is 2 + 0.01i. The optical properties are relatively insensitive to the index of refraction.

to calculate the optical properties. The optical efficiencies, normalized against a spherical particle of diameter 12 microns, for spheroids of various elongations and orientations are plotted in Figure 4.19. One can see that an individual spheroid can have significantly different optical efficiencies., but each is balanced out by a spheroid of the opposite type (i.e. prolate vs oblate) and by a 90hange in orientation.

Because the coupled simulation does not track angular information of particles, there is no means of determining if there is a statistically more probable orientation for particles in the flow. If the particles are indeed randomly oriented, however, then the change in the optical properties is unaffected by spherical vs. spheroidal particles.

4.5.4 Magnetic Particles

In the optical regime, the magnetic permeability is rarely taken into account, as for most materials the permeability is low at such high frequencies. Most materials cannot change eddy current at gigahertz frequencies. However, it was hypothesized that a slight magnetic permeability could slightly change the optical properties from that of a pure dielectric. Figure 4.20 displays the change in optical efficiencies with magnetic permeability. Ferromagnetic effects are negligible at these frequencies, and nonlinear susceptibility is negligible at these field strengths. Magnetic permeability can drastically alter the optical behavior of these particles. However, this only occurs once the magnetic permeability reaches 1.1. It is known that in the cm wavelengths the magnetic permeability rapidly approaches one [86]. Thus, a magnetic permeability of 1.1 in the micron wavelength region is considered unreasonably high.

4.5.5 Particle Sticking

In the previous sections, it has been suggested that particles of various shapes and compositions are unlikely to affect the overall transmission of the entire flow. This can be shown succinctly by calculating the transmission for a single cloud snapshot (MLR = 0.4) as a function of particle properties. The effect of changing the material properties of the particle can also be plotted on the same contours. This is done in Figure 4.21. Similarly, the total absorption can be plotted as a function of Q_a and Q_{si}, shown in Figure 4.22. Note that the particle changes all are plotted to extreme quantities. The magnetic permeability is changed to 1.30. An oxide layer 100 micron thick is shown, as well as changes of 30% in the real and imaginary parts of the index of refraction.

Figure 4.21 also plots a single contour for the experimentally measured transmission. Notice that none of the potential changes in particle properties can significantly change the overall transmission. Any increase in absorption is counteracted by a decrease in scatter and vice versa. This leaves the transmission insensitive to the particle properties. Because the instantaneous absorption cannot be measured, no such contour is plotted in Figure 4.22. This is unfortunate, because the absorption is clearly only sensitive to the particle absorption efficiency. As a matter of future work, determining the relation between the instantaneous absorption and the downstream temperature rise would more clearly determine the particle properties.

Because the transmission is unaffected by any changes to the particle properties, other means of adjusting the cloud properties must be considered. The most probable cause of increased absorption is the effect of particles sticking to the wall of the channel. During the experiment, particle sticking was observed. However, it was assumed that all particles stuck permanently to the wall. Therefore, after the experiment was concluded, a transmission measurement was made with no flow but with the stuck particles. This transmission was used to normalize the transmission measurements presented by Banko et. al. [76]. (Note that all experimental data presented here has used the initial transmission measurement for normalization.) This difference was generally on the order of 1%-2%.

It is possible that instead of only permanent or specular particle collision, there were a significant number of particles that stuck to the wall for a period of time then released, or stuck to the wall and then rolled down the glass surface at very low speeds. These effects are not present in the coupled simulations, where all particle-wall collisions are energy conserving, specular reflections. This effect would increase the mass fraction of particles with respect to the mass flow fraction, increase the total amount of particles present in the test section, and decrease the total transmission.

Analyzing the effect of the wall collision model on the flow features is beyond the scope of this study. However, the PrMCRT method can be used to estimate the number of particles that need to be bound to the wall to match experiments. This is adding a percentage more particles to the side walls of the simulation (care being taken to ensure no particles overlap). Figure 4.23 shows a rendering of a snapshot with the added particles and without. The transmission as a function of added particles forms a very linear trend which can be solved for the exact quantity of particles that must be added. Figure 4.24 shows an example of this process.

In this analysis, every array transmission measurement is analyzed using this procedure, this includes data at two different mass loadings, laser diode array configurations, and emitted power. Six cases are analyzed in total, and the results are tabulated in Table 4.3.

Table 4.3 shows that for all heated cases, at least an additional 60% more particles are necessary to match experiments. The area fractions, that is the sum of the cross sections of added particles divided by the total glass area is no greater than 11 %. The total absorption at a single wall is less that $Q_a \cdot 0.11 * I_0$. The quantity of added particles follows physically meaningful trends. In the two array cases, the number of particles added increases as the power level increases (from Case 3 to Case 5 and from Case 4 to Case 6). However, the single array requires more particles than the two array cases for the same power level. This suggests that the likelihood for particles to stick is dependent and positively related to the incident flux. The single array case has a narrower beam than the two arrays cases, hence a high flux at the centerline. One can also note that the percentage of particles added decreases with increasing MLR; however, the total number of particles added is still increasing. This suggests that the quantity of particles added scales approximately as MLR^{γ} where γ is a number less than one. For the two strip cases, a gamma of 0.6 matches the trends.

Since the quantity of particles stuck to the walls is dependent on MLR and the incident flux, it is likely that the number of particles that are actually stuck to the channel walls is over-predicted by this analysis. This is because the side wall experiences very little flux. It appears unlikely, based on the present data, that the walls would experience a formation of particles to such a degree as those walls normal to the diode arrays.

Table 4.3: Transmission results for multiple heating and mass load cases, followed by the number of particles necessary to be added to the wall to match experimental measurements.

Case	1	2	3	4	5	6
Mass Loading Ratio	20%	40%	20%	40%	20%	40%
Number of Arrays	1	1	2	2	2	2
Emitted Power (kW)	1	1	1	1	2	2
Original Trans. (%)	88.56	79.01	88.65	77.87	88.76	77.95
Particles Added (%)	91	82	71	54	82	61
Added Area Fraction (%)	6.18	10.63	4.29	6.03	5.24	7.09
Adjusted Trans. (%)	81.81	68.59	83.67	71.12	83.04	70.36
Measurement (%)	82.24	69.12	83.71	71.18	83.05	70.39

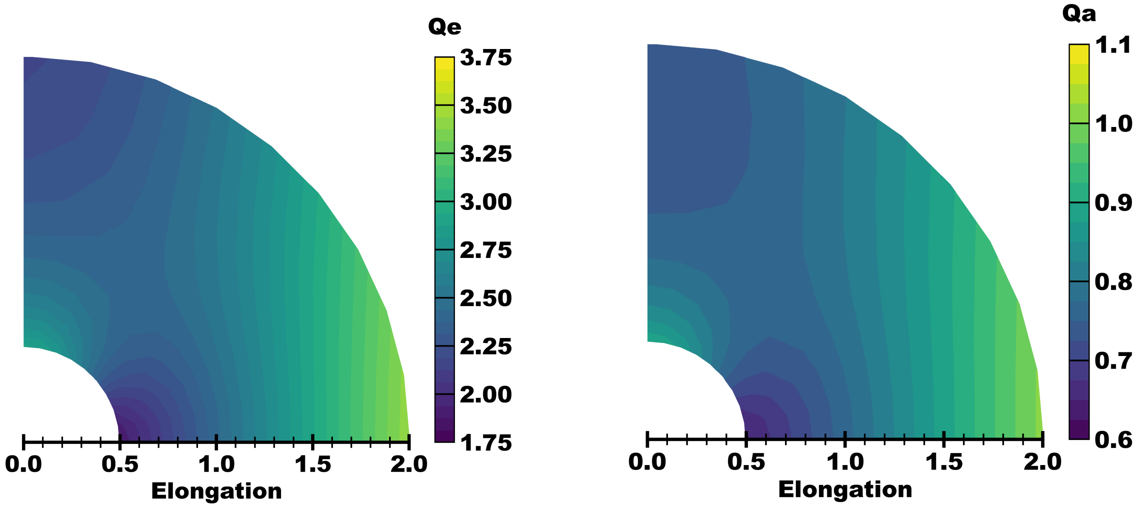

(a) Extinction Efficiency

(b) Absorption Efficiency

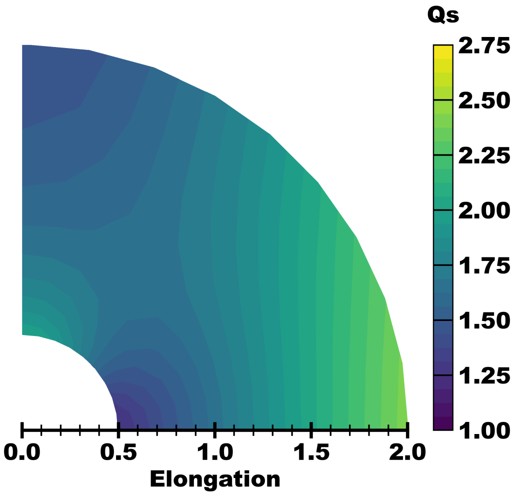

(c) Scattering Efficiency

Figure 4.19: Optical efficiencies of spheroidal particles with an index of refraction $2.4704 + 5.5117i$ and varying elongations but an effective diameter 12 microns.

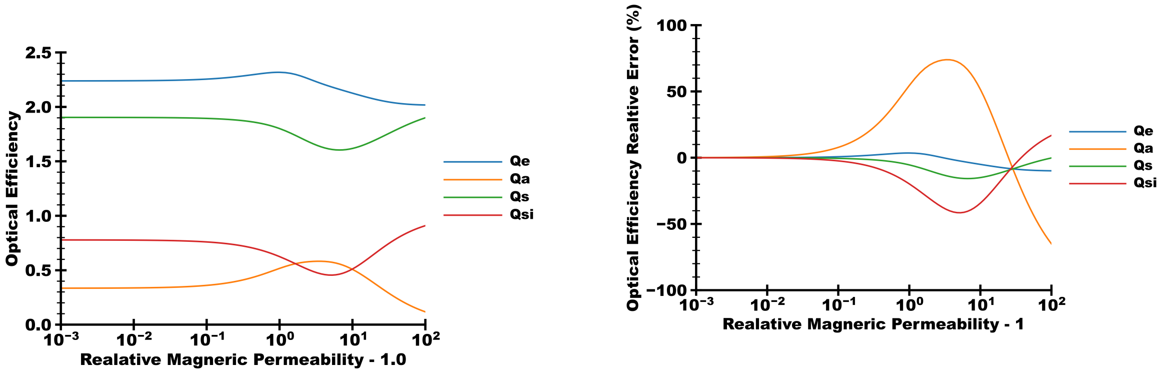

(a) Optical Efficiency

(b) Relative change in optical efficiencies compared to the $\mu_r = 1$ case.

Figure 4.20: Change in optical properties of a 11.226 micron diameter sphere exposed to light of wavelength 973 nm (index of refraction $2.4704 + 5.5117i$) with respect to magnetic permeability.

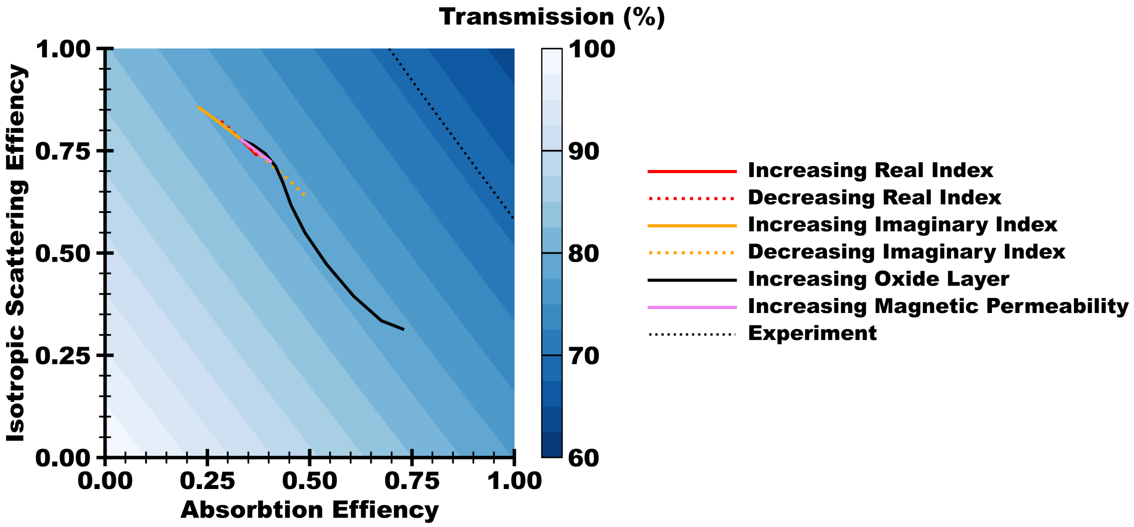

Figure 4.21: Results from PrMCRT simulations with particles of various scattering and absorption properties. The changes in particle optical properties with respect to material properties are overlaid. The experimentally measured transmission for this case is shown as a single contour line.

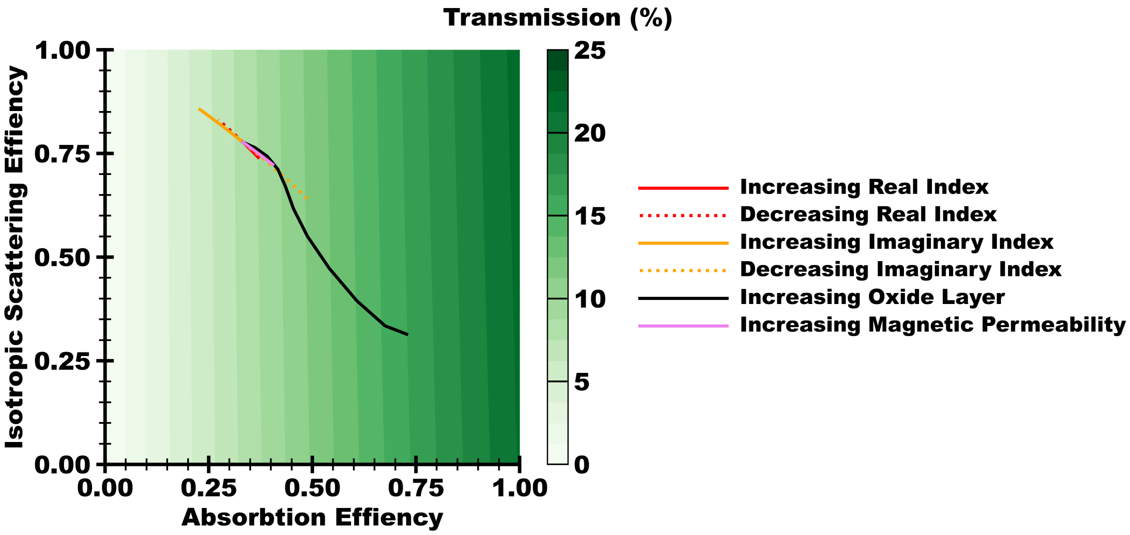

Figure 4.22: Results from PrMCRT simulation with particles of various scattering and absorption properties. The changes in particle optical properties with respect to material properties are overlaid.

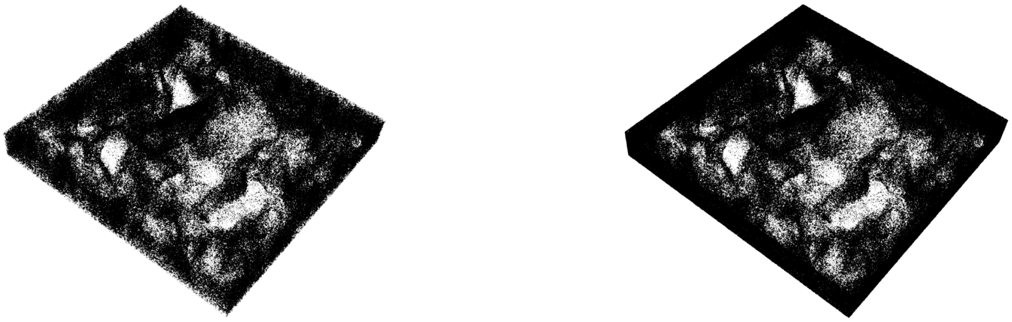

(a) Original Snapshot

(b) Snapshot with added particles

Figure 4.23: Renderings of additional particles added to channel side walls, only a 5 mm slice in the flow direction is rendered.

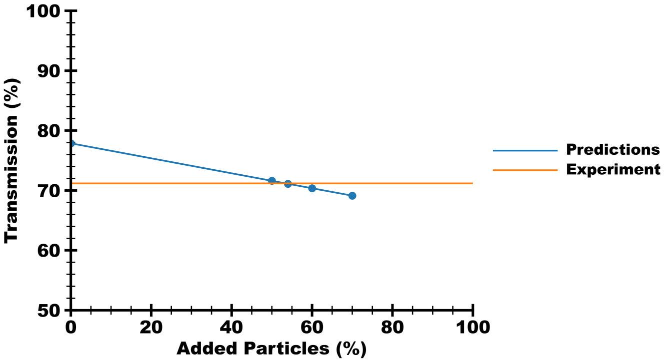

Figure 4.24: Example of predicted transmission with additional particles added to the channel walls. An estimate for the number of bound particles is performed by solving a linear fit at the experimentally measured transmission.

4.6 Conclusions

In this study, a particle laden flow experiment was analyzed using a coupled flow solver and a high fidelity Monte Carlo ray tracing method. The focus of the study was to accurately calculate the transmission and to validate these predictions with experimental measurements. It was shown that the transmission predictions were highly sensitive to the fidelity of the emitter and sensor models. The particles themselves were modeled with several ray tracing methods. It was found that the transmission was insensitive to the particle resolved approach versus a homogenized one (provided the mesh was sufficiently refined). The particle transmission was also unaffected by a change from an exact Mie scattering profile to a uniform isotropic scattering model.

Initial predictions overpredicted transmission by 5% in all cases examined. Multiple avenues were considered to account for the sources of error, focusing on the optical properties of the particles. However, it was found that no particle property could be a reasonable source of the transmission error. It was concluded that the particle clouds themselves could be a source of error.

It was hypothesized that the particles could have an additional mechanism which amplified their attraction to the duct walls, thereby raising the MLR with respect to MFR even higher. By adding wall-bound particles to snapshots examined previously, one could predict the quantity of particles that would need to be attached to the walls at any given instance. This yielded consistent trends over multiple emitter configurations, power levels, and Mass Loading Ratios. It is concluded that a particle attraction to the wall is the best avenue for further study of this experiment as well as the study of radiatively active particle laden flows.

CHAPTER 5

Radiative Transfer Through Reacting Gas Flows

5.1 Introduction

Exploration of outer gas giants has been met with new interest [87]; however, missions to these remote planets come with unique difficulties. A probe with enough velocity to arrive at such a far orbit must be moving at extremely high speed. Any object which attempts to enter the atmosphere of one of these planets is doing so at velocities of approximately 25 km/s. At these speeds, dissociation and ionization occur strongly, and the heat load on any heat shield increases. Furthermore, these atmospheres are composed primarily of hydrogen and helium. Producing experiments that completely replicate the entry conditions into a hydrogen-helium atmosphere such as Saturn's, for example, is extremely difficult. Numerical methods are required to calculate the fluid and radiative environment.

Radiative calculations are important because the heat loading applied by these flows may have a significant radiative contribution. Furthermore, analysis of the spectral intensity of flows at particular positions is one of the few methods available for ascertaining information about the flow composition and temperature. Experimental measurements of radiative transfer provide the richest data to verify computational models.

Although reacting flows of this type can be analyzed by Computation Fluid Dynamics (CFD), these methods cannot fully calculate the radiative environment. Radiative calculations require knowledge of the number of atoms and molecules in each of their excited states. Each of these states must be treated as its own species in a CFD framework. For a large grid, this volume of data can become intractable. These State to State models (StS) have been applied in a single dimension, but are not practical for design purposes.

The current state of the art is to run CFD with simplifying assumptions about the distribution of excited states which are encoded in one or multiple temperatures (e.g. two temperatures and Arrhenius chemical rates). Once these populations are determined according to spatial conservation laws, the excited state populations are calculated locally according to some set of rules. In earlier decades, this distribution of states was taken to be in thermal equilibrium (a Boltzmann distribution). However, it is now possible to solve the quasi-steady-state (QSS) assumptions at flow points. This can only be done by organizing chemical rates for each excited state in the flow. These chemical rates as a group will be referred to as the QSS model for a species or set of species.

The excited-state populations calculated according to QSS or Boltzmann models can be significantly different and lead to radically different radiative transfer predictions of the system. However, both excitation models are based on the original population calculated by simplified CFD rates. QSS methods are considered more accurate, although they rely on the accuracy of experimental data or quantum mechanical calculations for the rate coefficients. The development of an accurate QSS model is an important step in validating CFD models.

Analysis of these CFD rate models for aerospace applications began in earnest during the Galileo mission to Jupiter. Flight data had been useful to evaluate the accuracy of existing aerothermal models. The Galileo mission resulted in several studies examining the aerothermal environments experienced during the entry phase [88–90]. The deceleration module of the Galileo Probe entered Jupiter at 47.4 km s^{-1} resulting in a peak heat flux of 30 kW cm^{-2} [91, 92]. Analog resistance ablation detector (ARAD) sensors were embedded in the forebody of the thermal protection system (TPS) that measured the total recession of the TPS material.

The ARAD data revealed that *a priori* analysis under-predicted the recession by at least 50% over the entire frustum region. The recession data available from flight prompted a number of studies that investigated this discrepancy. Matsuyama et al. [93] performed a trajectory-based heating analysis by including coupled fluid-radiative transfer calculations and the injection-induced turbulence model proposed by Park [94]. Their simulations resulted in better agreement in the frustum region but enhanced the discrepancy at the stagnation point. Park further analyzed the discrepancy at the stagnation point by including the effect of spallation and modifying the thermodynamic coefficients (values in the JANAF database) of H and H^+ [95]. A better agreement at the stagnation point was achieved by Park because the expelled particles (spallation) from the heat shield could act as radiation blockers in the flowfield. It is important to note that the spallation phenomena were not modeled explicitly. The attenuation of radiative intensity was estimated based on the concentration of expelled particles obtained from experiments [88]. Additionally, the JANAF coefficients were corrected for a lower ionization potential.

Both the studies assumed thermochemical equilibrium for modeling the flowfield. More recently, Erb et al. [96] performed a detailed study that included shape change in the trajectory analysis and assessed the validity of modeling assumptions regarding diffusion, radiative heating, and ablation. They found that the improved agreement relative to past studies was due to the notable impact of shape change, multi-component diffusion, and ray-tracing radiative heating. While a finite-rate chemical kinetic model was used for their study, thermal non-equilibrium was not accounted for and a one-temperature model was used in their analysis [96]. Since the entry velocity of Galileo was so extreme, the density and pressure rise across the shock would likely result in thermal equilibrium. However, the proposed entry conditions into Saturn and Uranus are at much lower velocities (26 and 22 km/s respectively) and a thermochemical non-equilibrium treatment is required under certain conditions.

Palmer et al. [97] used the state-of-the-art two-temperature approach to evaluate entry conditions into Saturn and Uranus. As part of that effort, they updated collision integrals to compute transport properties (viscosity, diffusivity, and thermal conductivity) and vibrational relaxation times based on the latest ab-initio data [98–100] and high-fidelity state-to-state modeling [101]. The updated values showed differences in the shock standoff distance and non-equilibrium regions for entry conditions relevant to Saturn. However, Palmer et al. [97] used a heritage chemical kinetics model from the 1970s based on shock tube experiments from Leibowitz and Kuo [102]. Work from Park et al. [103] indicates that the ionization rate in the shock tube experiments of Leibowitz was likely incorrect from post-shock radiation contamination of the data. Furthermore, one-dimensional state-to-state models have been developed by Colonna et al. [104, 105] and Munafò et al. [106]. These investigations have shown that the addition of minor species (e.g. H_3^+ and H^-) could greatly change the distribution of major species behind the shock by creating small quanities of free electrons which greatly accelerated the excitation process.

To validate chemical models, flight data does not have enough granularity to effectively determine the accuracy of one model or another. Experimental facilities are a necessary component to develop these models. For entry conditions, these facilities are never capable of measuring the actual probe geometry or even model of probes. The required energy and gas mixture necessary to create a long time duration flow of these conditions would be as extremely costly. Instead, small-time duration experiments such as shock tubes, expansion tubes, or arc jets are used with simplified geometries. Information for these flows can be used to make a meaningful comparison with simulations to validate these chemical models.

The study develops a new QSS model to directly assess the accuracy of CFD rates by comparing to two recent experiments: results from the X-2 expansion tunnel facility at the University of Queensland [107] and an investigation in the electric arc shock tunnel (EAST) [108]. Physically, both these experiments are simpler than real entry flow. The Queensland data measures flow around a simple model and the East data examines only a moving one dimensional shock flow. However, both experiments have enough chemical variation to be useful for validation, indicating that non-equilibrium effects were present with changes in major species occurring over centimeter length scales.

The chapter is organized as follows. Experimental data is reviewed in Section 5.2. Section 5.3 describes the simulation details that reproduce the experiments, the available rates are discussed in Section 5.3.2. Details of the new QSS model are given in Section 5.3.4. The results of the numerical prediction are compared to experiments in Section 5.4:

5.2 Review of Experiments

Two experiments will be considered for this work, both representing recent experimental data in hydrogen helium aerothermochemistry. The data from the Electric Arc Shock Tube (EAST) involves a single shock while the data from the University of Queensland measures radiance from a flow over a capsule

5.2.1 Axisymetric flow from University of Queensland

Measurements at the X-2 facility at the University of Queensland were performed to analyze hydrogen-helium chemistry over a spherical cap [107,109]. The X-2 expansion tube is a free piston driven experimental facility with the capability to add two or more driven tubes. The initial rupture of the diaphragm creates a series of shocks in the expansion section resulting in velocities of 6-12 km s^{-1} in the test chamber. To achieve higher velocities with light gases (H_2 and He), either the percentage of He in the composition needs to be increased or a test gas substituent like neon has to be used. A description of the theoretical and experimental analysis for the substitution process can be found in Refs. [110,111]. This substituent approach is undertaken because gas velocities can reach 18 km s^{-1} in the test chamber by increasing the mole fraction of He, which allows the experimental tests to be closer to the flight enthalpy conditions.

In this study, we compare the simulation results with experiments that were performed with 80 % He and 20 % H_2 by volume. Note that the molar percentage of H_2 in the atmosphere's of Saturn, Jupiter, and Uranus is much higher (over 80% by volume). The freestream conditions used to compare with experimental results are shown in Table 5.1. The test geometry is a 45^o truncated sphere with a curvature radius of 70.7 mm. Radiance is measured along the stagnation line until the edge of the model and along the radial direction 3.2 mm away from the stagnation point. We only simulate the flow over the test object in the chamber and no tunnel effects are incorporated. Experimental images [107] and past work comparing CFD simulations and experiments [112] indicate that a core freestream surrounds the object in the test chamber and tunnel effects are not important for this system.

Major uncertainties in this experiment are the time dependence of the flow and the characterization of the free stream conditions. The experimental results presented represent only one instance in a changing flow. It has been shown [107] that near the stagnation line the integrated radiance still changes by 9.9% over the test time. These transient effects make the selection of the ideal test time for comparisons with steady flow simulations (as are used in Section 5.4.1) difficult. The test time itself is selected using the results of pitot probe measurements and radiance profiles. These pitot tube measurements are further used to characterize the free stream around the model. However, if non-equilibrium effects are present in the pitot tubes themselves, then the analysis of the pitot tube is dependent on the hydrogen chemistry that this work attempts to validate. This leads to a circular dependency, requiring that the chemistry model is accurate to ensure that the characterization of the free stream is accurate.

Table 5.1: Freestream conditions in the simulations.

Density of H_2	$7.07 \cdot 10^{-6}$ kg m^{-3}
Density of He	$5.62 \cdot 10^{-5}$ m^{-3}
Velocity (U)	18.2 km s^{-1}
Flow Temperature (T)	377 K
Wall Temperature (T_w)	300 K

5.2.2 One Dimension Shocks from EAST

In 2014, a series of hydrogen-helium experiments were run at the Electric Arc Shock Tube (EAST) facility [108]. EAST differs from a traditional shock tube in that the driver gas is electrically heated before the diaphragm is burst. This raises the enthalpy of the driver gas and can produce much faster shock waves in the driven gas.

When the shock tube is used, it is assumed that a one dimensional flow is generated in the test section. The one dimensional assumption is always at odds with the boundary layer which forms behind the shock along the test section walls as well as any other disturbances to the shock which result in a fully three dimensional flow. The shock velocity is measured using pressure sensors on the side walls of the driven section to measure the velocity. These measurements are considered accurate to 100 m/s. However, the gas composition at the test region is unknown. Contamination by the driver gas is a known problem as well as additions of trace amounts of air from leaks in the system. The combination of boundary layers and driver gas contamination can increase experimental uncertainties at points significantly behind the shock and can lead to an increased smearing effect throughout the flow.

The specific experiments under investigation used a driven gas mixture of 89% hydrogen 11% helium (by mole) at pressures of the order of one-tenth of a torr. The driven shocks were found to move at velocities between 25 and 28 km/s. Radiative emission was not noted at velocities lower than 25 km/s and 28 km per second was the maximum velocity of interest from that test campaign. This work will focus on two particular shots for that test campaign, which have been designated Shot 18 and Shot 22. These shots were selected because they represent the extremities of the shots in the test campaign while still exhibiting

Table 5.2: Conditions for East data.

Shot Name	Free Stream Number Density	Mole Fraction H_2 to He	Initial Temperature	Shock Speed
Shot 18	$3.2404362 \cdot 10^{21}\ m^{-3}$	89:11	298 K	25.69 km/s
Shot 22	$1.6526225 \cdot 10^{22}\ m^{-3}$	89:11	298 K	27.66 km/s

analyzable radiative signals. Table 5.2 shows the initial conditions of the driven gas, as well as the measured shock speeds. These shots differ both in density and shock speed. Shot 18 represents a weaker shock compared to Shot 22.

5.3 Numerical Methods

The numerical procedure used in this analysis is the current state of the art for complex flows. This is a two-step procedure. First, CFD simulations are used to ascertain the populations of species and the local temperature. Second, a radiative transfer calculation is performed to calculate the excited state populations and the emitted spectrum. A two-step procedure is used because a CFD solution that captures all excited states (a state-to-state model) is prohibitively expensive both in terms of runtime and memory usage. The details of each numerical method are outlined below.

5.3.1 CFD

The aerothermal simulations are performed using the LeMANS solver, a Navier-Stokes solver developed at the University of Michigan specifically for hypersonic applications with thermal and chemical non-equilibrium. It can handle unstructured three-dimensional meshes, and the governing equations are solved using the finite volume method. LeMANS has been benchmarked, verified, and validated over several years [113–115]. LeMANS contains several features and capabilities and only the options relevant to the results presented in this study are discussed below.

LeMANS solves the compressible Navier-Stokes equations (Eqs. 5.1-5.5) that account for n-species, momentum equations, and two-energy equations to include thermal and chemical non-equilibrium. Axi-symmetric solutions are obtained by including the appropriate Jacobian terms for a two-dimensional grid. The two- energy equations are used to solve the total and vibrational energy, respectively [116]. The inviscid and viscous fluxes are split into vectors $\boldsymbol{F}$ and $\boldsymbol{F_v}$, with conserved variables $\boldsymbol{Q}$ and source terms $\boldsymbol{S}_{cv}$. The spatial integration is performed over the inviscid and viscous fluxes using the finite-volume method, and the time integration is performed implicitly using a parallel line-implicit method. Temporal integration is first-order accurate, and spatial integration is second-order accurate.

Species-diffusion fluxes are modeled using modified Fick's law, and momentum fluxes are calculated assuming a Newtonian fluid with Stoke's hypothesis. Conduction heat fluxes are calculated using Fourier's law. Thermal and chemical nonequilibrium is modeled using Park's two-temperature approach [117]. Translational and rotational modes are assumed to be fully excited and in equilibrium with each other. Heat capacity for the internal mode (vibration and electronic) is obtained from NASA polynomial fits [118] using the vibrational-electronic-electron temperature for the curve fit and subtracting the contributions of translational and rotational modes. A detailed discussion of this approach can be found in Ref. [116]. Species thermodynamic data is obtained from NASA polynomial fits [118]. Transport properties (diffusivity, viscosity, and thermal conductivity) are computed from collision integrals [119], where the collision cross sections are fit to the Gupta formulation [120] for heavy species. The most updated cross sections based on ab-initio data for H_2/He system can be found in Ref. [97]. The ion-ion, ion-electron, and electron-electron cross sections are modeled using a shielded Coulomb potential [121]. Mixture transport properties (species diffusion, viscosity, thermal conductivity) are calculated using Wilke's semi-empirical mixing rule. Charged species are treated with a single-fluid approach, and ambipolar diffusion of electrons enforces local quasi-neutrality [122]. Vibrational relaxation is modeled using the Landau-Teller equation [123], where the parameters are obtained from Ref. [97]. The energy transfer between heavy particles and electrons is modeled using the formulation in Ref. [124]. Forward rates for chemical mechanisms follow the modified Arrhenius form: $AT^{\eta}exp(-E/T)$. The temperature is set to the geometric mean of translational and vibrational temperature [117] for all reactions except electron-impact ionization reactions. The backward rates are calculated using the equilibrium constant computed from Gibb's free energy. For electron-impact ionization reactions, vibrational-electronic-electron temperature is used as the controlling temperature. Energy is lost or gained during electron-impact ionization and recombination reactions and the contribution is added or subtracted from the vibrational-electronic-electron energy equation.

$$\frac{\partial \boldsymbol{Q}}{\partial t} + \nabla \cdot (\boldsymbol{F} - \boldsymbol{F_v}) = \boldsymbol{S}_{cv} \tag{5.1}$$

$$\boldsymbol{Q} = \left\{ \begin{array}{c} \rho_1 \\ \vdots \\ \rho_{ns} \\ \rho u \\ \rho v \\ E \\ E_{ve} \end{array} \right\} \quad (5.2) \qquad \boldsymbol{F} = \left\{ \begin{array}{c} \rho_1 u \\ \vdots \\ \rho_{ns} u \\ \rho u^2 + p \\ \rho u v \\ (E+p)u \\ E_{ve} u \end{array} \right\} \quad (5.3) \qquad \boldsymbol{S_{cv}} = \left\{ \begin{array}{c} \dot{\omega}_1 \\ \vdots \\ \dot{\omega}_{ns} \\ 0 \\ 0 \\ 0 \\ \dot{\omega}_{ve} \end{array} \right\} \quad (5.4)$$

$$\boldsymbol{F_v} = \left\{ \begin{array}{c} -J_{x,1} \\ \vdots \\ -J_{x,ns} \\ \tau_{xx} \\ \tau_{xy} \\ \tau_{xx} u + \tau_{xy} v - (q_{tr,x} + q_{ve,x}) - \Sigma(J_{x,s} h_s) \\ -q_{ve,x} - \Sigma(J_{x,s} e_{ve,s}) \end{array} \right\} \qquad (5.5)$$

5.3.2 CFD Chemistry

Different chemical kinetic rate models are evaluated in this study. Previous work [125] has shown that contemporary rate models fall into two categories based on the ionization rates of Hydrogen. This work will use one representative rate model from each category. The rates published in Ref. [126] are referred to as Boyd rates. In Boyd rates, the dissociation rates (reactions 1-4) were obtained from the NIST Chemical Kinetics Database [127], while the rates for the H_2+e^- dissociation reaction and ionization reactions (reactions 7-11) were compiled from McCay and Dexter [128] based on results from Talrose and Karachevtsev [129]. The rates from Ref. [130] are referred to as Higdon rates. Higdon rates are similar to Leibowitz and Kuo [102], with modifications based on curve fits from Gordon and McBride's equilibrium constant data [131]. Later work by Liu et al. [132] has suggested that a modification of the Higdon rate can yield better agreement with experimental measurements of electron number density. They suggested raising all the leading coefficients of the hydrogen ionization reactions by a factor of 25. These rates will be referred to as Modified Higdon rates.

All Arrhenius reaction rate constants from each model can be found in Table 5.3. It is important to note that Higdon et al. [130] also proposed two different rates for both the $H+e^-$ and $He+e^-$ ionization reactions. However, the differences between these rates were found to have a negligible impact on the resulting flowfield obtained in this study. Therefore, only the baseline rates for both of these ionization reactions are included in Table 5.3.

From the rate constants in Table 5.3, we see that rate constants significantly between the Boyd and Higdon rates. The difference is more pronounced for the ionization of H atoms by electrons ($H+e^- \leftrightarrow H^+ + e^- + e^-$). The differences in the dissociation rate is within one order of magnitude (Fig. 5.1a) but four orders of magnitude variation is observed in the ionization reaction (Fig. 5.1b). Erb et al. [96] conducted a detailed investigation of various $H+e^-$ ionization reaction rates, and concluded that uncertainties in the $H+e^-$ ionization rate have a negligible impact on resulting flowfield parameters. However, since entry trajectories into gas giants such as Saturn and Uranus can involve significant thermochemical non-equilibrium, the differences in these rate constants can lead to large variations in the resulting flowfields (Figure 5.4).

Table 5.3: H_2-He mixture reaction rate coefficients. The rates proposed by Higdon et al. [130] have multiple co-efficients for some reactions. All rate co-efficients were analyzed in the comparison study and we found that the results did not vary among the co-efficients. The baselines rates are reported here.

		Rate Constant $[\frac{cm^3}{mol-s}]$		
No.	Reaction	Boyd [126]	Higdon [130]	Modified Higdon [130]
		Dissociation Reactions		
1	$H_2 + H_2 \leftrightarrow H + H + H_2$	$1.096e16T^{-0.251}$ $e^{-51275/T}$	$1.040e19T^{-1.0}$ $e^{-51958/T}$	Unchanged
2	$H_2 + He \leftrightarrow H + H + He$	$1.096e16T^{-0.251}$ $e^{-51275/T}$	$4.170e18T^{-1.0}$ $e^{-51958/T}$	Unchanged
3	$H_2 + H \leftrightarrow H + H + H$	$1.096e16T^{-0.251}$ $e^{-51275/T}$	$8.347e19T^{-1.0}$ $e^{-51958/T}$	Unchanged
4	$H_2 + H^+ \leftrightarrow H + H + H^+$	$1.096e16T^{-0.251}$ $e^{-51275/T}$	$8.347e19T^{-1.0}$ $e^{-51958/T}$	Unchanged
5	$H_2 + e^- \leftrightarrow H + H + e^-$	$1.091e11T^{1.0}$ $e^{-51275/T}$	$8.347e19T^{-1.0}$ $e^{-51958/T}$	Unchanged
6	$H_2 + He^+ \leftrightarrow H + H + He^+$	-	$4.170e18T^{-1.0}$ $e^{-51958/T}$	Unchanged
		Ionization Reactions		
7	$H + H \leftrightarrow H^+ + e^- + H$	$4.216e18T^{-1.0}$ $e^{-157825/T}$	$6.167e10T^{0.5}$ $e^{-116100/T}$	$1.5418e12T^{0.5}$ $e^{-116100/T}$
8	$H + H_2 \leftrightarrow H^+ + e^- + H_2$	$4.216e18T^{-1.0}$ $e^{-157825/T}$	-	-
9	$H + H^+ \leftrightarrow H^+ + e^- + H^+$	$4.216e18T^{-1.0}$ $e^{-157825/T}$	-	-
10	$H + He \leftrightarrow H^+ + e^- + He$	$4.216e18T^{-1.0}$ $e^{-157825/T}$	$4.880e10T^{0.5}$ $e^{-116100/T}$	$1.220e12T^{0.5}$ $e^{-116100/T}$
11	$H + e^- \leftrightarrow H^+ + e^- + e^-$	$3.174e31T^{-3.0}$ $e^{-157825/T}$	$2.282e13T^{0.5}$ $e^{-157800/T}$	$5.705e14T^{0.5}$ $e^{-157800/T}$
12	$He + e^- \leftrightarrow He^+ + e^- + e^-$	-	$1.331e13T^{0.5}$ $e^{-285300/T}$	Unchanged

5.3.3 One Dimensional Shock Flows

To compare against measurements of EAST, a one-dimensional CFD solution was generated. Many times, these flows are approximated as the stagnation line of a blunt body flow [133]. However, to mitigate any possible errors due to wall thermal effects, a one-dimensional free shock calculation is performed. The grid used was a 1 m rectangular stip

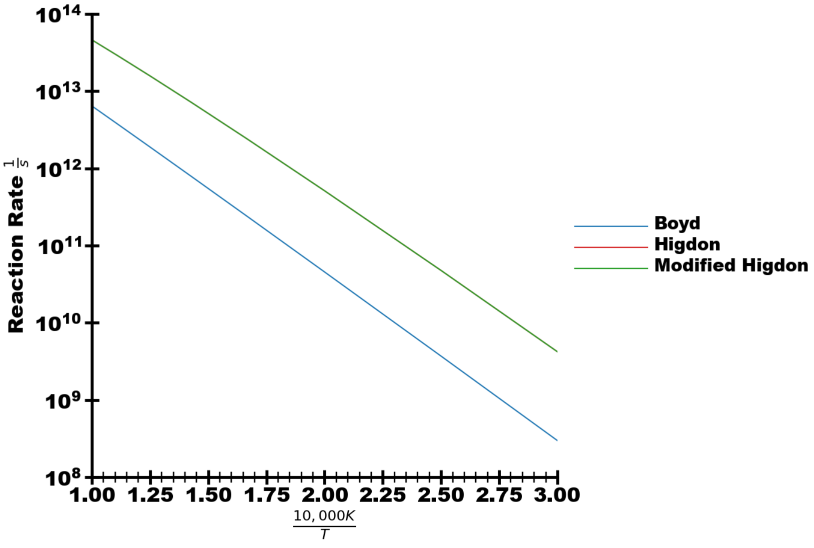

(a) Dissociation Reaction: $H_2 + H \leftrightarrow H + H + H$.

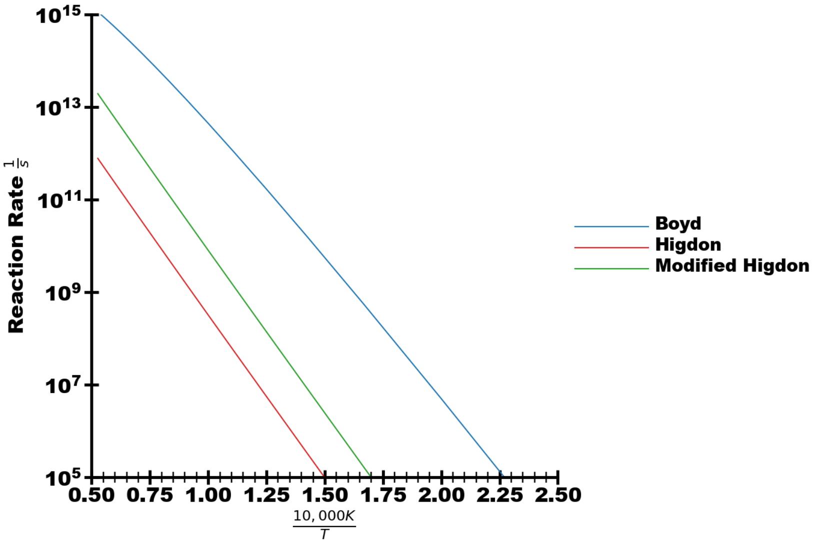

(b) Ionization Reaction: $H + e^- \leftrightarrow H^+ + e^- + e^-$.

Figure 5.1: Rate constants for all four chemistry rates as a function of temperature. Note that the Modified Hidgon chemistry has the same dissociation rate as the orginal Higdon model.

with up to 2000 elements in the x direction, the boundaries in the y direction were all given periodic conditions. The inlet side (x = 0 m) was set to the measured shock speed with density and temperature conditions of the particular EAST shot (see Table 5.1). The outlet (x = 1 m) was given a subsonic pressure outlet condition.

The flow is initialized with a Rankine Hugoniot condition using the flow chemistry of the supersonic side. For high flow speeds, it was found that doubling the subsonic density lead to faster convergence.

Because the flow is initialized to only the approximate shock conditions and there is no physical mechanism to hold the shock in place, a control system was implemented into LeMANS to reduce the shock velocity to zero.

5.3.3.1 Shock Control Derivation

Consider a supersonic normal shock flow with a moving shock. The velocity, pressure and density on the supersonic side are denoted u_1, P_1, and ρ_1 respectively. The same variables are subscripted 2 on the subsonic side. The shock is moving with velocity v_s.

Let the ˆ denote variables transformed to the shock frame. That is, $\hat{u}_1 = u_1 + v_s$ is the flow velocity of the shock. In this frame, the shock is not moving and the normal shock relations hold. Mass, momentum, and energy flow is constant.

$$\rho_1 \hat{u}_1 = \rho_2 \hat{u}_2 \tag{5.6}$$

$$\rho_1 \hat{u}_1^2 + P_1 = \rho_2 \hat{u}_2^2 + P_2 \tag{5.7}$$

$$h_1 + \frac{1}{2}\hat{u}_1^2 = h_2 + \frac{1}{2}\hat{u}_2^2 \tag{5.8}$$

where h is the enthalpy. Consider another normal shock flow with the same supersonic conditions, but with a different shock speed. Let a prime ($'$) denote the conditions of this flow e.g. $\hat{u}_1' = u_1 + v_s'$ where v_s' is the new shock speed. These shock relations are then

$$\rho_1 \hat{u}_1' = \rho_2' \hat{u}_2' \tag{5.9}$$

$$\rho_1 \hat{u}_1'^2 + P_1 = \rho_2' \hat{u}_2'^2 + P_2' \tag{5.10}$$

$$h_1 + \frac{1}{2} \hat{u}_1'^2 = h_2' + \frac{1}{2}' \hat{u}_2'^2 \tag{5.11}$$

The prime conditions are considered as the target conditions. The object is to find ρ_2' in terms of the unprimed conditions and new shock speed. The new shock speed is encoded in $\hat{u}_1'$. One begins by subtracting the two energy equations (Equations 5.8 and 5.11), canceling the supersonic enthalpy.

$$\frac{1}{2}(\hat{u}_1^2 - \hat{u}_1'^2) = h_2 - h_2' + \frac{1}{2}(\hat{u}_2^2 - \hat{u}_2'^2) \tag{5.12}$$

Because this analysis concerns a hypersonic flow, thermally perfect gas assumptions are not valid. The subsonic internal energy is divided into a translation component and an internal component. It is assumed that the translational component is thermally perfect.

$$h_2 = C_v T + RT + e_{int} \tag{5.13}$$

where C_v is the translational heat capacity, R is the gas constant, T is the translational temperature, and e_{int} is the internal energy of the gas. This can be reduced by defining a constant pressure translational heat capacity.

$$C_p = C_v + R \tag{5.14}$$

such that Equation 5.13 reduces to

$$h_2 = C_p T + e_{int} \tag{5.15}$$

Substituting Equation 5.15 into Equation 5.12

$$\frac{1}{2}(\hat{u}_1^2 - \hat{u}_1^{'2}) = C_p(T - T') + e_{int} - e_{int,2} + \frac{1}{2}(\hat{u}_2^2 - \hat{u}_2^{'2}) \tag{5.16}$$

It is now assumed that any control process only slightly changes the “2” state. Thus, the change in internal energy is negligible.

$$\frac{1}{2}(\hat{u}_1^2 - \hat{u}_1^{'2}) = C_p(T - T') + \frac{1}{2}\hat{u}_2^2 - \frac{1}{2}\hat{u}_2^{'2} \tag{5.17}$$

Using the primed equation of mass conservation (Equation 5.9)

$$\rho_1 \hat{u}_1' = \rho_2' \hat{u}_2' \rightarrow \hat{u}_2' = \frac{\rho_1 \hat{u}_1'}{\rho_2'} \tag{5.18}$$

and the similar equation for the unprimed system (Equation 5.6)

$$\rho_1 \hat{u}_1 = \rho_2 \hat{u}_2 \rightarrow \hat{u}_2 = \frac{\rho_1 \hat{u}_1'}{\rho_2} \tag{5.19}$$

One can substitute into the equation 5.17

$$\frac{1}{2}(\hat{u}_1^2 - \hat{u}_1'^2) = C_p(T_2 - T_2') + \frac{\rho_1^2 \hat{u}_1'^2}{2\rho_2^2} - \frac{\rho_1^2 \hat{u}_1'^2}{2\rho_2'^2} \tag{5.20}$$

The momentum equations (Equations 5.7) 5.10) can also be transformed by the ideal gas law ($\frac{P}{\rho} = RT$), as well as the substitutions above (Equations 5.19 and 5.18)

$$\rho_1 \hat{u}_1^2 + \rho_1 RT_1 = \frac{\rho_1^2 \hat{u}_1^2}{\rho_2} + \rho_2 RT_2 \rho_1 \hat{u}_1'^2 + \rho_1 RT_1 = \frac{\rho_1^2 \hat{u}_1'^2}{\rho_2'} + \rho_2' RT_2' \tag{5.21}$$

$$\frac{\rho_1 \hat{u}_1^2}{\rho_2 R} + \frac{\rho_1 T_1}{\rho_2} - \frac{\rho_1^2 \hat{u}_1^2}{\rho_2^2 R} = T_2 \frac{\rho_1 \hat{u}_1'^2}{\rho_2' R} + \frac{\rho_1 T_1}{\rho_2'} - \frac{\rho_1^2 \hat{u}_1'^2}{\rho_2'^2 R} + T_2' \tag{5.22}$$

Equations 5.21 and 5.22 can be substituted into Equation 5.20.

$$\begin{aligned}\frac{\rho_1}{2}(\hat{u}_1^2 - \hat{u}_1'^2) =& \frac{C_p \rho_1 \hat{u}_1^2}{\rho_2 R} + \frac{C_p \rho_1 T_1}{\rho_2} - \frac{C_p \rho_1^2 \hat{u}_1^2}{\rho_2^2 R} - \frac{C_p \rho_1 \hat{u}_1'^2}{\rho_2' R} \\ & - \frac{C_p \rho_1 T_1}{\rho_2'} + \frac{C_p \rho_1^2 \hat{u}_1'^2}{\rho_2'^2 R} + \frac{\rho_1^2 \hat{u}_1'^2}{2\rho_2^2} - \frac{\rho_1^2 \hat{u}_1'^2}{2\rho_2'^2}\end{aligned} \tag{5.23}$$

$$\begin{aligned}\frac{\rho_2^2 \rho_2'^2}{2}(\hat{u}_1^2 - \hat{u}_1'^2) =& \frac{C_p \rho_2 \rho_2'^2 \rho_1 \hat{u}_1^2}{R} + \frac{C_p \rho_1 \rho_2^2 \rho_2'^2 RT_1}{R} - \frac{C_p \rho_1^2 \rho_2'^2 \hat{u}_1^2}{R} - \frac{C_p \rho_1 \rho_2^2 \rho_2' \hat{u}_1'^2}{R} \\ & - \frac{C_p \rho_1 \rho_2^2 \rho_2' RT_1}{R} + \frac{C_p \rho_1^2 \rho_2^2 \hat{u}_1'^2}{R} + \frac{1}{2} \rho_1^2 \rho_2'^2 \hat{u}_1'^2 \\ & - \frac{1}{2} \rho_1^2 \rho_2^2 \hat{u}_1'^2\end{aligned} \tag{5.24}$$

$$\begin{aligned}0 = \rho_2'^2 & \left[-\frac{\rho_2^2}{2}(\hat{u}_1^2 - \hat{u}_1'^2) + \frac{C_p}{R} \rho_2 \rho_1 \hat{u}_1^2 + C_p \rho_1 \rho_2^2 T_1 - \frac{C_p}{R} \rho_1^2 \hat{u}_1^2 + \frac{1}{2} \rho_1^2 \hat{u}_1'^2 \right] \\ + \rho_2' & \left[-\frac{C_p}{R} \rho_1 \rho_2^2 \hat{u}_1'^2 - C_p \rho_1 \rho_2^2 T_1 \right] \\ + & \left[\frac{C_p}{R} \rho_1^2 \rho_2^2 \hat{u}_1'^2 - \frac{1}{2} \rho_1^2 \rho_2^2 \hat{u}_1'^2 \right]\end{aligned} \tag{5.25}$$

Equation 5.25 is a quadratic equation. The positive root is the only valid solution.

5.3.3.2 Application

In Section 5.3.3.1, equations were derived to determine a new post-shock density base on freestream conditions, the original post-shock density, and the change in shock speed desired. Without this quantity, one cannot know how much density to add to a flow to adjust the shock velocity. Guesswork usually leads to a shock whose velocity does change or to a number of negative energy solutions.

However, the calculation of this new density to a real flow is not straightforward. In a real CDF solver, two conditions that are assumed in section 5.3.3.1 do not hold: post-shock momentum and density are not constant, and momentum is not necessarily conserved across the shock. This is because all supersonic CFD solvers iterate in time, and error in the momentum is considered a time-dependent acoustic disturbance.

Applying shock control to a converging solution is nontrivial. In this study, the shock velocity is measured directly. The post-shock density is best approximated by finding the minimum post-shock velocity. One can estimate a post-shock density as

$$\rho_2^* = \frac{\rho_1 u_1}{u_{2,min}} \tag{5.26}$$

Using ρ_2^* as ρ_2 in 5.25 one can solve for $\rho_2'^2$ and then develop a density ratio

$$\nu_\rho = \frac{\rho_2'^2}{\rho_2^*} \tag{5.27}$$

Multiplying all species densities in the subsonic cells by ν_ρ sets the new subsonic densities.

The new momentum is also set by a ratio,

$$\nu_{\mathbf{P}} = \frac{\rho_1 u_1 + \rho_1 \Delta v_s}{\rho_1 u_1} \tag{5.28}$$

where Δv_s is the change in shock speed. The translational temperature, however, is adjusted additively as

$$\nu_{\mathbf{T}} = v_{s,1}\frac{1}{R}(\frac{\rho_1}{\rho_2^*}+1)\frac{\rho_1}{\rho_2^*} - v_{s,2}\frac{1}{R}(\frac{\rho_1}{\rho_2'}+1)\frac{\rho_1}{\rho_2'} + T_1(\frac{\rho_1}{\rho_2^*}-\frac{\rho_1}{\rho_2'}) \tag{5.29}$$

Applying these state changes to a 1D shock flow can change the shock speed. However, due to the convergence that is happing coincidently, it has been found that repeated small applications of these equations with small changed in shock speed yields the most stable flows. For the flows discussed in this work, a length scale is determined, usually about 0.25 cm. The shock is allowed to move four times this length scale. Afterward, every time that the shock cross another integer multiple of the length scale, the shock speed is set to be

$$v_{s,2} = (0.5^n - 0.05n)v_{s,1} \tag{5.30}$$

where $v_{s,2}$ is the new shock velocity, $v_{s,1}$ is the current measured shock velocity as measured by the time required to reach the current control point from the last one, and n is the current number of control steps that have been applied. This usually leads to a convergence where the shock moves into the subsonic region (because the Rankine Huguniot condition underpredicts the post-shock density) which is slowed down by density additions, once the shock remains stationary relative to the control length scale for a flow-through time, the solution is considered converged. A perfectly stationary shock is impossible to achieve. However, the shock speed is kept less than one percent of the free stream velocity, which is approximately the error in the measured shock speed in the EAST facility.

5.3.4 Radiative Heat Transfer

Radiative Heat transfer is calculated using NEQAIR v.15.0. NEQAIR, takes the number densities, translational, rotational, vibrational, and electronic temperatures along a line of sight to calculate the populations of excited species. It then computes the spectra in the wavelength region (or regions) of interest using a line-by-line radiation solver. NEQAIR also includes the ability to calculate convolved spectra using the measured convolution functions of the experimental equipment.

For the H_2/He system, a combination of Boltzmann and quasi-steady state (QSS) models are used for the NEQAIR calculations. The excited states of helium and its ions always are calculated with an assumed Boltzmann distribution, while the hydrogen molecule and atom are calculated using Boltzmann or QSS methods.

Helium acts as an inert substituent. This can be seen by calculating the population ratio between the $1s^2$ state and the $1s3p$ configuration. The $1s3p$ to $1s2s$ transition is the strongest helium line at 501 nm. However, the ratio of $1s3p$ to ground state is approximately $5 \cdot 10^{-}6$ in a Boltzmann distribution at 20000 K (Change of energy being 23 eV with a degeneracy of 3). The Einstein coefficient is given as $1.3372 \cdot 10^7 s^{-1}$ [134]. The emitted power per steradian is then approximately

$$I = \frac{hc}{\lambda} n_{He} A = 3.965 \cdot 10^{-19} J \cdot 3.2404362 \cdot 10^{21} m^{-3} \cdot 0.2 \cdot 5 \cdot 10^{-}6 \cdot 1.3372 \cdot 10^{7} s^{-1} = 17181 \frac{W}{m^3 sr} \tag{5.31}$$

Assuming that the object of interest has a length scale of 10 cm. This yields an approximate intensity of $0.0017181 W cm^{-2} sr^{-}1$. The experimental measurements under consideration are only sensitive to $0.1 W cm^{-2} sr^{-}1$. Therefore, it is unlikely that any helium radiation will be measured. Using only the Boltzmann assumption for He does not affect the accuracy of the computed radiance with respect to those measurements.

The hydrogen atom and molecule each require a set of rate data for each state which is compiled from a number of sources.

5.3.4.1 Hydrogen Atom

NEQAIR's method for atomic QSS modeling requires a set of state energies and degeneracies as well as electron impact excitation rate data. The states of hydrogen are binned by principal quantum numbers and neglect the faint splitting by angular momentum. State energies are taken from the NIST atomic database [135] up to the eleventh excited state. The twelfth excited state ($n = 13$) and above all varying in energy by less than a tenth of an electron volt, and their relative populations are small. They are simply equilibrated to the $n = 12$ state.

The database also includes electron impact excitation rates for the ground state to an excited state, but no rates for changes between excited states. There are few complete sets of electron impact excitation rate data available that are suited for hypersonic flow.

Aggarwal [136] created a low temperature set which is complete in all but a few transitions (the $n = 2$ to $n = 3$ rate for example). Park [137] also published a complete set in the early 1970's by averaging over many of the theories available at the time.

This work will focus on the electron transition emission from the second to the first excited state of atomic hydrogen ($n = 3$ and $n = 2$). This line also called Balmer - α, lies in the visible range, and is a relatively isolated spectral line, making it easy to measure experimentally. In the QSS model, the number densities of excited states are constant. The radiative emission is principally balanced by electron impact excitation into the excited states. (These states are also generated by emission from a more excited state.) Figure 5.2 plots the excitation rates for the ground to first excited state from sources including the NIST database. The ground to second excited state rates are plotted in Figure 5.3. Park's and Aggarwal's are remarkably consistent, and both are an order of magnitude faster than the NIST estimates. Because they are the most modern complete set, the Aggarwal excitation rate data was used. The missing state changes were then supplemented with Park's estimates.

5.3.4.2 Molecular Hydrogen

Molecular hydrogen requires rate data between each electronically excited state, between the initial and final vibrational levels, as well as rate data for processes which convert a particular state into a different chemical (e.g. electron impact dissociation, ionization, etc.) species. The inter-state transitions are described by a set of Frank-Condon factors, electron impact excitation rates (which are independent of vibrational state), and radiative Einstein coefficients. The Franck-Condon factors and Einstein coefficients are taken from the work

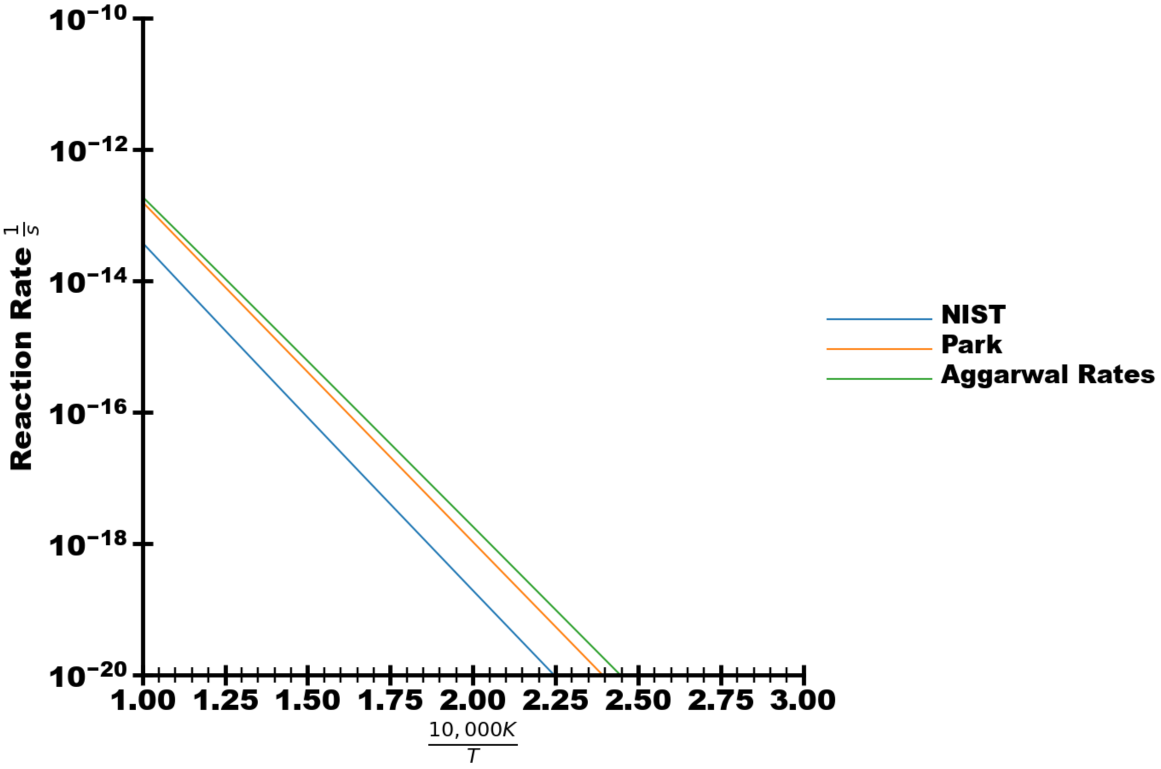

Figure 5.2: Rates for the $n = 1$ to $n = 2$ excitation of atomic hydrogen compiled from several sources.

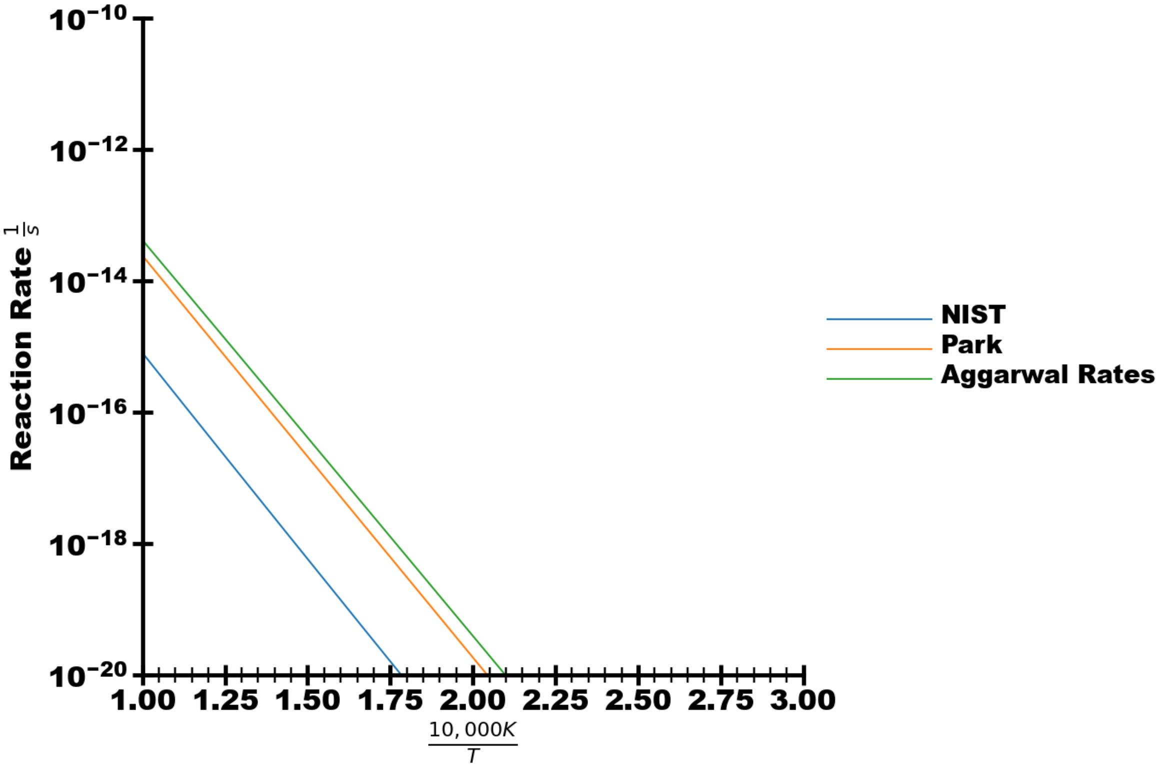

Figure 5.3: Rates for the $n = 1$ to $n = 3$ excitation of atomic hydrogen compiled from several sources.

of Fantz and Wünderlich [138]. Electron impact excitation rates are taken from Kim [139].

Frank Condon Factors [140,141] are the nuclear overlap of two molecular states of different electron excitations. If a molecule experiences an electronic transition, the vibrational level will also change. The likelihood of entering a particular vibrational level is proportional to the Frank Condon factor. Because the vibrational state still contains some energy, the photon emission from the electron transitions is broadened by the energy of the vibrational levels.

The Einstein coefficients are values that determine the probability of transition in time. There are two coefficients. The "A_{ij}" coefficient is the rate of spontaneous transition from state i to state j. The "B_{ij}" coefficient relates the probability that an atom or molecule transitions due to an external field. These can be used to determine, for example, the absorption coefficient (or spectral opacity). For this work, only the A_{ij} is used.

The QSS calculation also accounts for other changes to the hydrogen molecule. Electron dissociation cross sections were taken from Yoon [142]. Nondissociative ionization cross sections were found in Jacobsen [143]. Wedding and Phelps [144] determined quenching rates for the $c^3\Pi_u^-$ and $a^3\Sigma_g^+$ states, which were included. However, experimental quenching data is sparse for other states and represents one of the largest uncertainties of the QSS model.

5.4 Results

5.4.1 Queensland Data

Three axisymmetric simulations are performed using LeMANS with different chemical rates. Based on previous work [125], a one-temperature model was used without significant loss of accuracy. Contours of temperature are shown in Figure 5.4. Temperatures extracted from the stagnation line are plotted on Figure 5.7. Densities along the stagnation line are shown in Figure 5.5, and Figure 5.6 shows the electron number densities along the stagnation line all plotted on the same axis. The notable difference between the chemical models is the electron density as a function of position as well as the significantly different temperature profiles.

The Boyd rates ionize hydrogen at a much faster rate. This creates several points of contrast against the Higdon model. First, the electron density per the Boyd model almost matches the atomic hydrogen density and the ionized hydrogen density. The energy that is used to ionize hydrogen is removed from translational modes, this reduces the shock strength and decreases the shock stand-off distance. Meanwhile, the Higdon model ionizes slowly, increasing the shock strength and standoff distance. The Modified Higdon rates predict temperatures which lie between the other two models. The total variation in shock standoff distance is approximately 5 cm.

From each contour, a series of 100 lines of sight (LOS) are extracted from the contour normal to the flow direction (See Figure 5.8). These LOS contain density and temperature information used by NEQAIR. For those lines extracted ahead of the model, the LOS is copied and appended in reverse to the original line to represent the entire flow. The model itself is taken to be a cold black body. NEQAIR performs calculations on each of the lines of sight, outputting a spectrum representing the emission at the end of the LOS. This spectrum is spectrally convolved with the known properties of the instruments used at the Queensland facility. This is taken as a Voigt profile with a Half-Width Half Value (HWHV) of 9.7 Åand Lorentzian HWHV of 4.7 Å. A spatial convolution over these LOS is also performed. The convolution parameters are determined based on the experimental measurement of a light source placed behind the model. When the camera is placed behind the model it measures some intensity. The change in intensity with position is equal to the convolution function. Figure 5.9 shows both the measurements as well as the fitted Voigt profile of HWHVs of 0.10868 mm and 0.032507 mm.

Figures 5.10 and 5.11 show the spectral radiance contour using the Higdon chemistry and Boltzmann excited states before and after the spatial convolution. The convolution blurs the change of radiance at the shock as well as the shadow of the model at ($x = 0$). Six such convolved contours are generated for three chemical models and the two excited state models.

Integrating these contours over specific wavelengths can produce radiance curves that can be directly compared to experimental measurement of radiance along the stagnation line. Figure 5.12 and Figure 5.13 show the α emission in natural and log scale respectively. This is calculated by integrating the spectral radiance over the wavelengths between 476 and 497 nm. Likewise, the β emission (640 to 670 nm) is plotted in Figures 5.15 and 5.16. The α and β regions are the locations of the spectral lines of hydrogen transitions from the first excited electronic state to ground, and from the second excited state to ground respectively.

The predicted radiance is highly dependent on both the CFD chemistry and the excited state model. The most apparent trend is that the Boltzmann assumption consistently predicts a higher radiance than the QSS calculation. The relative difference between the Boltzmann and QSS methods is a measure of the degree of non-equilibrium in the flow. In an equilibrium flow, the Boltzmann and QSS methods should tend to similar excited state populations.

Given these spectral ranges, equilibrium specifically refers to the equilibrium of the hydrogen electronic states compared to the electron state. The QSS model only calculates the hydrogen excitation via electron impact. In order for the hydrogen excited states to match the Boltzmann distribution, electrons must be present in sufficient density and energy to excite the mode at the rate of its spontaneous emission.

With this in mind, these results suggest that the Boyd model predicts the least amount of non-equilibrium in the flow. The greatest non-equilibrium is predicted using Higdon or Modified Higdon chemistry depending on location. This is consistent with the difference in ionization rates between the models. The Boyd model, being the fastest in ionization appears closest to equilibrium conditions. Higdon chemistry, being the slowest ionizing model appears to be nearer equilibrium near the shock where there are no electrons, but dissociation has completed. The Modified Higdon rates have enough electrons that the chemical nonequilibrium is most observable. Near the wall, however, the Higdon rates have produced an appreciable electron density which is placed in new equilibrium by the translational cooling near the wall. It is stressed that no flow chemistry produces a distribution that is consistent with a Boltzmann distribution. Therefore, the use of a Boltzmann distribution model for excited states is inaccurate. For the remainder of this section, all discussion pertains only to the QSS results which are considered more accurate.

No combination of models appears to accurately capture the experimental results. The most striking property of the measurements is the rise in radiance toward the model. This trend is only captured using the Modified Higdon chemistry. However, the predicted intensity is approximately an order of magnitude lower. The relative rise in intensity between the fore and aft positions along the stagnation line is not as great as that measured as well.

The success of the Modified Higdon rates is a result of two effects. First, the thermal energy that supported the high emission of the Higdon model near the shock is reduced by ionization. Secondly, as these electrons remain present in the flow they can excite more atomic hydrogen near the wall. The two relatively simple effects combine to have a dramatic effect on the overall shape of the measured radiance.

Accurate modeling of the flow chemistry and excited states significantly impacts the total radiative heat transfer to the model. Figure 5.17 shows an estimated radiative heat transfer to the stagnation point. This is done by extracting the stagnation line from all CFD results and calculating the total heat transfer along that line using NEQAIR. The resulting intensity is multiplied by π to estimate a total heat flux to the surface area. This assumes that the flow field is approximately spherically symmetric about the stagnation line. This is not a perfect assumption, however, the solid angles where this does not hold are at low incident angles to the stagnation point and do not significantly contribute to the total heat flux.

Figure 5.17 shows that the total radiative heat flux changes by an order of magnitude depending on the chemistry and excitation models. The overprediction of the Boltzmann model is evident throughout. Furthermore, the difference in non-equilibrium between the chemical models, as shown by the relative difference between the Boltzmann and QSS models, is consistent with the spectral analysis above. This reinforces that the accurate radiative modeling of these flows can be critical for missions to the outer gas giants, especially the design of thermal protection systems.

5.4.2 EAST Data

Using the one-dimensional shock methods discussed in Section 5.3.3, six CFD solutions are generated: three chemical kinetic models for each of the two shots. Figure 5.18 shows the number densities for the Shot 18 case and Figure 5.19 shows the same data for the Shot 22 case. The number densities of the electrons are compared in Figures 5.22 and 5.23. As expected, the electron densities of the Boyd rates are highest, and the Higdon chemistry predicts the lowest electron density.

The data from EAST consists of 4 spectral images taken at different wavelength bands. Contours of this data are shown in Figures 5.24 and 5.25. The narrow region at 650 nm represents a high-resolution image of the hygdron atomic emission from the second excited state to ground, called the β emission in the Queensland experiments. These bands, in increasing wavelength, are referred to as the vacuum ultraviolet (VUV), the blue, the red, and infrared (IR) bands. Three comparisons are made between the data. Integrated radiance from each wavelength band is plotted against position. The spectral radiance is integrated over the 2 cm behind the shock and plotted as a function of wavelength. Lastly, the same integrated spectrum is shown for the red region alone.

Figure 5.28 plots the radiance curves of Shot 22 with respect to positions for the Higdon rates with both Boltzmann and QSS settings. These curves show the expected variation that the Boltzmann method predicts a much higher radiance. Figures 5.26 and 5.27 show

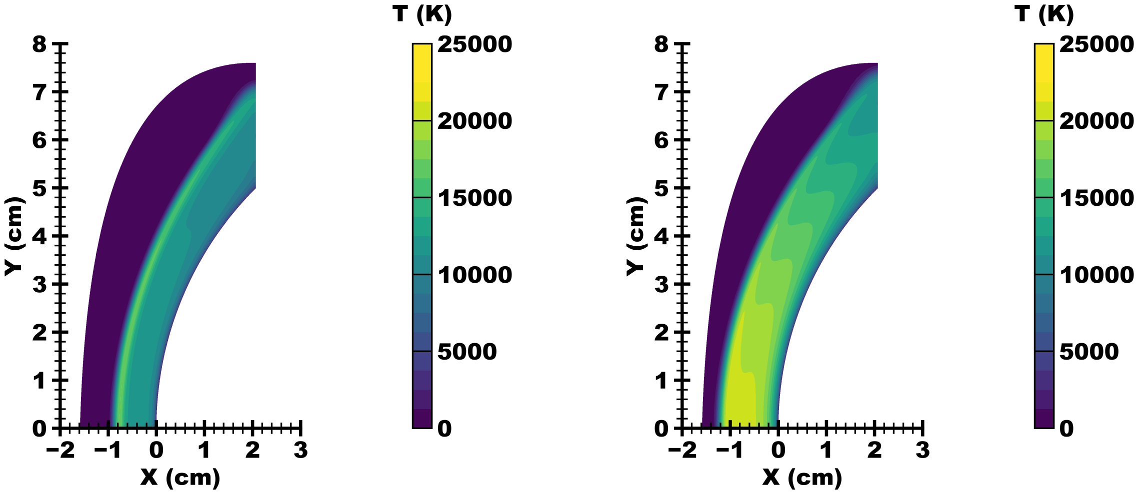

(a) Boyd Chemistry

(b) Higdon Chemistry

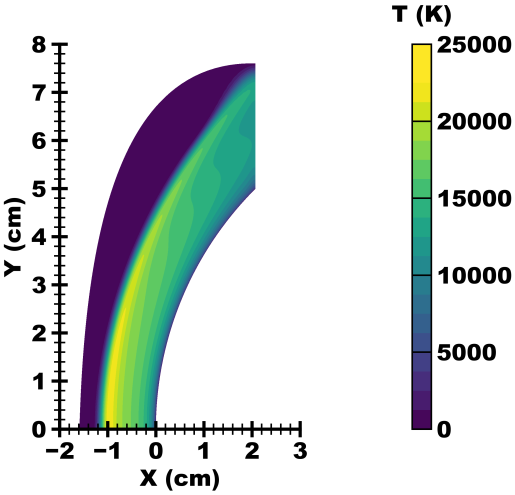

(c) Modified Higdon Chemistry

Figure 5.4: Temperature contours of flow around model in Queensland experiment

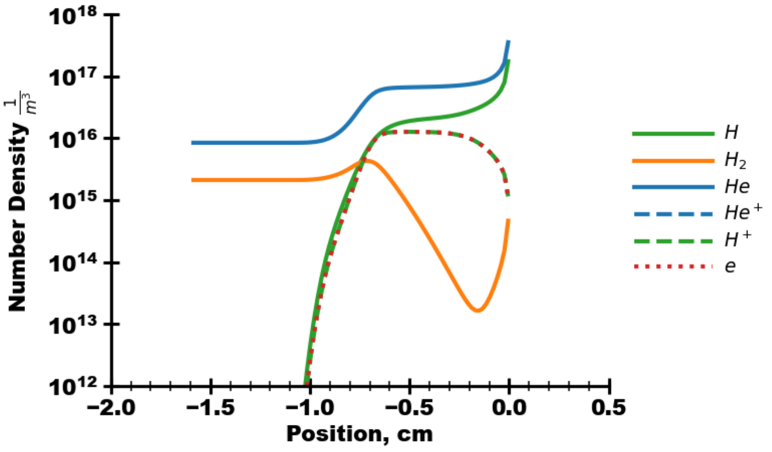

(a) Boyd Chemistry

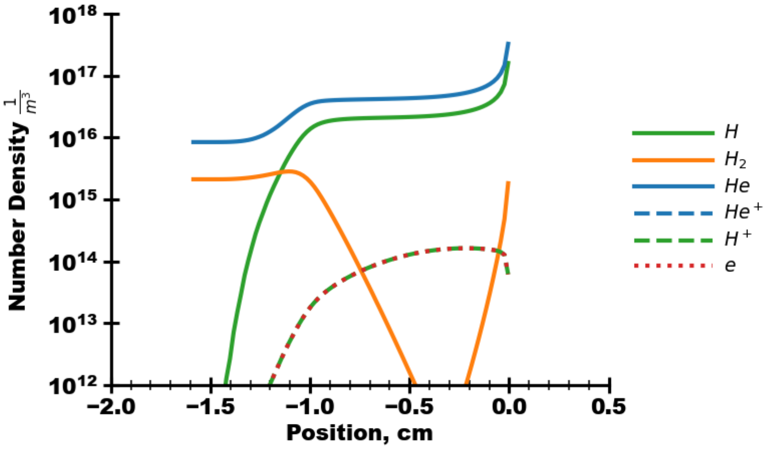

(b) Higdon Chemistry

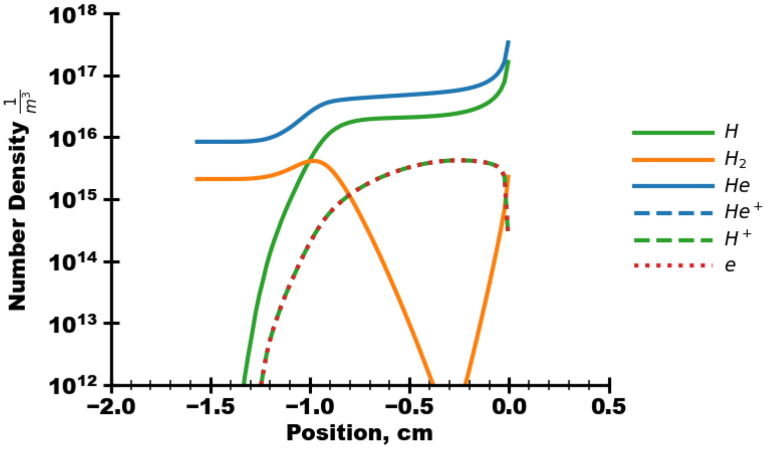

(c) Modified Higdon Chemistry

Figure 5.5: Species densities along stagnation line of flow in Queensland experiment

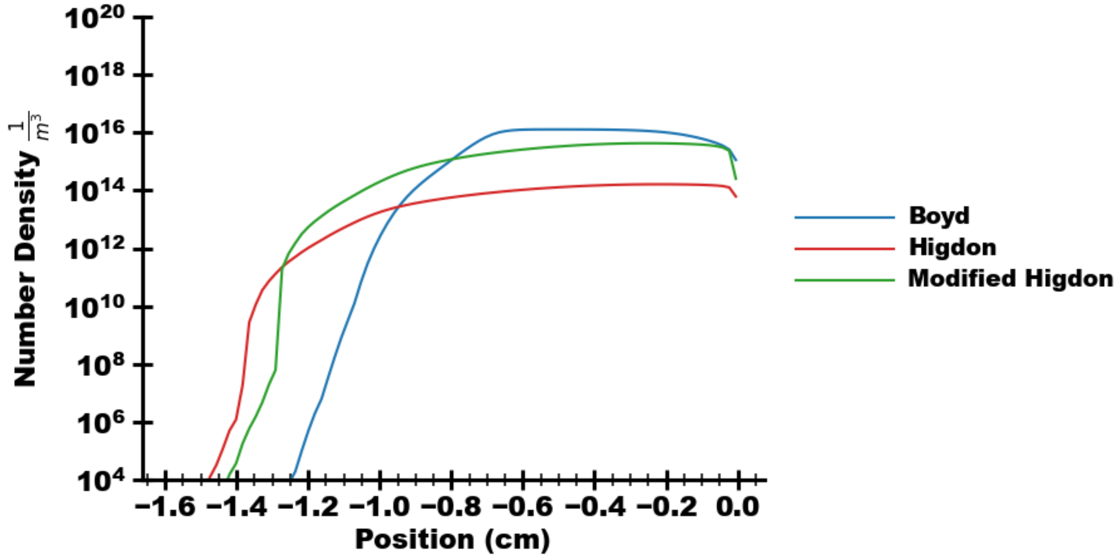

Figure 5.6: Electron number densities along stagnation line

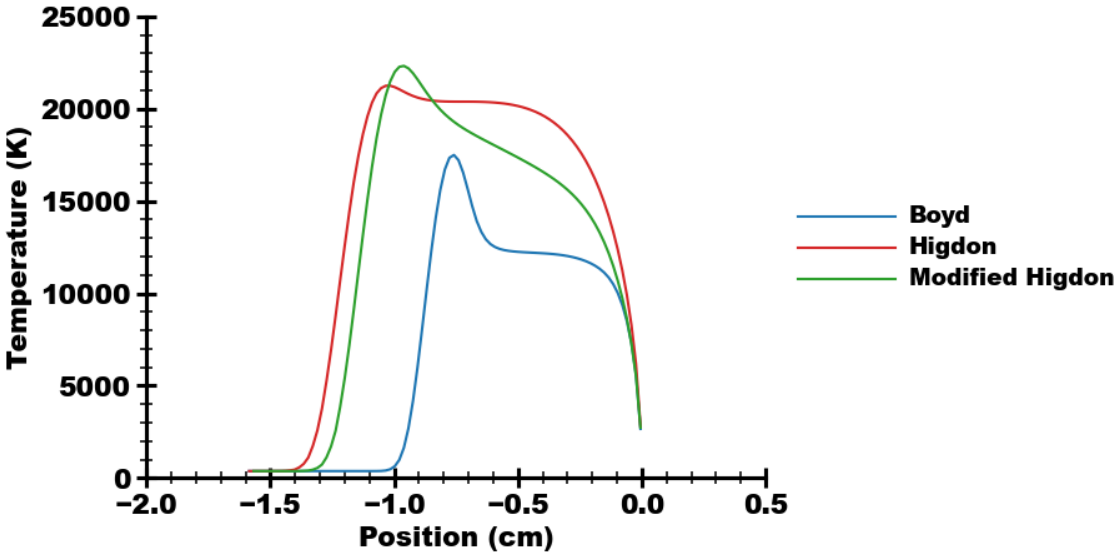

Figure 5.7: Temperatures along stagnation line

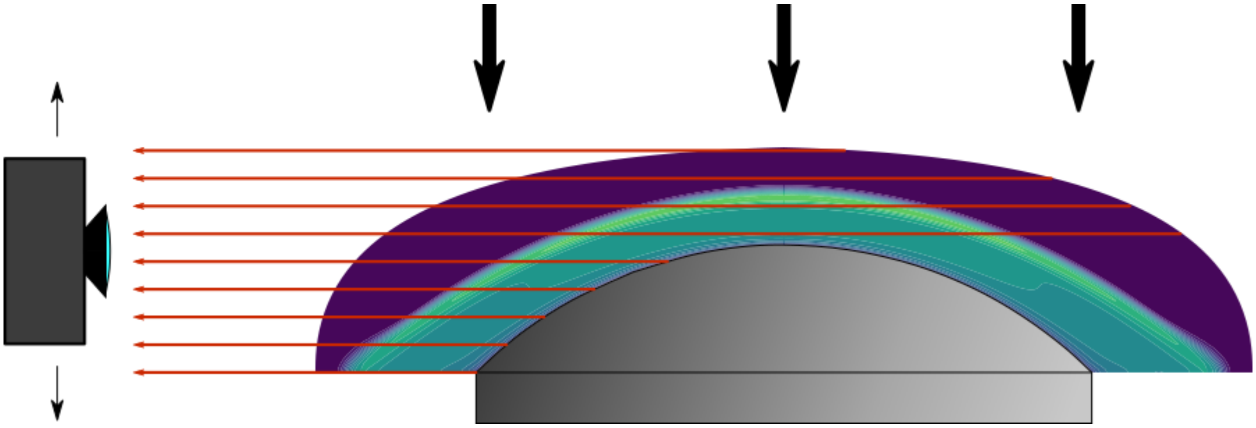

Figure 5.8: Overhead diagram of extracted lines of sight (LOS) used to predict the spatially resolved spectral radiance. The flow enters from above and impinges on the model. The predicted flow temperature contours are plotted, identical to the results in Figure 5.4a. Lines of sight are extracted normal to the flow towards the camera. The shadowing of the model is included. The camera convolution function is shown in figure 5.9. Although only nine lines are shown, 100 lines of sight are extracted.

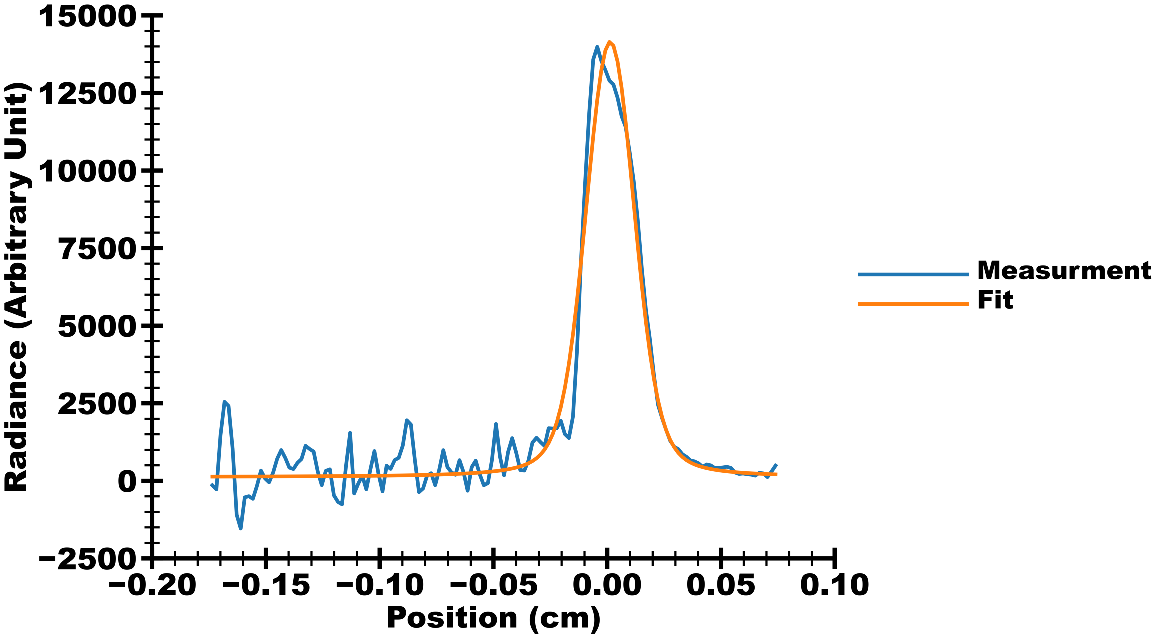

Figure 5.9: Spatial Convulation function for radiance calulations based on experimental measuments. The resultant fit is a Voigt profile with a Gausian Half Width Half Value (HWHV) of 0.10868 mm and a Lorentizan HWHV of 0.032507 mm.

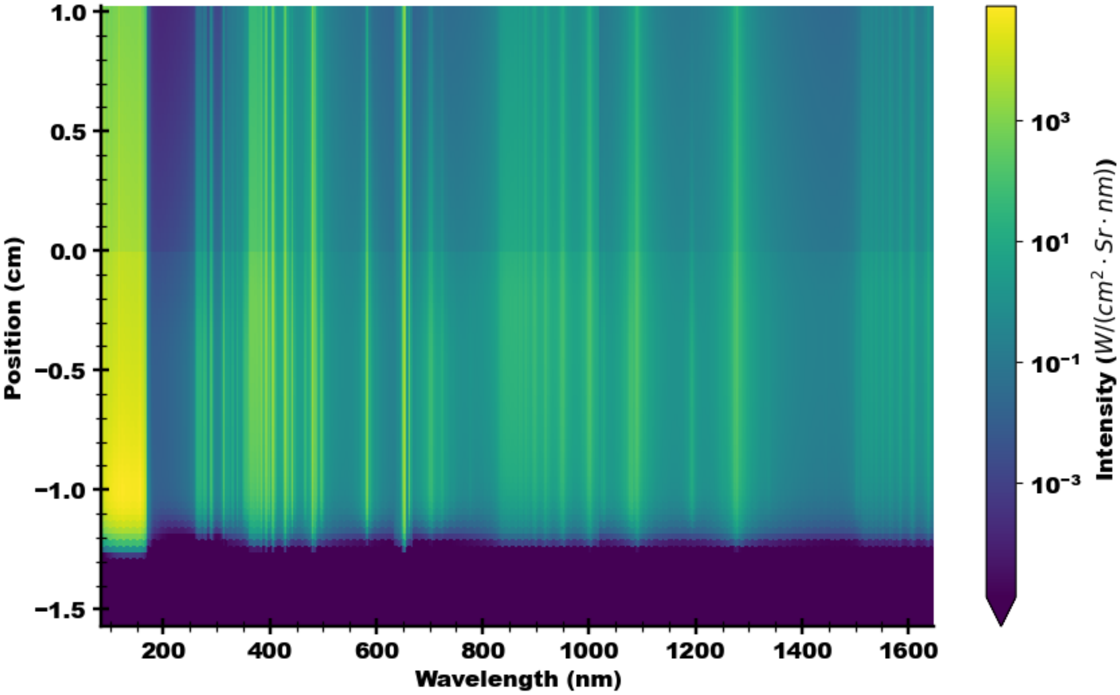

Figure 5.10: Spatial and spectral contour on the prediced spetral radiance of the Queesnland experiment using Higdon chemiry and Boltman excited states. No convolution is performed

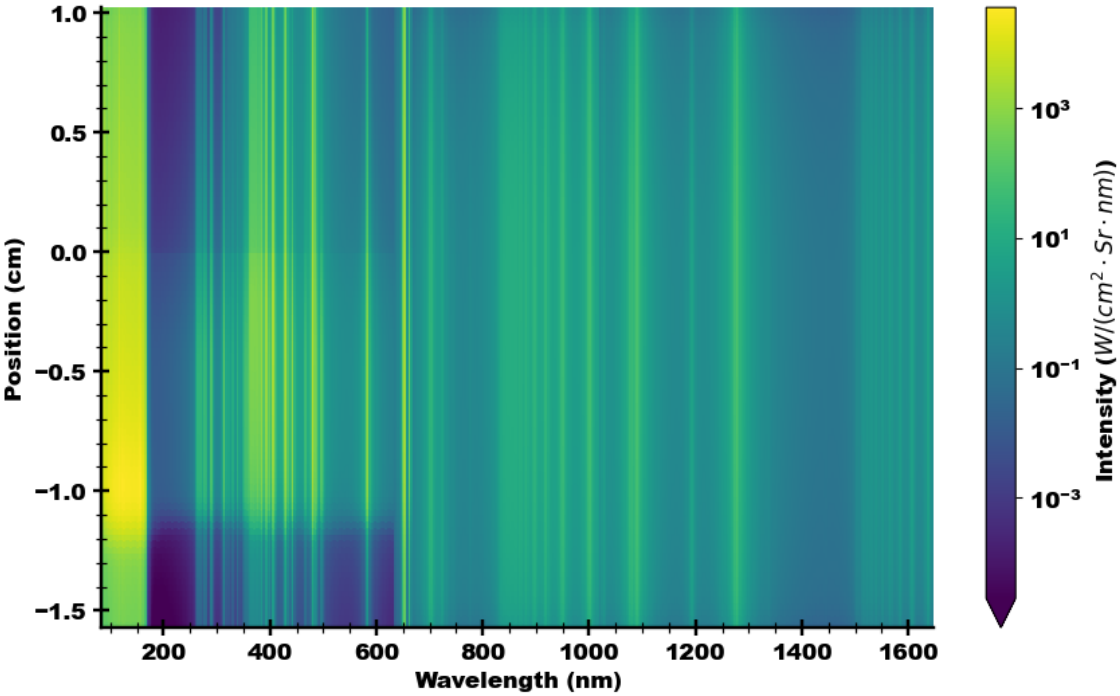

Figure 5.11: Same as Figure 5.10, however the spatial convolution from Figure 5.9 is performed.

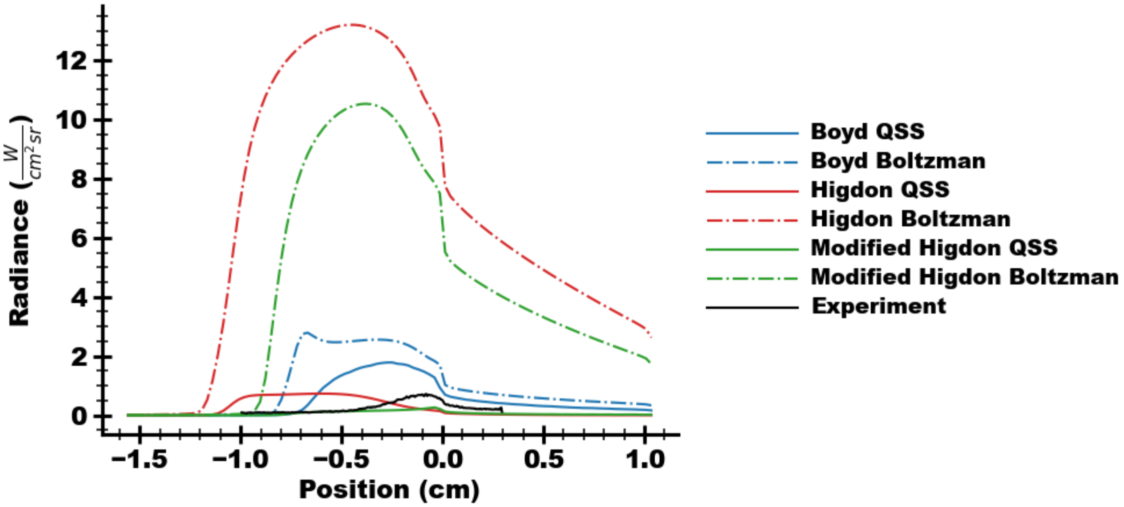

Figure 5.12: Radiance profiles measured along stagnation steamline with instrument convolution, intensity is averages around the $H\alpha$ band $(476nm - 497nm)$. Measurements place the shock at $-1.185cm$.

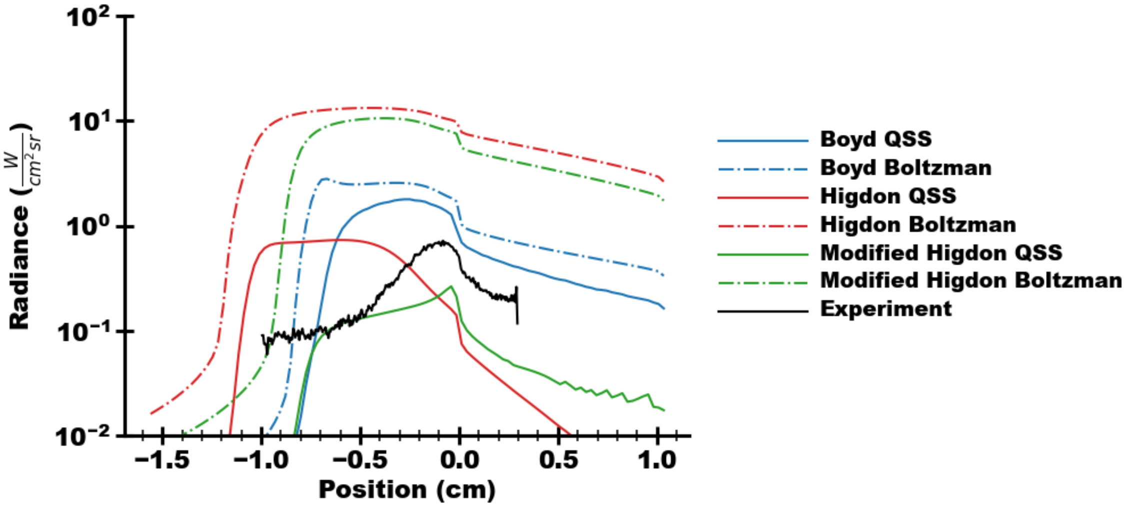

Figure 5.13: Radiance profiles measured along stagnation steamline with instrument convolution, intensity is averages around the $H\alpha$ band (476 nm - 497 nm). Data is identical to Figure 5.12, but scale is logarithmic.

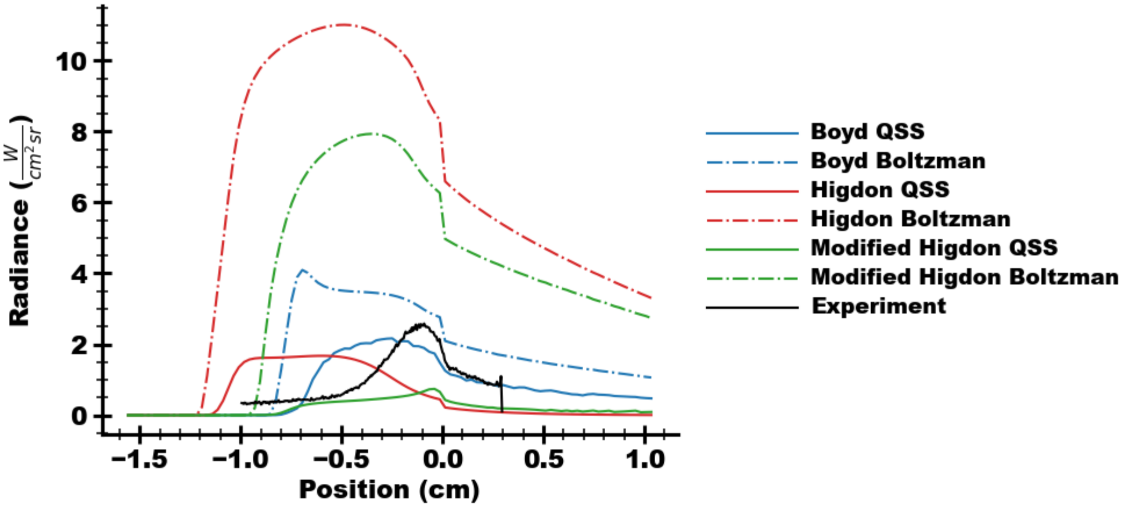

Figure 5.14: Radiance profiles measured along stagnation steamline without instrument convolution, intensity is averages around the $H\beta$ band (640 nm - 670 nm).

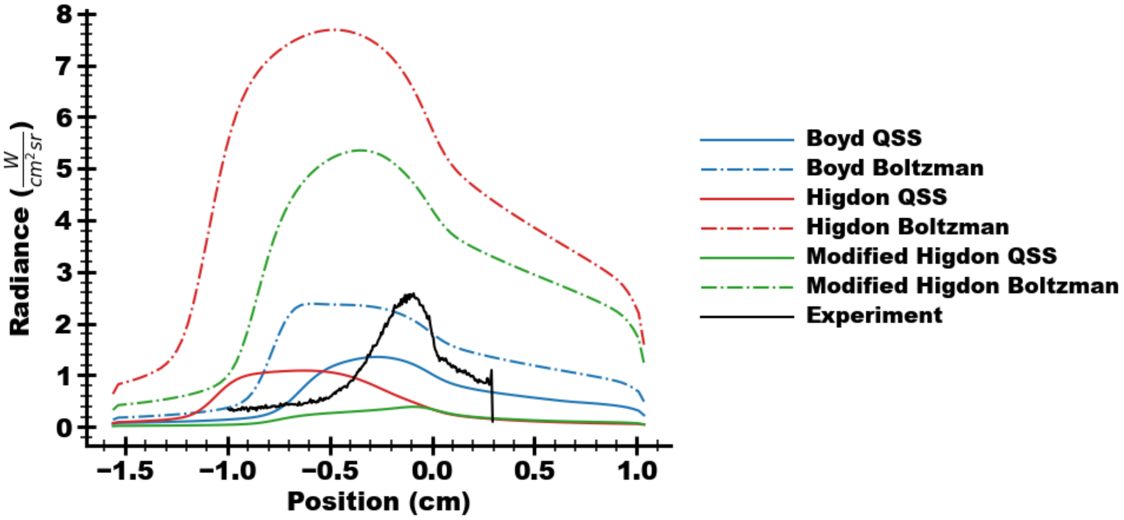

Figure 5.15: Radiance profiles measured along stagnation with instrument convolution, intensity is averages around the $H\beta$ band ($640nm - 670nm$).

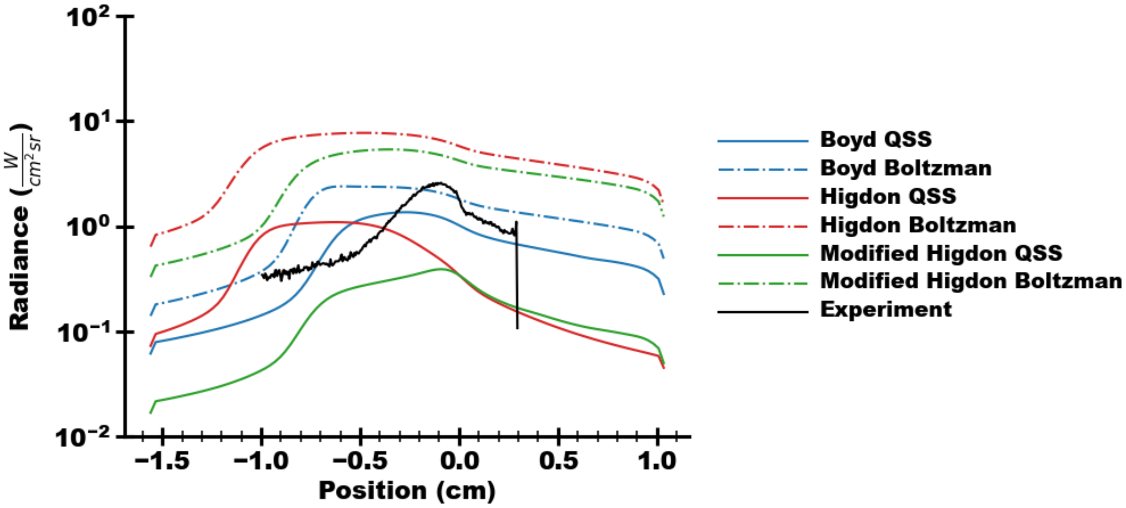

Figure 5.16: Radiance profiles measured along stagnation with instrument convolution, intensity is averaged around the $H\beta$ band ($640nm - 670nm$). Data is identical to Figure 5.15, but scale is logarithmic.

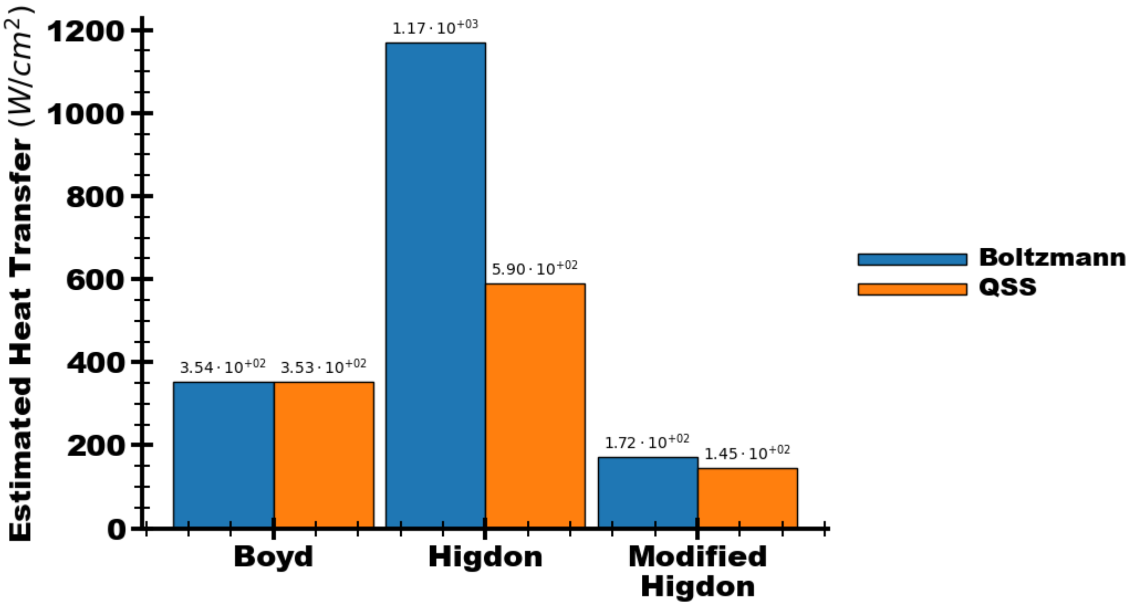

Figure 5.17: Estimated radiative heat transfer to the stagnation point of the flow. These are estimated as π times the radiative heat flux along the stagnation line. One can see that the radiative heat flux spans an order of magnitude depending on the CFD chemistry and excited state model.

the 656 nm line using all combinations of chemical rates and excited state modeling. All conditions show that QSS methods produce significantly different results. Once again, it is assumed that the QSS methods are more accurate. Comparisons with experiments are only considered using QSS methods.

The Shot 22 QSS results and experimental measurements are plotted in Figures 5.30, 5.32, and 5.34. Figure 5.34 shows the integrated red spectrum over the 2 cm behind the shock. It is noted that the best prediction occurs using the Modified Higdon rates, although the amount of line broadening is different between measurements and simulations. Figure 5.32 shows the complete spectrum over all regions. One feature that can only be seen in this figure is the electron-free-free collision spectrum which exists in the 300 nm region. This energy is directly related to electron density. It is, therefore, unsurprising that the Boyd rates predict the highest radiance and the Higdon rates the lowerest radiance in that region. The Modified Higdon rates, however, closely match the measured radiance in the blue region of the East data.

The radiance profiles of Figure 5.30, must be interpreted in terms of the experiment. Likely much of the radiance far from the shock (5 cm and beyond) represents a gas mixture that includes driver gas. The regions of most importance are those close to the shock. The IR region must be evaluated with consideration for a much longer exposure time compared to other results. There are two regions of primary interest. First is the VUV peak at the shock. This peak represents the excitation of molecular hydrogen. The calculation of this quantity is dependent on the number densities of electrons and molecular hydrogen (as electron impact is the primary excitation mechanism) as well as the heavy particle quenching rate. This calculation is based on the quenching cross-section at 300K. There is relatively high uncertainty on this value which can dramatically affect the intensity in the VUV region. Aside from this ultraviolet peak, there is a unique phenomenon in the red region right at the shock. The experimental results have two clear points where the radiance rises, as opposed to a smooth rise in intensity. This may suggest that two processes are occurring: first, a reaction involving a small number of equilibrium electrons with a relatively fast reaction rate followed by, second, a slower process that produces many more electrons. This would create a small fast jump in the radiance followed by a fast rise. The numerical predictions display only a single rise, best approximated by the Modified Higdon rates.

The Shot 18 QSS results and experimental measurements are plotted in Figures 5.29, 5.31, and 5.33. Here, the experimental results must be interpreted with an awareness that the measurements are very near the noise floor of the instruments. For example, the IR region of Figure 5.29 can all be interpreted as effectively zero. The trends between the chemical models are all similar to the Shot 22 results. One notable exception is that the 656 nm peak is predicted lower by the Modified Higdon model than by the original Higdon model. This is likely a result of the higher temperature present in the Higdon model. The relation of the various predictions to the experimental results also stands in contrast to the Shot 22 results. Figure 5.33 shows that the Modified Higdon rates are less accurate in these conditions. The electron free-free region (300 nm) in Figure 5.31 is not matched by the Modified Higdon rates and is closer to the radiances predicted by the Boyd rates.

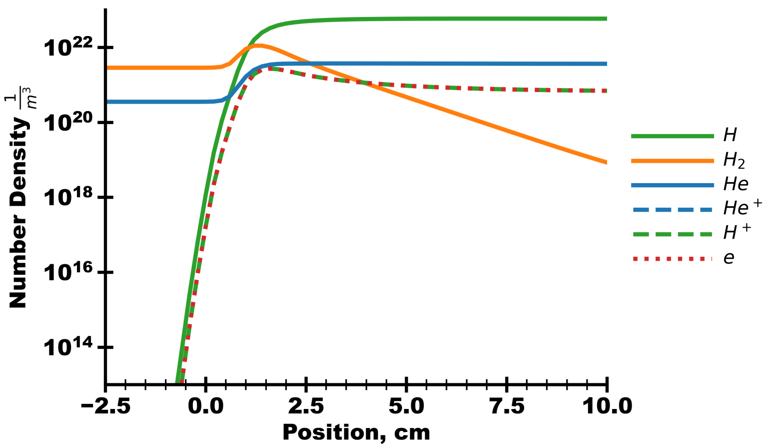

(a) Boyd Chemistry

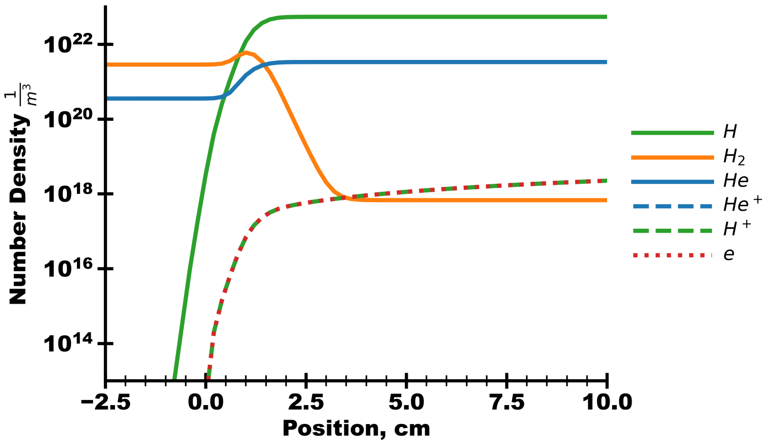

(b) Higdon Chemistry

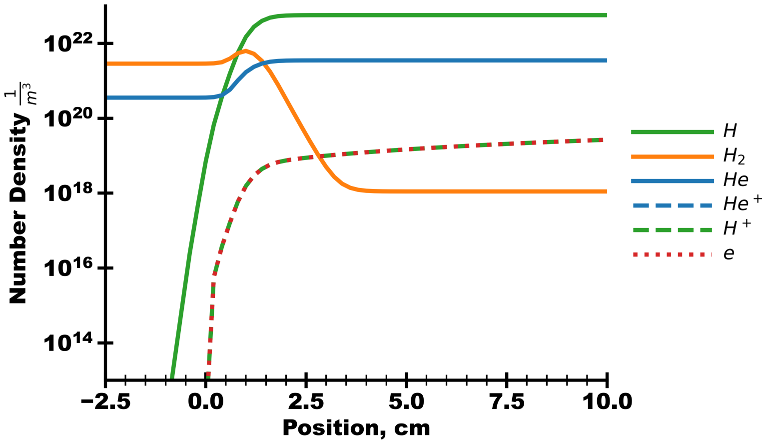

(c) Modified Higdon Chemistry

Figure 5.18: Number densities of species in flows representing Shot 18 conditions with different CFD chemistry models.

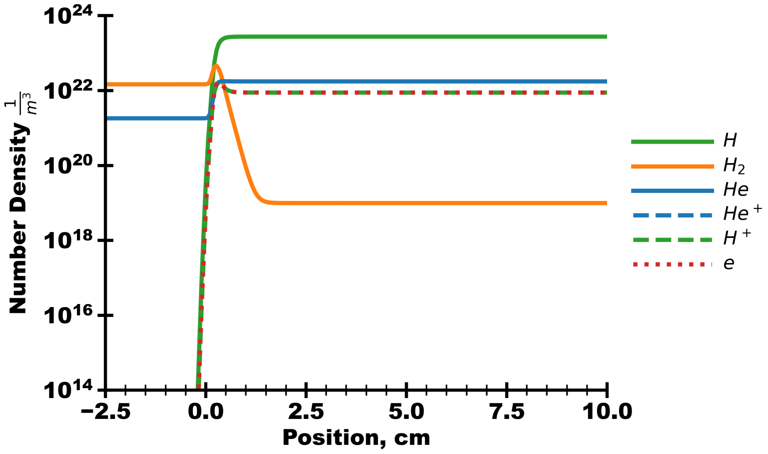

(a) Boyd Chemistry

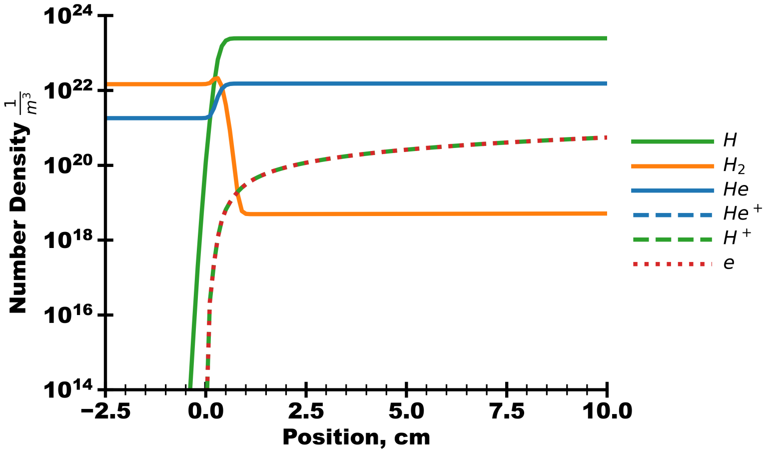

(b) Higdon Chemistry

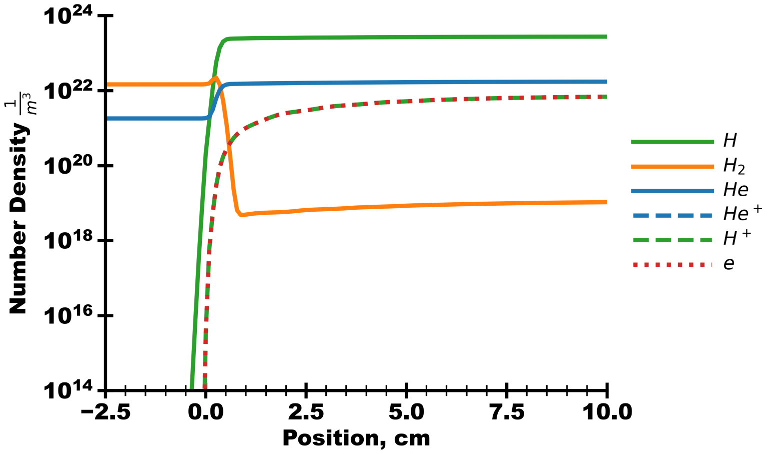

(c) Modified Higdon Chemistry

Figure 5.19: Number densities of species in flows representing Shot 22 conditions with different CFD chemistry models.

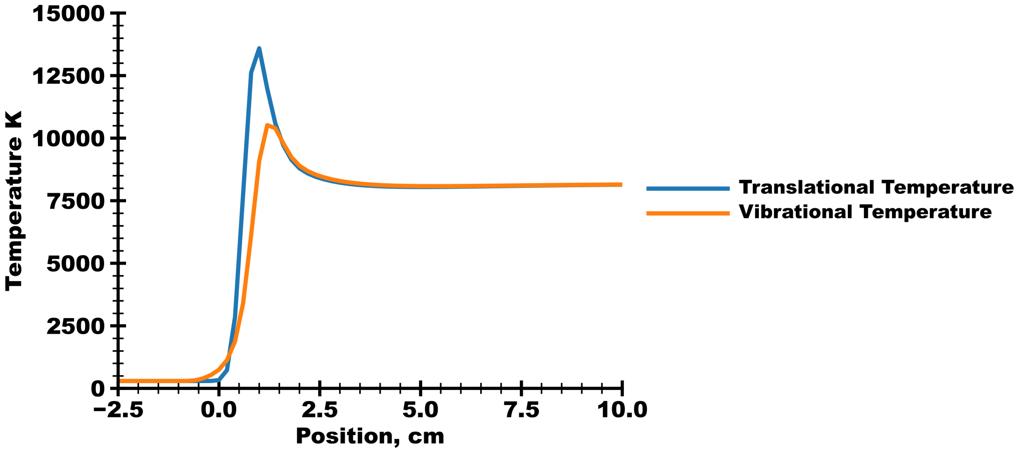

(a) Boyd Chemistry

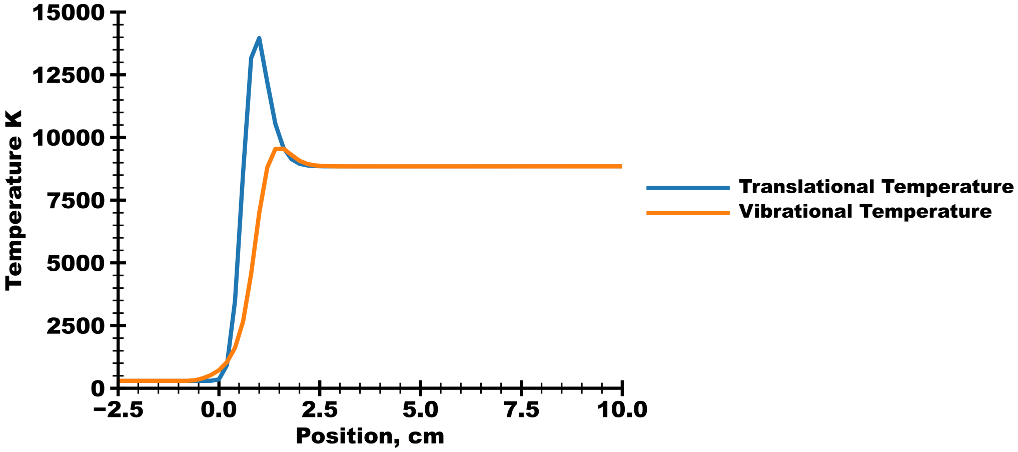

(b) Higdon Chemistry

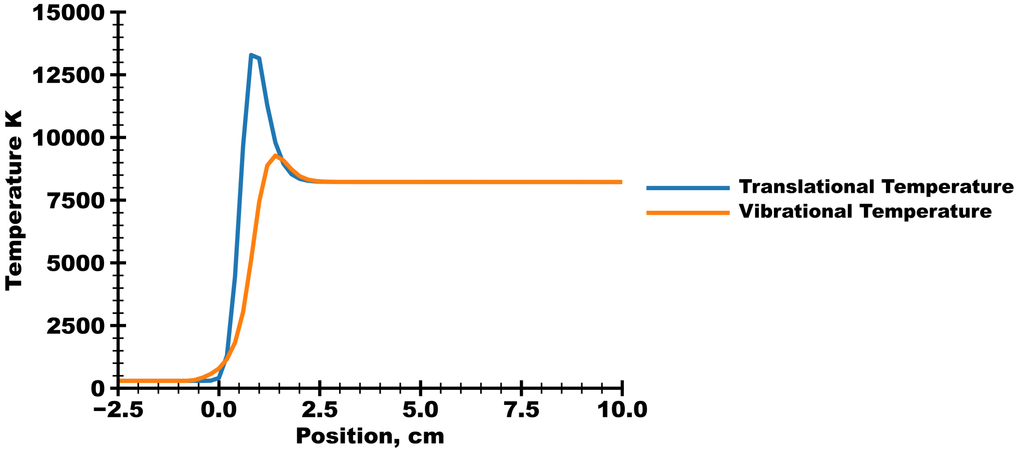

(c) Modified Higdon Chemistry

Figure 5.20: Temperatures in flows representing Shot 18 conditions with different CFD chemistry models

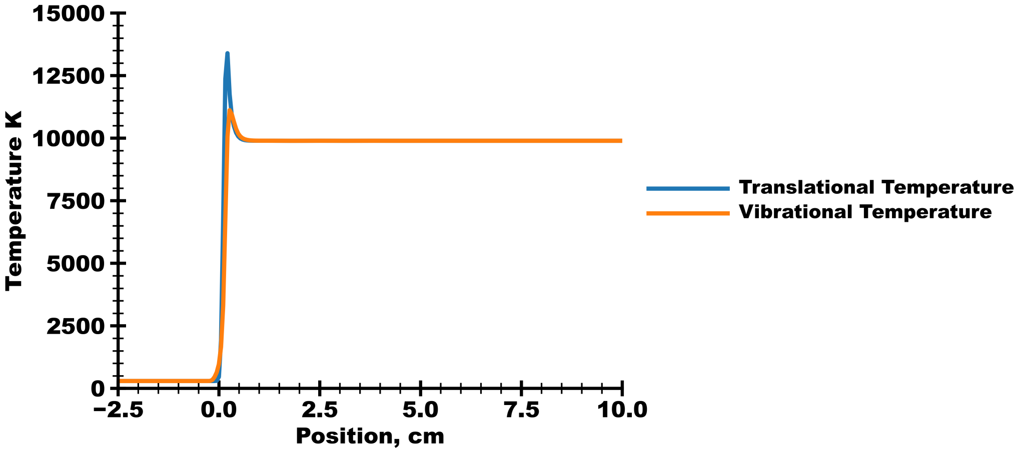

(a) Boyd Chemistry

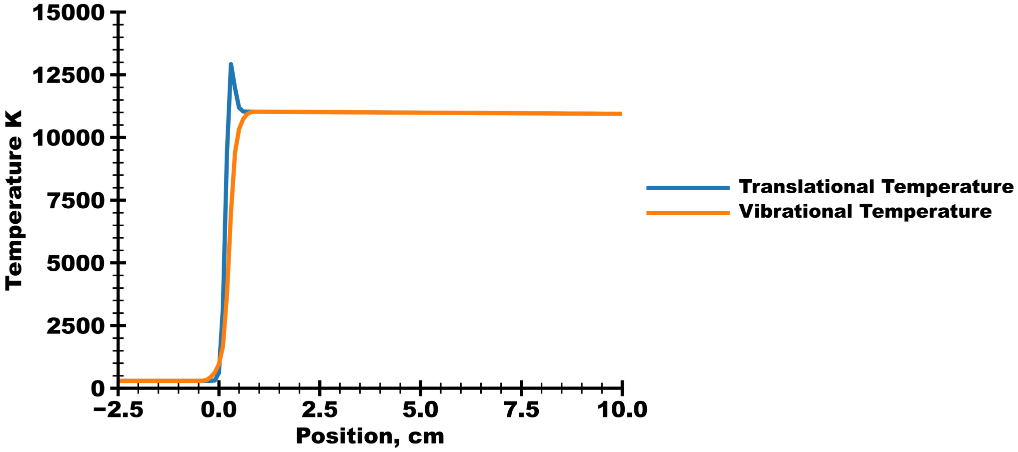

(b) Higdon Chemistry

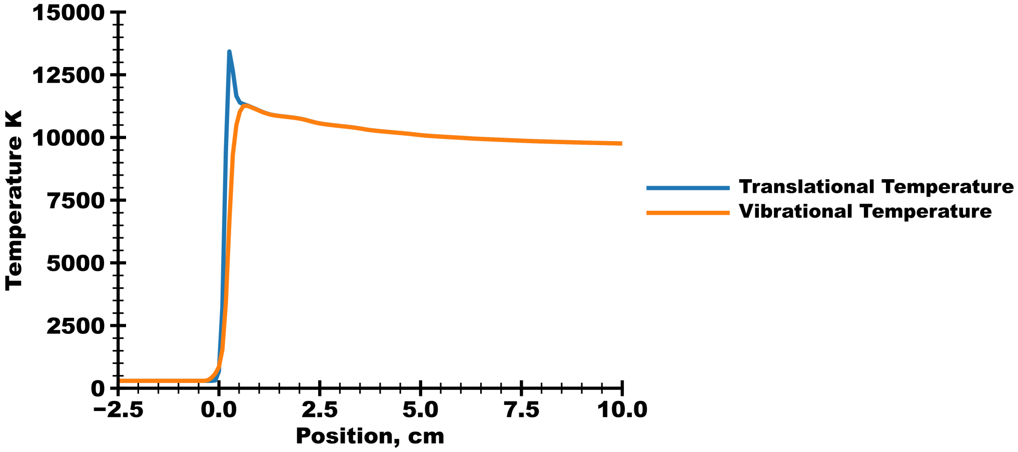

(c) Modified Higdon Chemistry

Figure 5.21: Temperatures in flows representing Shot 22 conditions with different chemistry models

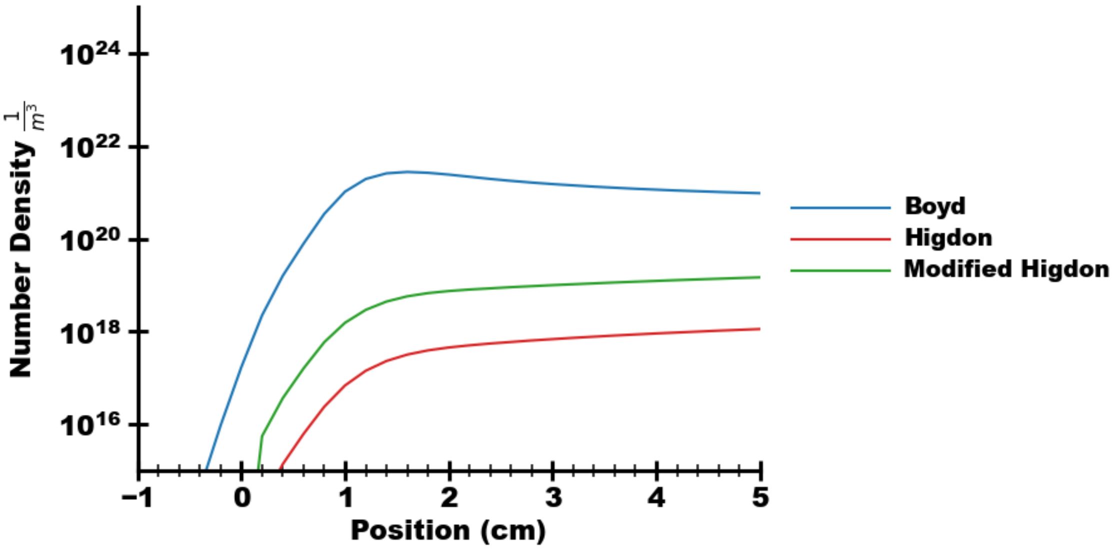

Figure 5.22: Number densities of electrons of flow in the Shot 18 conditions with various chemical models

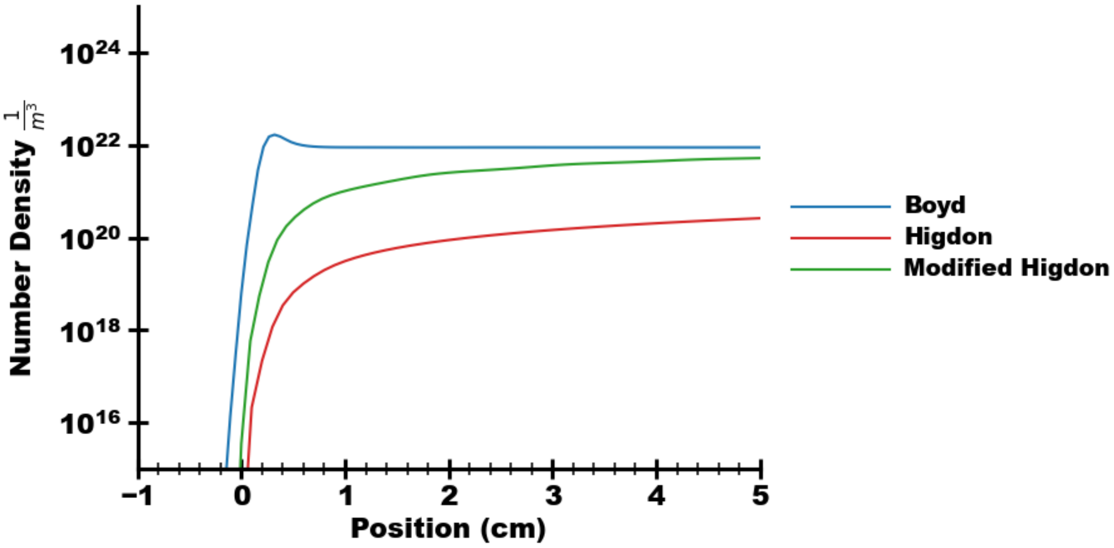

Figure 5.23: Number densities of electrons in flow of the Shot 22 conditions with various chemical models

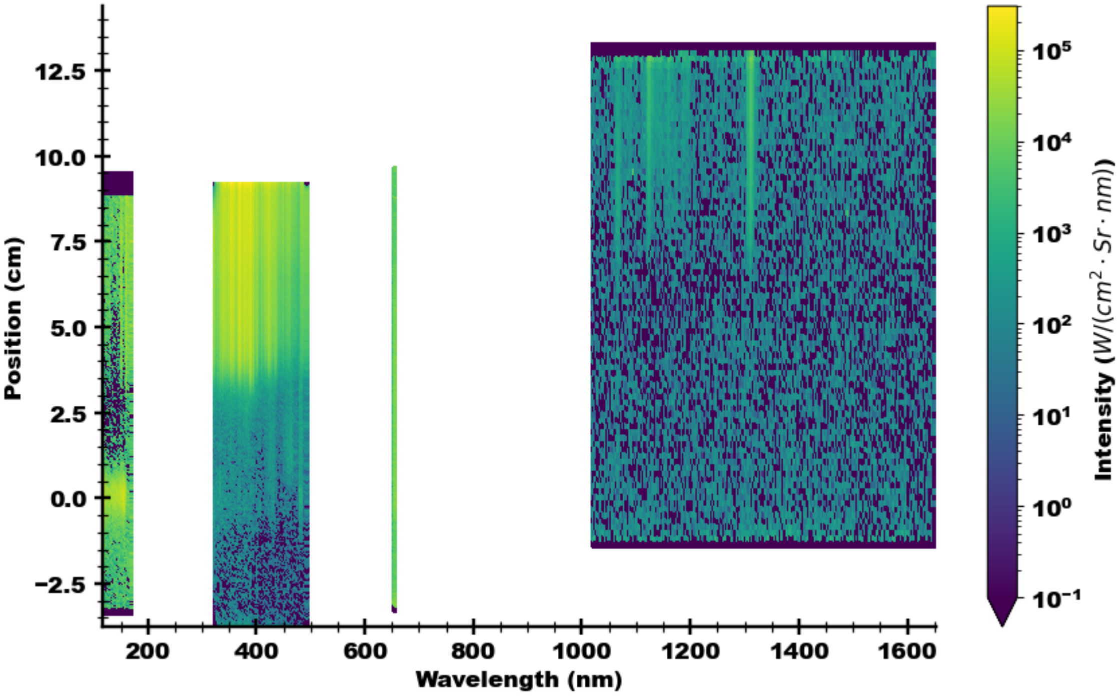

Figure 5.24: Experimental measurements from EAST for Shot 18 conditions. Note that the IR reagion (far right) is nearly at the intrument noise floor.

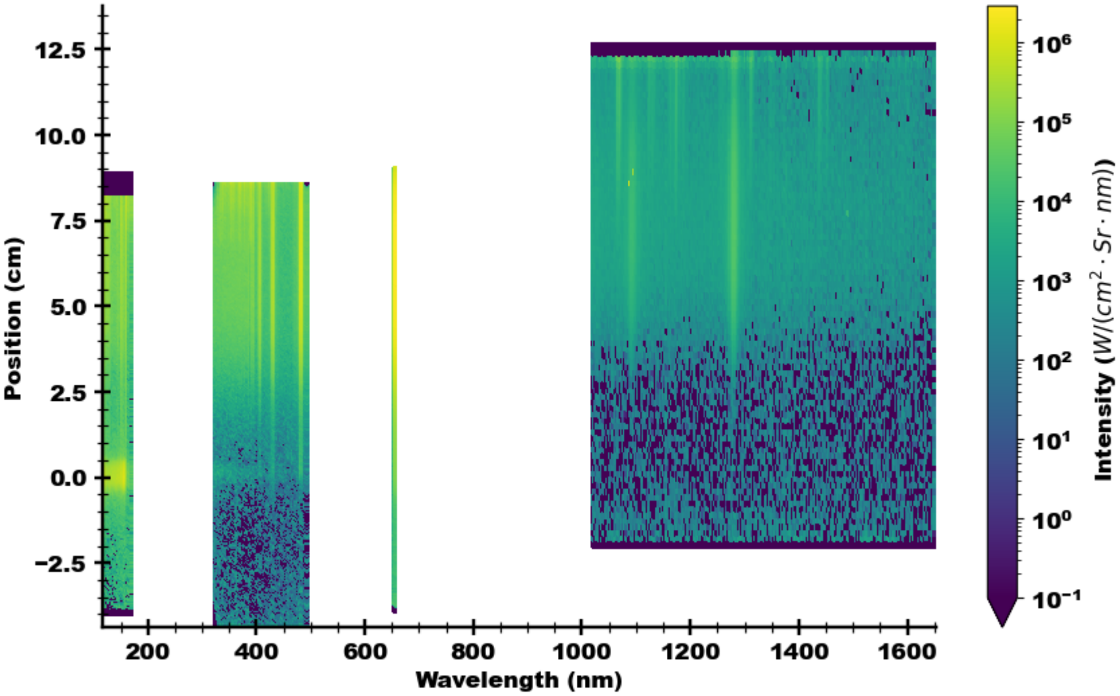

Figure 5.25: Experimental measurements from EAST for Shot 22 conditions

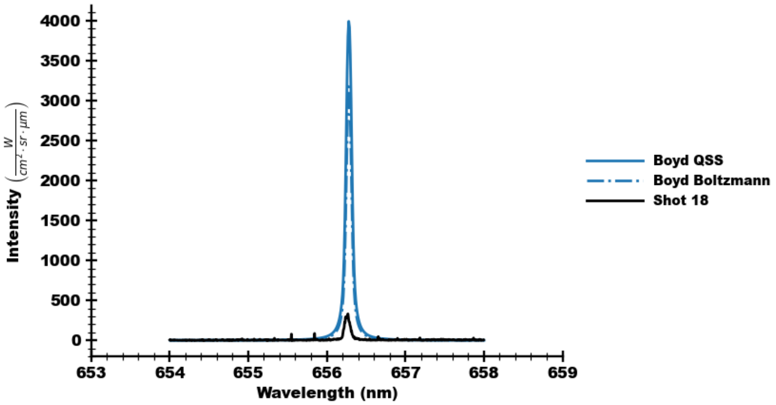

(a) Boyd Chemistry

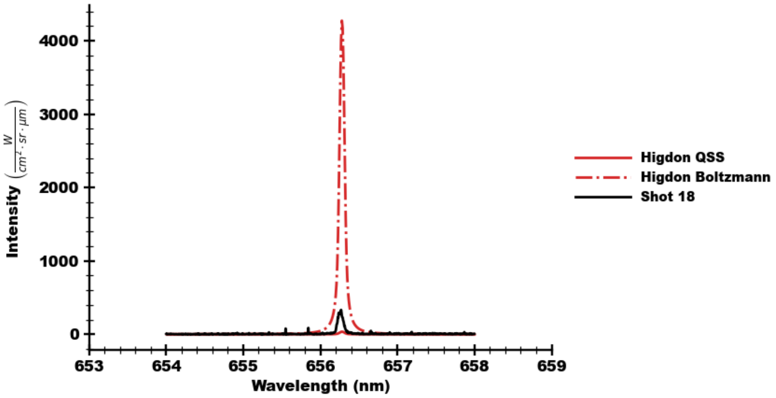

(b) Higdon Chemistry

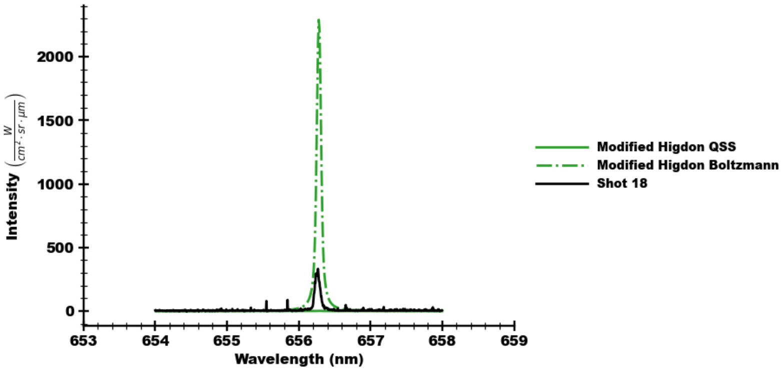

(c) Modified Higdon Chemistry

Figure 5.26: High resolution plot of the atomic hydrogen 656 nm peak (β emission) for Shot 18. The Boltzmann and QSS results for each CFD chemistry are plotted sperately.

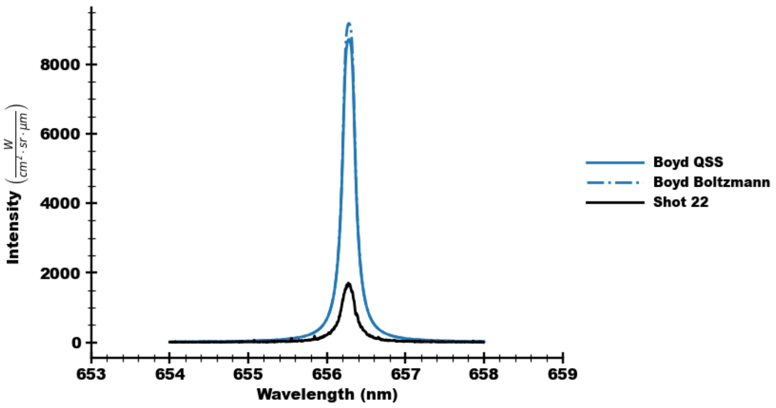

(a) Boyd Chemistry

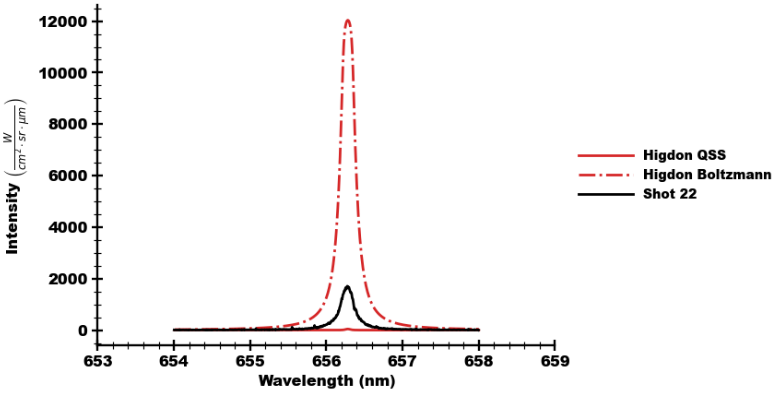

(b) Higdon Chemistry

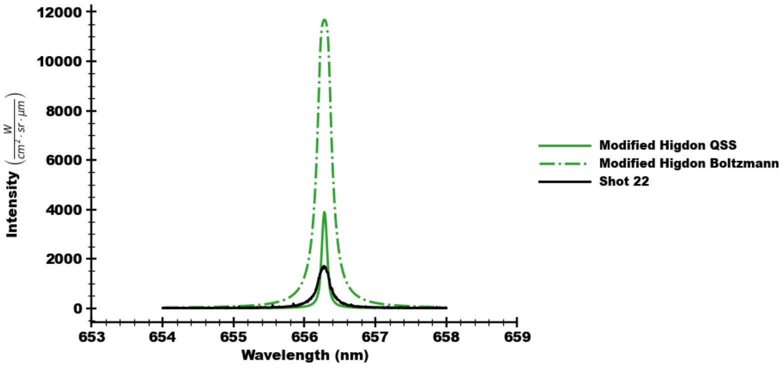

(c) Modified Higdon Chemistry

Figure 5.27: High resolution plot of the atomic hydrogen 656 nm peak (β emission) for Shot 22. The Boltzmann and QSS results for each CFD chemistry are plotted sperately.

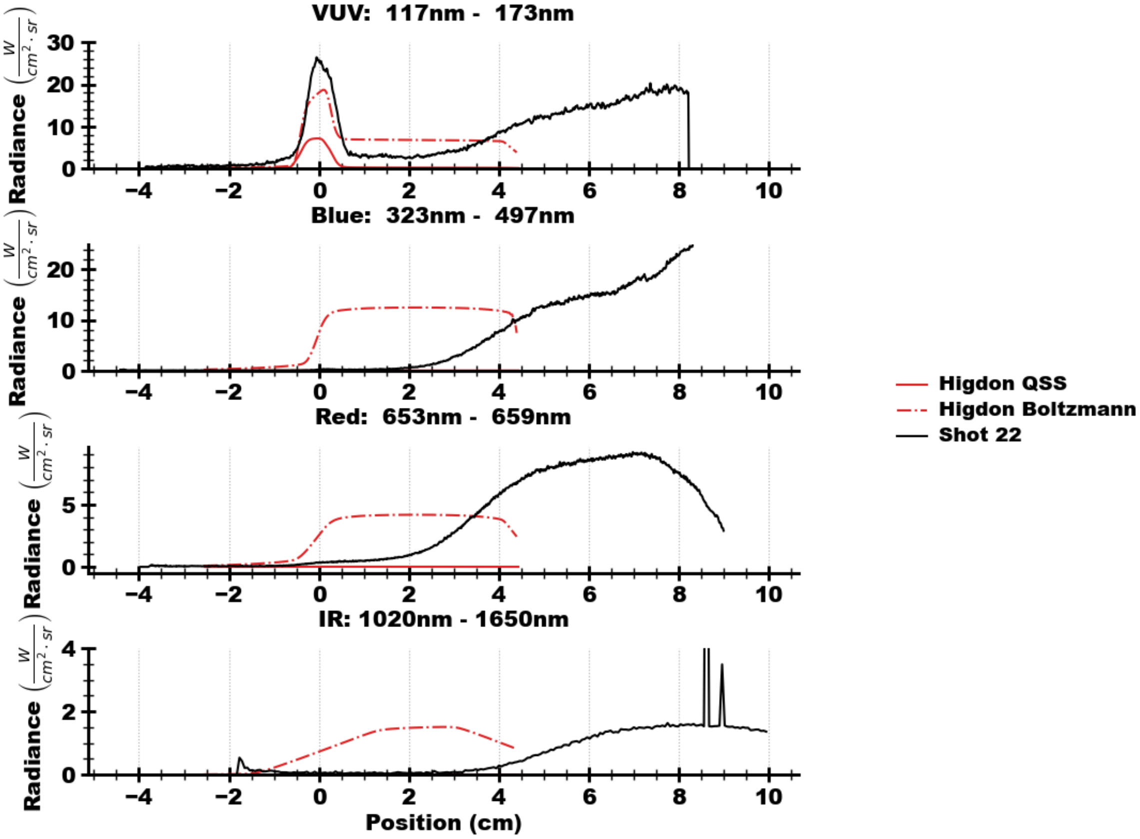

Figure 5.28: Integrated radiance with respect to position over the EAST wavelength bands. The modeled lines compare the Boltzmann and QSS models for the Shot 22 conditions with the same underlying CFD chemistry (Higdon rates).

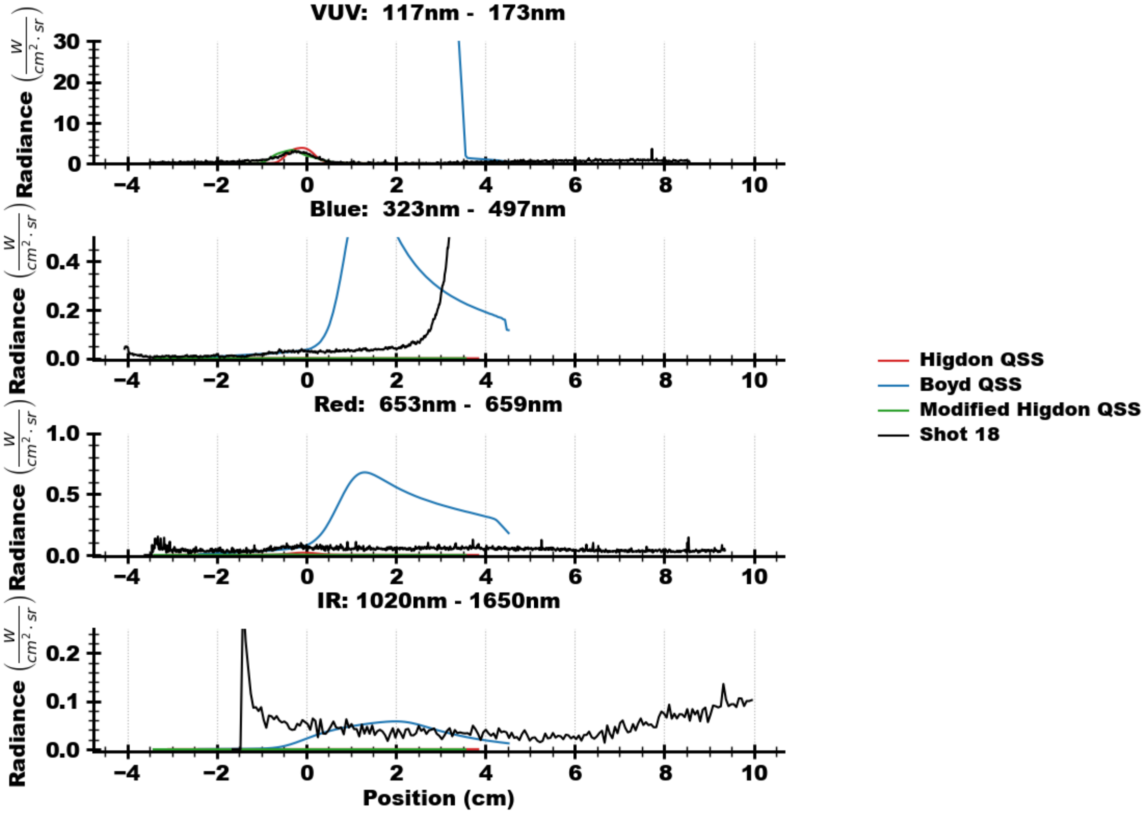

Figure 5.29: Integrated radiance as a function of a position for Shot 18, include all QSS predictions. Each EAST spectal region is plotted seperately.

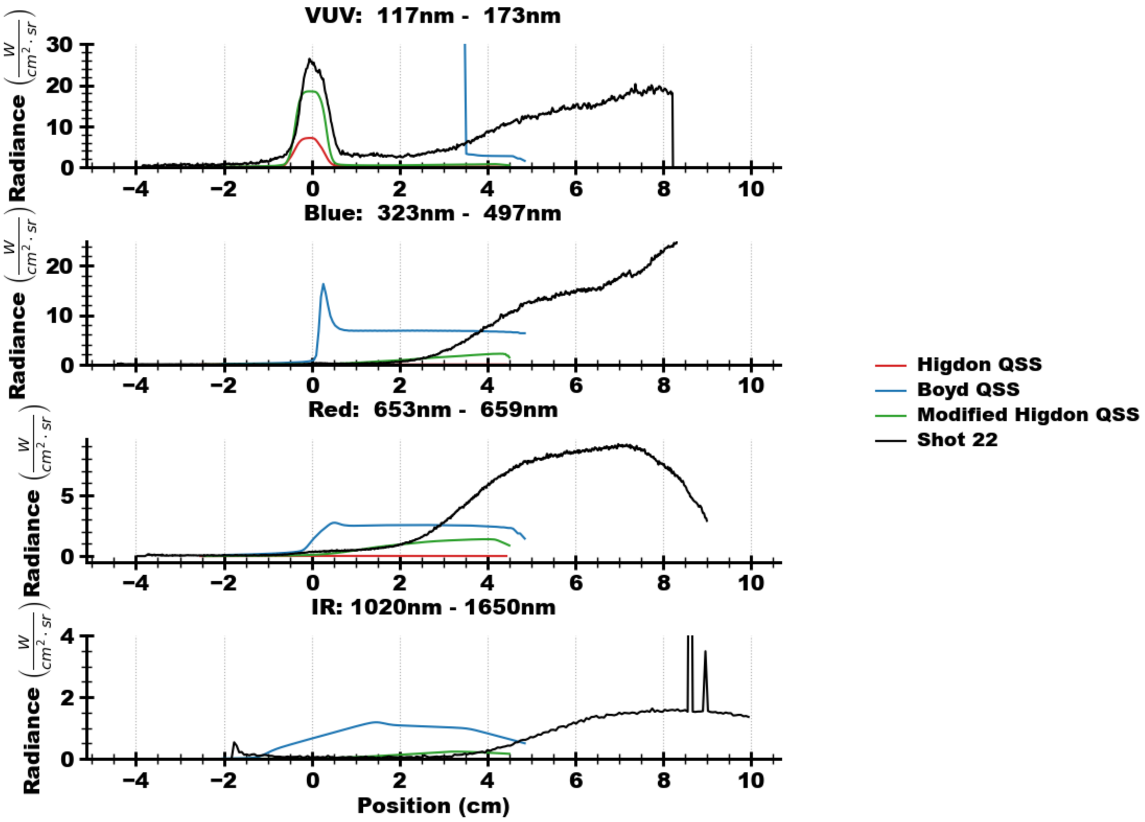

Figure 5.30: Integrated radiance as a function of a position for Shot 22, include all QSS predictions. Each EAST spectal region is plotted seperately.

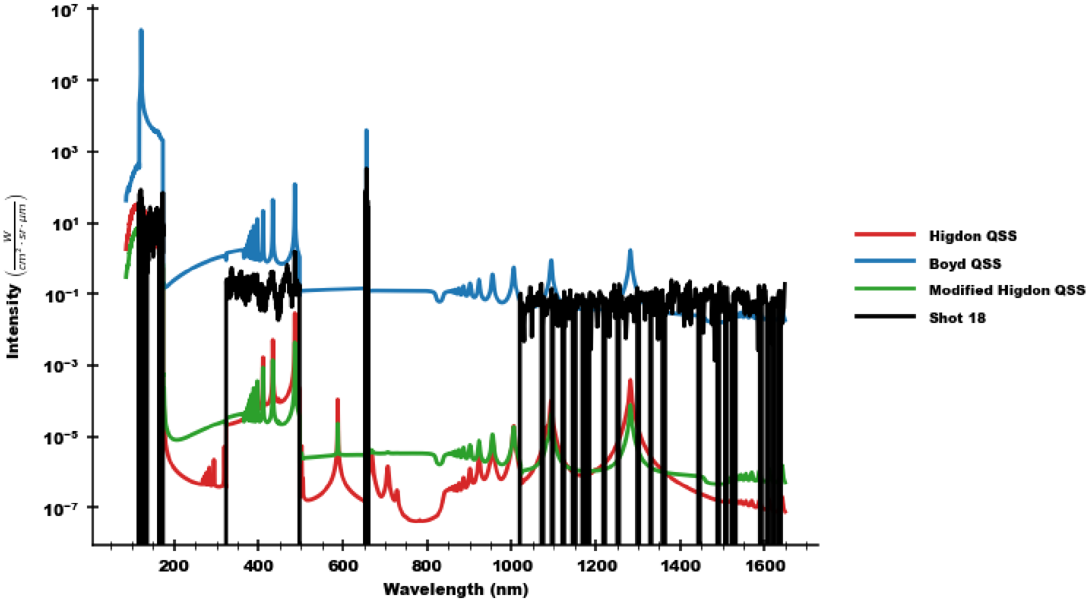

Figure 5.31: Spectral signal averaged over the 2 cm behind the Shot 18 shock.

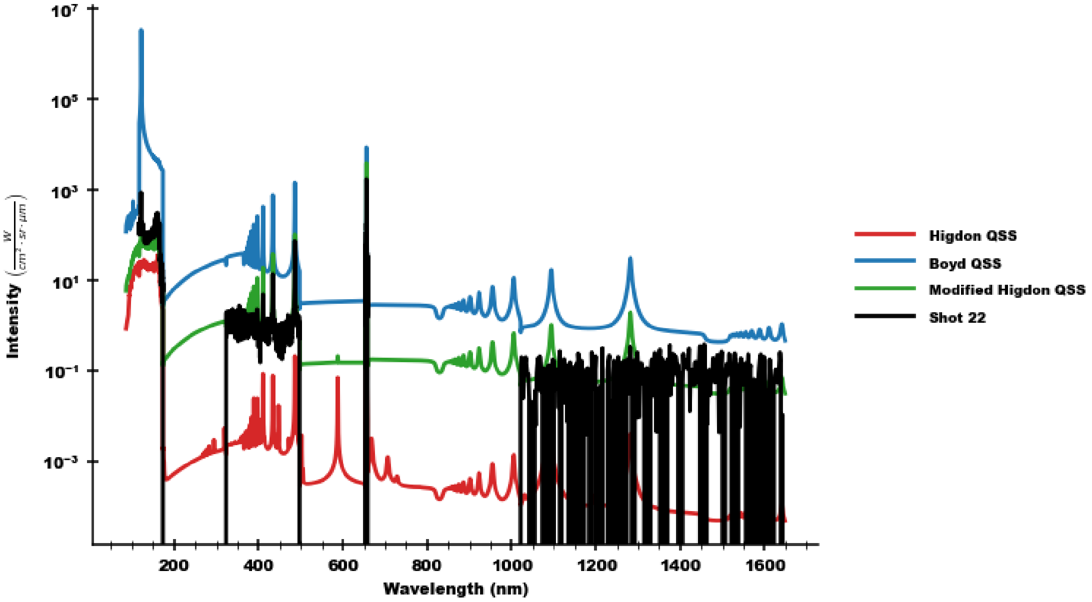

Figure 5.32: Spectral signal averaged over the 2 cm behind the Shot 22 shock.

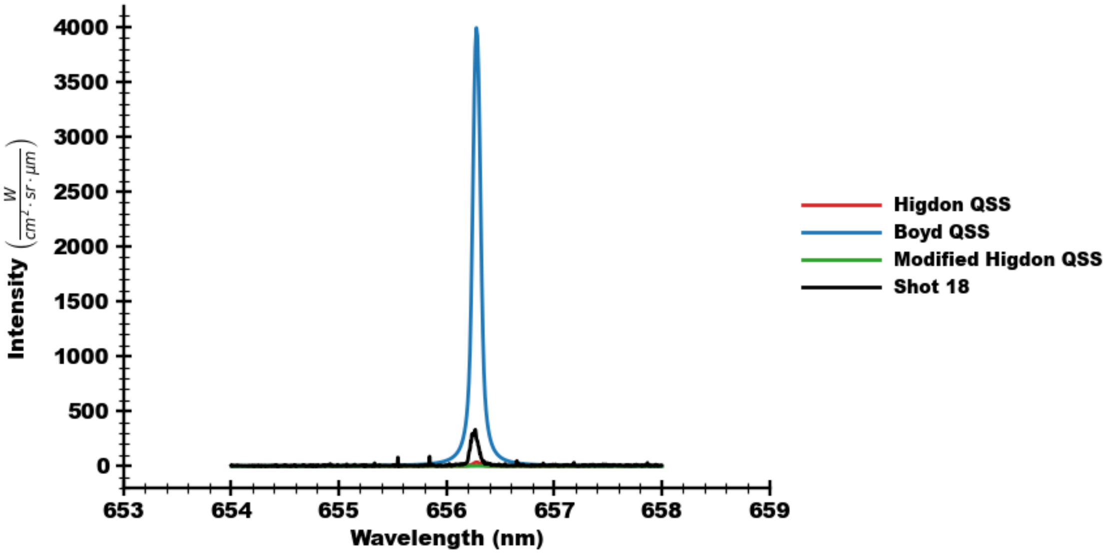

Figure 5.33: High resolution plot of the atomic hydrogen 656 nm peak (β emission) for Shot 18 including only QSS results.

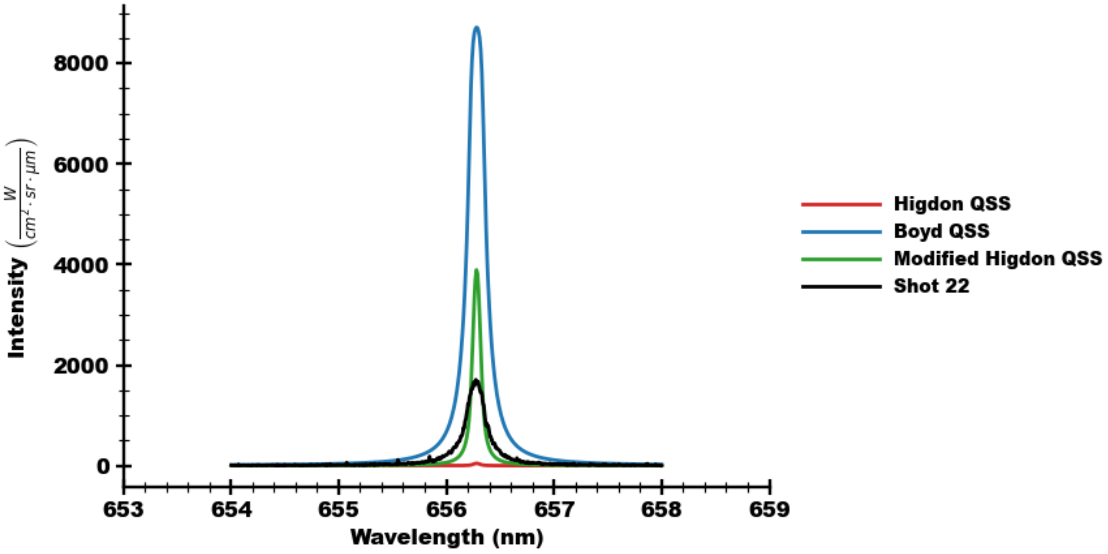

Figure 5.34: High resolution plot of the atomic hydrogen 656 nm peak (β emission) for Shot 22 including only QSS results.

5.5 Summary and Conclusions

Current aerothermochemistry models for hydrogen helium system were evaluated in terms of radiative transfer and spectral measurements taken in shock layers. The numerical predictions were performed in two steps. First, a CFD calculation was performed using standard techniques for hypersonic flows. Three chemical rates were examined: those attributed to Boyd and those to Higdon, plus a Modified Higdon model which raised the leading coefficient on all ionization rates by a factor of 25. Radiative transfer and spectral predictions were performed using NEQAIR. Two modes were used to calculate the excited states: an assumed Boltzmann distribution or the quasi-steady-state approximation.

The QSS method requires a collection of state-to-state rates for all excited states in the system. The Hydrogen QSS rates were compiled as part of this work. Application of the QSS model verified that the Boltzmann approximation for excited states is invalid for non-equilibrium hydrogen-helium flows. The current QSS model presented does have uncertainties. Most notably, the quenching rates of molecular hydrogen are not known for all states.

The QSS model was used to compare CFD chemistry models to spectral measurement in several experimental flows. This included stagnation lines in axisymmetric flows and post shock measurements in a shock tube. No chemistry model when combined with the QSS model led to radiative predictions which matched all experimental measurements. The Modified Higdon rates predicted the best trends when modeling the Queensland experiment but inaccurately predicted the shock standoff distance. The Boyd rates produced significantly too high a radiance in the strong shock case in the EAST experiments (Shot 22) but were the most accurate in the lower shock speed case (though they still generally overpredicted radiance). The Higdon rates most accurately captured the shock standoff distance, but inconsistently captured the radiance profiles (i.e. underpredicted or overpredicted).

These results suggest a few properties of an ideal hydrogen-helium model. First, the ionization reaction has relatively strong inverse dependence on temperature. That is to say that the exponent in the modified Arrhenius rates is likely less than zero. This is due to the increased success of the highly ionizing Boyd model at low shock strengths and in the near-wall region of the Queensland experiment. Second, if the ionization rate is faster, then a further change in the chemical models must be made to delay the rise in internal energy after a shock. This is suggested because the Higdon rates, which ionized the slowest, best predicted the shock standoff distance. If ionization must proceed faster, the loss of translational energy must be mitigated by some means. This may be through an adjustment in the vibrational relaxation time, a reduction in the dissociation rate, or both.

In conclusion, as one considers faster and faster entry conditions into gas giants, the uncertainties in the experienced heat loads especially due to radiative transfer become greater. This increases the failure risks, leading to engineering decisions that overdesign thermal protection systems, or simply avoiding the mission altogether. The success of future missions hinges on quantifying the errors and uncertainties in current aerothermodynamic models — as has been done here — and using this understanding to assemble more accurate and efficient models of hydrogen-helium flows.

CHAPTER 6

Conclusion

6.1 Summary

This dissertation focused on radiative transfer simulations of particle laden flows and reacting flows. Chapter 2 presented the electromagnetic theory for the scattering of small particles. This included conventions for the spherical vector harmonic expansions used. Numerical procedures for shelled particles were discussed as well as modifications to account for particle magnetic permeability. Lastly, the Extended Boundary Method was discussed for irregular dielectric particles. The method was modified to use a surface impedance boundary condition. This permitted the calculation of the optical properties of large absorbing spheroids; particles that could not be examined in the dielectric framework because of numerical instability.

Chapter 3 extended the electromagnetic theory of a single particle to a radiative transfer theory for a collection of particles. This chapter focused on the homogenization of particles using the Beer-Lambert Law. It was found that high particle concentrations could decrease the transmissivity of particle clouds, an effect that could not be predicted by the Beer-Lambert Law. This was determined to be an effect of the anti-clustering of particles that could not overlap. Furthermore, numerical errors could be introduced by overrefining a mesh over the particles. A model was proposed that mitigated both errors.

Using the tools of the previous chapters, an examination of a radiatively heated particle-laden flow was carried out in Chapter 4. A completely particle resolved radiative transfer simulation was developed, using high fidelity scattering profiles for the particles. This simulation could make detailed predictions of the radiative emission and sensing that matched the experimental geometry. It was found that accurately modeling the experimental sensors and emitters was critical to predict the transmission through the flow. However, simplified homogenization models and scattering models were sufficient. Nonetheless, transmission predictions based on a coupled flow simulation tended to over-predict transmission by approximately 5%.

To determine the source of these discrepancies, a comprehensive study of the optical properties of the nickel particles used in the flow was carried out. It was shown that no physical change in the particles themselves could yield optical properties that changed the flow's transmissivity. It was, therefore, suggested that particle sticking was a mechanism to increase transmission. Using experimental measurements, estimates were performed to determine the number of particles that would need to be bound to the channel walls. This suggested at least 150% more particles would have to be added as wall-bound particles in order to yield predictions consistent with experiments. This suggests that the specular particle interaction with channel walls is not an accurate representation of the particle dynamics.

Chapter 5 presented a different type of radiative analysis; one that focused on spectral data as much as geometric. This chapter analyzed the flow of reacting hydrogen-helium mixtures. The mixture profiles were developed using CFD methods and simplified finite rate, chemistry models. Using QSS models to calculate excited state modeling and a line-by-line radiative transfer solver, each finite rate chemistry model could be examined in the context of multiple experimental measurements. It was found that no finite rate chemistry model currently exists which captures the experimental measurements.

In conclusion, this research has primarily used increased fidelity of radiative transfer models to illuminate the inaccuracies of the simulations these models are applied to. This demonstrates that these models are not a secondary calculations to be performed, but a critical aspect of any high fidelity physics simulation. Now that experiments and simulations are more tightly tied together with these models, one can expect that revising the underlying simulations can proceed in short order. The integration of radiative transfer calculations into these simulations will only accelerate the research process.

6.2 Novel Research Contributions

The research presented in this dissertation has touched multiple fields including electromagnetic theory, particle transport, turbulence interactions, and spectroscopy. The major contributions that resulted from this work may be summarized as follows:

- The scattering of shelled spheres was extended to include a relative magnetic permeability.
- The Extended Boundary Method was reformulated to use a surface impedance boundary condition.
- The validity of Beer-Lambert homogenization was examined in the context of solid

particles.

- A new homogenized model was developed to account for errors found to be present in Beer-Lambert homogenization
- The need for accurate particle-wall sticking models was shown to increase the accuracy of particle-laden flow modeling.
- A quasi-steady-state model of excited hydrogen states was developed. It was shown that this model resulted in significantly different spectral predictions than a Boltzmann distribution of excited states.
- The radiative properties of hydrogen flow chemistry were shown to be highly dependent on the atomic ionization rate.
- Current CFD models of hydrogen-helium flow were shown to not accurately capture the experimentally measured radiance.

6.3 Recommendations for Future Work

This body of work has shown that the modeling two physical phenomena currently require development. First, it was shown that particle sticking phenomena are important in wall-bounded particle-laden flows. Understanding the physical mechanisms that initiate this effect is necessary to progress simulations of particle-laden flow. There are three possible avenues of study. First, the effect may be due to electromagnetic forces induced by the incident radiation. Second, the sticking may be a purely adhesive phenomenon activated by temperature. Third, the particles may not be stuck but rather trapped into a rolling state along the particle wall with no mechanism to detach into the fluid again.

Secondly, this dissertation also showed that high-temperature hydrogen chemistry is currently inaccurately modeled in CFD for aerospace applications. Specifically, the atomic hydrogen ionization rates were shown to be the dominant source of error. It is recommended that a comprehensive study of minor species be undertaken (e.g. H_3^+, H_2^-, etc.) as well as a compilation of all the state-specific rate data currently available. A reduced model can only be developed once the underlying physics is thoroughly understood.

Experimentally, several modifications to current experiments or new experiments entirely would facilitate the study of these flows. On the particle-laden work, increased diagnostics that capture the intensity of scattered light would be easily comparable to data that is already generated in numerical simulations. This would make the distribution of particles more evident. Replacing the calorimeter with a sensor with spatial resolution would also have greatly aided numerical analysis. Experiments will also need to be performed in the future to analyze just the particles-wall interactions without the particle laden turbulence. Simple experiments such as dropping particles on an irradiated glass sheet may be enough to form empirical relationships that may augment future fully coupled simulations.

The studies in reacting hydrogen chemistry would be facilitated by modern experiments into single state rate coefficients. It was found that accurate quenching rate or heavy particle excitation rates were the most difficult to procure. These can be experimentally found by taking radiative lifetime measurements of hydrogen at high pressures [144,145]. Modern work has focused on using low pressures to accurately measure the radiative lifetimes [146,147] or can directly these lifetimes with numerical methods [138,148,149]. This data could then be used to analyze high pressure emission and determine more accurate quenching rates.

From a numerical perspective, this work has used radiative transfer as a means of comparing numerical simulation data to experimental measurements. However, the radiative transfer models were not integrated into any of the numerical simulations used to generate flow fields. For instance, the radiative heating used in the coupled simulations of the particle-laden flow was not the same heating source as that used in the radiative transfer model. It is unlikely that this significantly affected the particle clustering, but it is not a certainty. Similarly, the chemistry rates used in the excited state model are not necessarily consistent with those in the CFD rate models.

The modeling of the hydrogen flows used a fairly primitive line of sight method to determine the geometric arrangement of intensity. Although acceptable for one-dimensional or quasi-one dimensional situations, this method can not capture multidimensional effects such as reflections and photoionization due to off-axis sources. The results of the particle-laden turbulent models have shown that the measured intensity is as dependent, if not more dependent on the correct arrangement of the emitter sources and sensors than on the modeling of the particulate itself. This principle likely holds true for the modeling of reacting flows as well. The development of a multidimensional radiative transfer simulation framework for these types of flows should be developed and, if possible, integrated into CFD calculations.

BIBLIOGRAPHY

[1] Trainer, M., "The 50th anniversary of the laser," *World Patent Information*, Vol. 32, No. 4, dec 2010, pp. 326–330.

[2] Lewis, E. E. and Miller, W. F., "Computational methods of neutron transport," 1984.

[3] Petty, G. W. G. W., *A first course in atmospheric radiation*, Sundog Pub, 2006.

[4] Rybicki, G. B. and Lightman, A. P., *Radiative Processes in Astrophysics*, Wiley-VCH Verlag GmbH and Co. KGaA, Weinheim, Germany, may 1985.

[5] BURTON, R. A., "A modified Schlieren apparatus for large areas of field." *Journal of the Optical Society of America*, Vol. 39, No. 11, nov 1949, pp. 907.

[6] Barnes, N. F. and Bellinger, S. L., "Schlieren and Shadowgraph Equipment for Air Flow Analysis," *Journal of the Optical Society of America*, Vol. 35, No. 8, aug 1945, pp. 497.

[7] Luthman, E., Cymbalist, N., Lang, D., Candler, G., and Dimotakis, P., "Simulating schlieren and shadowgraph images from LES data," *Experiments in Fluids*, Vol. 60, No. 8, aug 2019, pp. 134.

[8] Chen, F. F. and Others, *Introduction to plasma physics and controlled fusion*, Vol. 1, Springer, 1984.

[9] Papadogiannis, A. S., Papadogianni, N. S., Carabelas, A., Tsitomeneas, S., Kyraggelos, P., and Chondros, T. G., "The mirror weapon in Archimedes era," *Proceedings of EUCOMES 2008 - The 2nd European Conference on Mechanism Science*, Springer, Dordrecht, 2009, pp. 29–36.

[10] Modest, M. F. M. F., *Radiative heat transfer*, Academic Press, 2003.

[11] Sankaran, S., Esmaily Moghadam, M., Kahn, A. M., Tseng, E. E., Guccione, J. M., and Marsden, A. L., "Patient-Specific Multiscale Modeling of Blood Flow for Coronary Artery Bypass Graft Surgery," .

[12] Capecelatro, J. and Buchta, D. A., "Direct numerical simulation of noise suppression by water injection in high-speed flows," *AIAA Science and Technology Forum and Exposition*.

[13] Shotorban, B. and Mashayek, F., "Modeling subgrid-scale effects on particles by approximate deconvolution Equation of motion for a small rigid sphere in a nonuniform flow Modeling subgrid-scale effects on particles by approximate deconvolution," *Physics of Fluids Physics of Fluids The Physics of Fluids*, Vol. 171, No. 10, 2005.

[14] Bianco, F., Chibbaro, S., Marchioli, C., Salvetti, M. V., and Soldati, A., "Intrinsic filtering errors of Lagrangian particle tracking in LES flow fields," *Citation: Physics of Fluids*, Vol. 24, 2012.

[15] Cernick, M. J., Tullis, S. W., and Lightstone, M. F., "Particle subgrid scale modelling in large-eddy simulations of particle-laden turbulence," *Journal of Turbulence*, Vol. 16, No. 2, feb 2015, pp. 101–135.

[16] Apte, S. V., Mahesh, K., Moin, P., and Oefelein, J. C., "Large-eddy simulation of swirling particle-laden flows in a coaxial-jet combustor," *International Journal of Multiphase Flow*, Vol. 29, No. 8, 2003, pp. 1311–1331.

[17] Gobert, C., "Analytical assessment of models for large eddy simulation of particle laden flow," *Journal of Turbulence*, Vol. 11, No. 23, jan 2010, pp. N23.

[18] Shotorban, B. and Mashayek, F., "A stochastic model for particle motion in large-eddy simulation," *Journal of Turbulence*, Vol. 7, No. 18, 2006.

[19] Park, G. I., Bassenne, M., Urzay, J., and Moin, P., "A simple dynamic subgrid-scale model for LES of particle-laden turbulence," *PHYSICAL REVIEW FLUIDS*, Vol. 2, 2017.

[20] Michałek, W. R., Kuerten, J. G. M., Zeegers, J. C. H., Liew, R., Pozorski, J., and Geurts, B. J., "A hybrid stochastic-deconvolution model for large-eddy simulation of particle-laden flow," *Physics of Fluids*, Vol. 25, No. 25, 2013, pp. 123302.

[21] Bassenne, M., Urzay, J., Schneider, K., and Moin, P., "Extraction of coherent clusters and grid adaptation in particle-laden turbulence using wavelet filters," *Physical Review Fluids*, Vol. 2, No. 5, may 2017, pp. 54301.

[22] Kuerten, J. G. M., "Point-Particle DNS and LES of Particle-Laden Turbulent flow - a state-of-the-art review," *Flow, Turbulence and Combustion*, Vol. 97, 2016, pp. 689–713.

[23] Dai, Q., Luo, K., Jin, T., and Fan, J., "Direct numerical simulation of turbulence modulation by particles in compressible isotropic turbulence," *Journal of Fluid Mechanics*, Vol. 832, 2017, pp. 438–482.

[24] Pozorski, J., Sourabh, D., and Apte, V., "Filtered particle tracking in isotropic turbulence and stochastic modeling of subgrid-scale dispersion," .

[25] Strutt, H. C., Tullis, S. W., and Lightstone, M. F., "Numerical methods for particle-laden DNS of homogeneous isotropic turbulence," 2011.

[26] Paris, A. D., Paris, and Dana, A., "Turbulence attenuation in a particle-laden channel flow," *PhDT*, 2001, pp. 4748.

[27] Capecelatro, J., Desjardins, O., and Fox, R. O., "On the transition between turbulence regimes in particle-laden channel flows," *Journal of Fluid Mechanics*, Vol. 845, jun 2018, pp. 499–519.

[28] Eaton, J. K. and Fessler, J. R., "Preferential concentration of particles by turbulence," *International Journal of Multiphase Flow*, Vol. 20, No. SUPPL. 1, aug 1994, pp. 169–209.

[29] Ho, C. K. and Iverson, B. D., "Review of high-temperature central receiver designs for concentrating solar power," jan 2014.

[30] Marti, J. and Jr, J. V., "ASCUAS : A Solar Central Receiver Utilizing a Solid Thermal Carrier," , No. January, jan 1982, pp. 1–32.

[31] Larsen, M. L. and Clark, A. S., "On the link between particle size and deviations from the Beer-Lambert-Bouguer law for direct transmission," *Journal of Quantitative Spectroscopy and Radiative Transfer*, Vol. 133, 2014, pp. 646–651.

[32] Esmaily, M., Villafane, L., Banko, A. J., Iaccarino, G., Eaton, J. K., and Mani, A., "A benchmark for particle-laden turbulent duct flow: A joint computational and experimental study," *International Journal of Multiphase Flow*, Vol. 132, 2020, pp. 103410.

[33] Bohren, K. F. and Huffman, D. R., *Absorption and Scattering of Light by Small Particles*, Wiley, 1998.

[34] Mie, G., "Beiträge zur Optik trüber Medien, speziell kolloidaler Metallösungen," *Annalen der Physik*, Vol. 330, No. 3, 1908, pp. 377–445.

[35] Mishchenko, M. I., "Gustav Mie and the fundamental concept of electromagnetic scattering by particles: A perspective," sep 2009.

[36] Kahnert, F., "Numerical methods in electromagnetic scattering theory," *Journal of Quantitative Spectroscopy and Radiative Transfer*, Vol. 79-80, jun 2003, pp. 775–824.

[37] Steinfeld, J., *Molecules and Radiation: An Introduction to Modern Molecular Spectroscopy*, MIT Press, 2nd ed., 1989.

[38] Leibowitz, L. P., "Measurements of the structure of an ionizing shock wave in a hydrogen-helium mixture," *The Physics of Fluids*, Vol. 16, No. 1, 1973, pp. 59–68.

[39] Johnston, C. O., Hollis, B. R., and Sutton, K., "Spectrum modeling for air shock-layer radiation at lunar-return conditions," *Journal of Spacecraft and Rockets*, Vol. 45, No. 5, may 2008, pp. 865–878.

[40] Johnston, C. O., Hollis, B. R., and Sutton, K., "Non-boltzmann modeling for air shock-layer radiation at lunar-return conditions," *Journal of Spacecraft and Rockets*, Vol. 45, No. 5, may 2008, pp. 879–890.

[41] Brandis, A. M., Johnston, C. O., Cruden, B. A., Prabhu, D. K., Wray, A. A., Liu, Y., Schwenke, D. W., and Bose, D., "Validation of CO 4th positive radiation for Mars entry," *Journal of Quantitative Spectroscopy and Radiative Transfer*, Vol. 121, may 2013, pp. 91–104.

[42] Brandis, A. M., Saunders, D. A., Johnston, C. O., Cruden, B. A., and White, T. R., "Radiative heating on the after-body of Martian entry vehicles," *Journal of Thermophysics and Heat Transfer*, Vol. 34, No. 1, jan 2020, pp. 66–77.

[43] Lino Da Silva, M. and Beck, J., "Contribution of CO2 IR radiation to martian entries radiative wall fluxes," *49th AIAA Aerospace Sciences Meeting Including the New Horizons Forum and Aerospace Exposition*, Vol. 500, American Institute of Aeronautics and Astronautics Inc., 2011.

[44] Palmer, G. and Cruden, B. A., "Experimental validation of CO2 radiation simulations," *43rd AIAA Thermophysics Conference 2012*, 2012.

[45] Mazaheri, A., Johnston, C. O., and Sefidbakht, S., "Three-dimensional radiation ray-tracing for shock-layer radiative heating simulations," *Journal of Spacecraft and Rockets*, Vol. 50, No. 3, may 2013, pp. 485–493.

[46] Holloway, M. E., Hanquist, K. M., and Boyd, I. D., "Effect of thermochemistrya double modeling coneon hypersonic flow over," *AIAA Scitech 2019 Forum*, American Institute of Aeronautics and Astronautics Inc, AIAA, 2019.

[47] Gaily, T. A. and Carlson, L. A., "Nonequilibrium chemical and radiation coupling, Part II: Results for AOTV flowfields," *Journal of Thermophysics and Heat Transfer*, Vol. 6, American Institute of Aeronautics and Astronautics Inc., may 1992, pp. 392–399.

[48] Hill, C., Gordon, I. E., Kochanov, R. V., Barrett, L., Wilzewski, J. S., and Rothman, L. S., "HITRANonline: An online interface and the flexible representation of spectroscopic data in the HITRAN database," *Journal of Quantitative Spectroscopy and Radiative Transfer*, Vol. 177, jul 2016, pp. 4–14.

[49] Jackson, J. D., *Classical Electrodynamics*, Wiley, 2004.

[50] Stratton, J. A., *Electromagnetic Theory*, John Wiley and Sons, Inc., Hoboken, NJ, USA, oct 2015.

[51] Mishchenko, M. I., "Light scattering by randomly oriented axially symmetric particles," *Journal of the Optical Society of America A*, Vol. 8, No. 6, jun 1991, pp. 871.

[52] Wigner, E. P. and Fano, U., "Group Theory and Its Application to the Quantum Mechanics of Atomic Spectra," *American Journal of Physics*, Vol. 28, No. 4, 1960, pp. 408–409.

[53] Yang, W., "Improved recursive algorithm for light scattering by a multilayered sphere," *Applied Optics*, Vol. 42, No. 9, mar 2003, pp. 1710.

[54] Waterman, P. C., "Matrix theory of elastic wave scattering," *The Journal of the Acoustical Society of America*, Vol. 60, No. 3, 1976, pp. 567–580.

[55] Wielaard, D. J., Mishchenko, M. I., Macke, A., and Carlson, B. E., "Improved T-matrix computations for large, nonabsorbing and weakly absorbing nonspherical particles and comparison with geometrical-optics approximation," Tech. rep., 1997.

[56] Somerville, W. R. C., Auguié, B., and Le Ru, E. C., "Severe loss of precision in calculations of T-matrix integrals," 2012.

[57] Mishchenko, M. I. and Travis, L. D., "T-matrix computations of light scattering by large spheroidal particles," *Optics Communications*, Vol. 109, No. 1-2, jun 1994, pp. 16–21.

[58] Villafane, L., Banko, A., Kim, J. H., Elkins, C., and Eaton, J. K., "Radiative heating of inertial particles in a particle-laden turbulent duct flow," *10th International Symposium on Turbulence and Shear Flow Phenomena*, 2017.

[59] Waterman, P., "Matrix formulation of electromagnetic scattering," *Proceedings of the IEEE*, Vol. 53, No. 8, 1965, pp. 805–812.

[60] Barber, P. and Yeh, C., "Scattering of electromagnetic waves by arbitrarily shaped dielectric bodies," *Applied Optics*, Vol. 14, No. 12, dec 1975, pp. 2864.

[61] Mishchenko, M. I., "Calculation of the amplitude matrix for a nonspherical particle in a fixed orientation," *Applied Optics*, Vol. 39, No. 6, 2000, pp. 1026.

[62] MISHCHENKO, M. I. and TRAVIS, L. D., "Capabilities and Limitations of a Current Method for Randomly Oriented , Rotationally," *J. Quant. Spectrosc. Radiat. Transfer*, Vol. 60, No. 3, 1998, pp. 309–324.

[63] Somerville, W., Auguié, B., and Le Ru, E., "Accurate and convergent T-matrix calculations of light scattering by spheroids," *Journal of Quantitative Spectroscopy and Radiative Transfer*, Vol. 160, jul 2015, pp. 29–35.

[64] "Nanoparticle formation by femtosecond laser ablation - IOPscience," .

[65] Dauvois, Y., Rochais, D., Enguehard, F., and Taine, J., "Statistical radiative modeling of a porous medium with semi transparent and transparent phases: Application to a felt of overlapping fibres," *International Journal of Heat and Mass Transfer*, Vol. 106, 2017, pp. 601–618.

[66] Kostinski, A. B., "On the extinction of radiation by a homogeneous but spatially correlated random medium," *Journal of the Optical Society of America A*, Vol. 18, No. 8, aug 2001, pp. 1929.

[67] Dick, V. P., "Applicability limits of Beer's law for dispersion media with a high concentration of particles," *Applied Optics*, Vol. 37, No. 21, jul 1998, pp. 4998.

[68] Bassenne, M., Esmaily, M., Livescu, D., Moin, P., and Urzay, D. J., “Dynamic spectrally-enriched LES subgrid-scale modeling for preferential concentration of inertial particles in turbulence,” *Center for Turbulence Research Annual Research Briefs*, 2017.

[69] Frankel, A., Iaccarino, G., and Mani, A., “Convergence of the Bouguer-Beer law for radiation extinction in particulate media,” *Journal of Quantitative Spectroscopy and Radiative Transfer*, Vol. 182, 2016, pp. 45–54.

[70] Wei, L.-Y., Li-Yi, Wei, and Li-Yi, “Parallel Poisson disk sampling,” *ACM SIGGRAPH 2008 papers on - SIGGRAPH ’08*, Vol. 27, ACM Press, New York, New York, USA, 2008, p. 1.

[71] Ebeida, M. S., Mitchell, S. A., Patney, A., Davidson, A. A., and Owens, J. D., “A Simple Algorithm for Maximal Poisson-Disk Sampling in High Dimensions,” *Computer Graphics Forum*, Vol. 31, No. 2pt4, may 2012, pp. 785–794.

[72] Mclaughlin, J. B., “Aerosol particle deposition in numerically simulated channel flow,” *Physics of Fluids A: Fluid Dynamics*, Vol. 1, 1989.

[73] Burt, J. M. and Boyd, I. D., “High Altitude Plume Simulations for a Solid Propellant Rocket,” *AIAA Journal*, Vol. 45, No. 12, 2007, pp. 2872–2884.

[74] Siegel, N. P., Ho, C. K., Khalsa, S. S., and Kolb, G. J., “Development and Evaluation of a Prototype Solid Particle Receiver: On-Sun Testing and Model Validation,” *Journal of Solar Energy Engineering*, Vol. 132, No. 2, may 2010, pp. 21008.

[75] Banko, A. J., *Radiation absorption by inertial particles in a turbulent square duct flow*, Ph.D. thesis, Stanford Univeristy, 2018.

[76] Banko, A. J., Villafañe, L., Kim, J. H., and Eaton, J. K., “Temperature statistics in a radiatively heated particle-laden turbulent square duct flow,” *International Journal of Heat and Fluid Flow*, Vol. 84, aug 2020, pp. 108618.

[77] Farbar, E., Boyd, I. D., and Esmaily-Moghadam, M., “Monte Carlo modeling of radiative heat transfer in particle-laden flow,” *Journal of Quantitative Spectroscopy and Radiative Transfer*, Vol. 184, 2016, pp. 146–160.

[78] Mackowski, D. W., “Calculation of total cross sections of multiple-sphere clusters,” *Journal of the Optical Society of America A*, Vol. 11, No. 11, nov 1994, pp. 2851.

[79] Mackowski, D. W. and Mishchenko, M. I., “Calculation of the T matrix and the scattering matrix for ensembles of spheres,” *Journal of the Optical Society of America A*, Vol. 13, No. 11, nov 1996, pp. 2266.

[80] Liu, L., Mishchenko, M. I., and Patrick Arnott, W., “A study of radiative properties of fractal soot aggregates using the superposition T-matrix method,” *Journal of Quantitative Spectroscopy and Radiative Transfer*, Vol. 109, No. 15, oct 2008, pp. 2656–2663.

[81] Mackowski, D. W. and Mishchenko, M. I., "A multiple sphere T-matrix Fortran code for use on parallel computer clusters," *Journal of Quantitative Spectroscopy and Radiative Transfer*, Vol. 112, No. 13, 2011, pp. 2182–2192.

[82] Johnson, P. and Christy, R., "Optical constants of transition metals: Ti, V, Cr, Mn, Fe, Co, Ni, and Pd," *Physical Review B*, Vol. 9, No. 12, jun 1974, pp. 5056–5070.

[83] Gowthami, V., Meenakshi, M., Perumal, P., Sivakumar, R., and Sanjeeviraja, C., "Optical dispersion characterization of NiO thin films prepared by nebulized spray technique," Tech. Rep. 13, 2014.

[84] Mahmoud, S. A., Shereen, A., and Tarawnh, M. A., "Structural and Optical Dispersion Characterisation of Sprayed Nickel Oxide Thin Films," *Journal of Modern Physics*, Vol. 02, No. 10, oct 2011, pp. 1178–1186.

[85] Adsten, M., Joerger, R., Järrendahl, K., and Wäckelgård, E., "Optical Characterization Of Industrially Sputtered Nickel–Nickel Oxide Solar Selective Surface," *Solar Energy*, Vol. 68, No. 4, jan 2000, pp. 325–328.

[86] Simon, I., "Magnetic permeability of nickel in the region of centimetre waves [18]," 1946.

[87] Board, S. S., Council, N. R., and Others, *Vision and voyages for planetary science in the decade 2013-2022*, National Academies Press, 2012.

[88] Lundell, J., "Spallation of the Galileo probe heat shield," *3rd Joint Thermophysics, Fluids, Plasma and Heat Transfer Conference*, 1982, p. 852.

[89] Park, C., Lundell, J. H., Green, M. J., Winovich, W., and Covington, M. A., "Ablation of carbonaceous materials in a hydrogen-helium arcjet flow," *AIAA journal*, Vol. 22, No. 10, 1984, pp. 1491–1498.

[90] Park, C. and Balakrishnan, A., "Ablation of Galileo Probe heat-shield models in a ballistic range," *AIAA journal*, Vol. 23, No. 2, 1985, pp. 301–308.

[91] Milos, F. S., "Galileo probe heat shield ablation experiment," *Journal of Spacecraft and Rockets*, Vol. 34, No. 6, 1997, pp. 705–713.

[92] Milos, F. S., Chen, Y.-K., Squire, T. H., and Brewer, R. A., "Analysis of Galileo probe heatshield ablation and temperature data," *Journal of Spacecraft and Rockets*, Vol. 36, No. 3, 1999, pp. 298–306.

[93] Matsuyama, S., Ohnishi, N., Sasoh, A., and Sawada, K., "Numerical simulation of Galileo probe entry flowfield with radiation and ablation," *Journal of Thermophysics and Heat Transfer*, Vol. 19, No. 1, 2005, pp. 28–35.

[94] Park, C., "Injection-induced turbulence in stagnation-point boundary layers," *AIAA journal*, Vol. 22, No. 2, 1984, pp. 219–225.

[95] Park, C., "Stagnation-region heating environment of the Galileo probe," *Journal of thermophysics and heat transfer*, Vol. 23, No. 3, 2009, pp. 417–424.

[96] Erb, A. J., West, T. K., and Johnston, C. O., "Investigation of Galileo Probe Entry Heating with Coupled Radiation and Ablation," *AIAA Aviation 2019 Forum*, 2019, p. 3360.

[97] Palmer, G., Prabhu, D., and Cruden, B. A., "Aeroheating uncertainties in uranus and saturn entries by the monte carlo method," *Journal of Spacecraft and Rockets*, Vol. 51, No. 3, 2014, pp. 801–814.

[98] Bruno, D., Catalfamo, C., Capitelli, M., Colonna, G., De Pascale, O., Diomede, P., Gorse, C., Laricchiuta, A., Longo, S., Giordano, D., and Others, "Transport properties of high-temperature Jupiter atmosphere components," *Physics of Plasmas*, Vol. 17, No. 11, 2010, pp. 112315.

[99] Stallcop, J. R., Levin, E., and Partridge, H., "Transport properties of hydrogen," *Journal of thermophysics and heat transfer*, Vol. 12, No. 4, 1998, pp. 514–519.

[100] Stallcop, J. R., Partridge, H., and Levin, E., "HH2 collision integrals and transport coefficients," *Chemical physics letters*, Vol. 254, No. 1-2, 1996, pp. 25–31.

[101] Kim, J. G., Kwon, O. J., and Park, C., "Master equation study and nonequilibrium chemical reactions for H+ H2 and He+ H2," *Journal of Thermophysics and Heat Transfer*, Vol. 23, No. 3, 2009, pp. 443–453.

[102] Leibowitz, L. P. and Kuo, T.-J., "Ionizational nonequilibrium heating during outer planetary entries," *AIAA Journal*, Vol. 14, No. 9, 1976, pp. 1324–1329.

[103] Park, C., "Nonequilibrium ionization and radiation in hydrogen-helium mixtures," *Journal of Thermophysics and Heat Transfer*, Vol. 26, No. 2, 2012, pp. 231–243.

[104] Colonna, G., Pietanza, L. D., D'Ammando, G., Celiberto, R., Capitelli, M., and Laricchiuta, A., "Vibrational kinetics of electronically excited states in H 2 discharges," *The European Physical Journal D*, Vol. 71, No. 11, nov 2017, pp. 1–8.

[105] Colonna, G., Pietanza, L. D., and Laricchiuta, A., "Ionization kinetic model for Hydrogen-Helium atmospheres in hypersonic shock tubes," *International Journal of Heat and Mass Transfer*, Vol. 156, 2020, pp. 119916.

[106] Munafò, A., Mansour, N. N., and Panesi, M., "A reduced-order NLTE kinetic model for radiating plasmas of outer envelopes of stellar atmospheres," *The Astrophysical Journal*, Vol. 838, No. 2, 2017, pp. 126.

[107] Liu, Y., James, C. M., Morgan, R. G., and McIntyre, T. J., "Experimental study of saturn entry radiation with higher amount of diluent in an expansion tube," 2018.

[108] Cruden, B. A. and Bogdanoff, D. W., "Shock radiation tests for Saturn and Uranus entry probes," *Journal of Spacecraft and Rockets*, Vol. 54, No. 6, 2017, pp. 1246–1257.

[109] Liu, Y., James, C. M., Morgan, R. G., and McIntyre, T. J., "Using aerothermodynamic similarity to experimentally study nonequilibrium giant planet entry," *Journal of Spacecraft and Rockets*, Vol. 57, No. 5, 2020, pp. 1008–1020.

[110] James, C. M., Gildfind, D. E., Morgan, R. G., Lewis, S. W., and McIntyre, T. J., "Simulating Gas Giant Atmospheric Entry Using Helium and Neon Test Gas Substitutions," *Journal of Spacecraft and Rockets*, Vol. 56, No. 3, 2018, pp. 725–743.

[111] Liu, Y., James, C. M., Morgan, R. G., and McIntyre, T., "Theoretical and experimental study of helium-neon substitution for Saturn entry radiation," *AIAA Aviation 2019 Forum*, 2019, p. 3134.

[112] Alba, C. R., Greendyke, R. B., Lewis, S. W., Morgan, R. G., and McIntyre, T. J., "Numerical modeling of earth reentry flow with surface ablation," *Journal of Spacecraft and Rockets*, Vol. 53, No. 1, 2015, pp. 84–97.

[113] Scalabrin, L. C. and Boyd, I. D., "Numerical Simulations of the FIRE-II Convective and Radiative Heating Rates," AIAA Paper 2007-4044, 2007.

[114] Martin, A., Scalabrin, L. C., and Boyd, I. D., "High Performance Modeling of Atmospheric Re-entry Vehicles," *Journal of Physics: Conference Series*, Vol. 341, No. 1, 2012, pp. 1–12.

[115] Farbar, E., Boyd, I. D., and Martin, A., "Numerical Prediction of Hypersonic Flowfields Including Effects of Electron Translational Nonequilibrium," *Journal of Thermophysics and Heat Transfer*, Vol. 27, No. 4, 2013, pp. 593–606.

[116] Gnoffo, P. A., Gupta, R. N., and Shinn, J. L., "Conservation equations and physical models for hypersonic air flows in thermal and chemical nonequilibrium," 1989.

[117] Park, C., "Assessment of Two-Temperature Kinetic Model for Dissociation and Weakly Ionizing Nitrogen," *Journal of Thermophysics and Heat Transfer*, Vol. 3, No. 3, 1989, pp. 233–244.

[118] McBride, B. J., Zehe, M. J., and Gordon, S., *NASA Glenn Coefficients for Calculating Thermodynamic Properties of Individual Species*, NASA TP-2002-211556, NASA Glenn Research Center, Cleveland, Ohio, 2002.

[119] Palmer, G. and Wright, M., "A Comparison of Methods to Compute High-Temperature Gas Thermal Conductivity," *36th AIAA Thermophysics Conference*, 2003, p. 3913.

[120] Gupta, R. N., Yos, J. M., Thompson, R. A., and Lee, K.-P., "A review of reaction rates and thermodynamic and transport properties for an 11-species air model for chemical and thermal nonequilibrium calculations to 30000 K," 1990.

[121] Wright, M. J., Bose, D., Palmer, G. E., and Levin, E., "Recommended collision integrals for transport property computations part 1: Air species," *AIAA Journal*, Vol. 43, No. 12, 2005, pp. 2558–2564.

[122] Alkandry, H., Boyd, I. D., and Martin, A., "Comparison of Transport Properties Models for Flowfield Simulations of Ablative Heat Shields," *Journal of Thermophysics and Heat Transfer*, Vol. 28, No. 4, 2014, pp. 569–582.

[123] Boyd, I. D. and Schwartzentruber, T. E., *Nonequilibrium Gas Dynamics and Molecular Simulation*, Cambridge University Press, Cambridge, United Kingdom, 2017.

[124] Scalabrin, L. C., "Numerical simulation of weakly ionized hypersonic flow over reentry capsules," *PhD thesis, University of Michigan*, 2007.

[125] Hansson, K., Carroll, A., Poovathingal, S., and Boyd, I., "Analysis of chemical kinetic parameters for hydrogen atmospheres," *AIAA Scitech 2021 Forum*, 2021.

[126] Boyd, I. D., "Monte Carlo Simulation of Nonequilibrium Flow in a Low-Power Hydrogen Arcjet," *Physics of Fluids*, Vol. 9, No. 10, 1997, pp. 3086–3095.

[127] *NIST Chemical Kinetics Database*, NIST, Gaithersburg, MD, 5th ed.

[128] McCay, T. D. and Dexter, C. E., "Chemical Kinetic Performance Losses for a Hydrogen Laser Thermal Thruster," *Journal of Spacecraft and Rockets*, Vol. 24, No. 4, 1987, pp. 372–376.

[129] Talrose, V. and Karachevtsev, G., "Elementary Reactions in Low-Temperature Plasma," 1971.

[130] Higdon, K. J., Cruden, B. A., Brandis, A. M., Liechty, D. S., Goldstein, D. B., and Varghese, P. L., "Direct Simulation Monte Carlo Shock Simulation of Saturn Entry Probe Conditions," *Journal of Thermophysics and Heat Transfer*, Vol. 32, No. 3, 2018, pp. 680–690.

[131] McBride, B. and Gordon, S., *Computer Program for Calculation of Complex Chemical Equilibrium Compositions and Applications I. Analysis*, NASA RP-1311, NASA Glenn Research Center, Cleveland, OH, 1994.

[132] Liu, Y., James, C. M., Morgan, R. G., Jacobs, P. A., Gollan, R., and McIntyre, T. J., "Electron number density measurements in a saturn entry condition," *AIAA Scitech 2021 Forum*, American Institute of Aeronautics and Astronautics Inc, AIAA, 2021, pp. 1–18.

[133] Bensassi, K., M. Brandis, A., and A. Cruden, B., "Computational Modelling for Nonequilibrium Shock Tube Flows," 2020, pp. 2969–2978.

[134] Wiese, W. L. and Fuhr, J. R., "Accurate Atomic Transition Probabilities for Hydrogen, Helium, and Lithium," 2009.

[135] Stone, P. M., Kim, Y. K., and Desclaux, J. P., "Electron-impact cross sections for dipole- and spin-allowed excitations of hydrogen, helium, and lithium," *Journal of Research of the National Institute of Standards and Technology*, Vol. 107, No. 4, 2002, pp. 327–337.

[136] Aggarwal, K. M., Berrington, K. A., Burke, P. G., Kingston, A. E., and Pathak, A., "Electron collision cross sections at low energies for all transitions between the n = 1, 2, 3, 4 and 5 levels of atomic hydrogen," *Journal of Physics D: Applied Physics*, Vol. 24, No. 6, mar 1991, pp. 1385–1410.

[137] Park, C., "Electron impact excitation rate coefficients for hydrogen, helium and alkali atoms," *Journal of Quantitative Spectroscopy and Radiative Transfer*, Vol. 11, No. 1, jan 1971, pp. 7–36.

[138] Fantz, U. and Wünderlich, D., "Franck-Condon factors, transition probabilities, and radiative lifetimes for hydrogen molecules and their isotopomeres," *Atomic Data and Nuclear Data Tables*, Vol. 92, No. 6, nov 2006, pp. 853–973.

[139] Kim, Y. K., "Scaled Born cross sections for excitations of H2 by electron impact," *Journal of Chemical Physics*, Vol. 126, No. 6, feb 2007, pp. 64305.

[140] Franck, J., "Elementary processes of photochemical reactions," *Transactions of the Faraday Society*, Vol. 21, No. FEBRUARY, jan 1926, pp. 536–542.

[141] Condon, E. U., "Nuclear motions associated with electron transitions in diatomic molecules," *Physical Review*, Vol. 32, No. 6, 1928, pp. 858–872.

[142] Yoon, J. S., Song, M. Y., Han, J. M., Hwang, S. H., Chang, W. S., Lee, B., and Itikawa, Y., "Cross sections for electron collisions with hydrogen molecules," *Journal of Physical and Chemical Reference Data*, Vol. 37, No. 2, jun 2008, pp. 913–931.

[143] Jacobsen, F. M., Frandsen, N. P., Knudsen, H., and Mikkelsen, U., "Non-dissociative single ionization of molecular hydrogen by electron and positron impact," *Journal of Physics B: Atomic, Molecular and Optical Physics*, Vol. 28, No. 21, nov 1995, pp. 4675–4689.

[144] Wedding, A. B. and Phelps, A. V., "Quenching and excitation transfer for the c 3Π u- and a 3Σg+ states of H2 in collisions with H2," *The Journal of Chemical Physics*, Vol. 89, No. 5, sep 1988, pp. 2965–2974.

[145] Blair, D. W., Tillack, M. S., and Zaghloul, M., "¡title¿Prediction of particulate characteristics in an expanding laser plume¡/title¿," *Micromachining and Microfabrication Process Technology VII*, edited by J. M. Karam and J. A. Yasaitis, Vol. 4557, SPIE, sep 2001, pp. 139–150.

[146] Aita, H., Ogi, Y., and Tsukiyama, K., "Fluorescence lifetimes of the O1Σg+, P1Σg+, R 1Πg, and S1Δg states of H2," *Journal of Molecular Spectroscopy*, Vol. 232, No. 2, aug 2005, pp. 315–322.

[147] Fantz, U., Briefi, S., Rauner, D., and Wünderlich, D., "Quantification of the VUV radiation in low pressure hydrogen and nitrogen plasmas," *Plasma Sources Science and Technology*, Vol. 25, No. 4, jun 2016, pp. 045006.

[148] Stephens, T. L. and Dalgarno, A., “Spontaneous radiative dissociation in molecular hydrogen,” *Journal of Quantitative Spectroscopy and Radiative Transfer*, Vol. 12, No. 4, apr 1972, pp. 569–586.

[149] Pardo, A., “Radiative lifetimes for the B1 σu+ state of the H2 molecule,” *Spectrochimica Acta - Part A: Molecular and Biomolecular Spectroscopy*, Vol. 54, No. 10, sep 1998, pp. 1433–1441.